



Cite this: *Nanoscale*, 2026, **18**, 9469

## Understanding surface wettability: insights from experiments, molecular simulations, and first-principles theory

Emdadul Haque Chowdhury,<sup>a</sup> Md Shahed Hossain Sohan,<sup>a</sup>  
 C. Ulises Gonzalez-Valle,<sup>b</sup> Adri C. T. van Duin<sup>a</sup> and  
 Bladimir Ramos-Alvarado<sup>a\*</sup>

Wettability plays a central role in surface science with far-reaching implications for engineering technologies, biomedical applications, and natural systems. Despite decades of investigation, wettability research remains fragmented across experimental characterization, molecular dynamics simulations, and quantum mechanical calculations, with no unified framework linking observations across length and time scales. This fragmentation originates from inconsistencies in experimental protocols, force field parameterization strategies, and electronic structure descriptions, which have contributed to long-standing debates regarding the intrinsic wetting behavior of many technologically relevant surfaces. This review critically synthesizes advances in experimental measurements, atomistic simulations, and first principles modeling to identify areas of agreement, unresolved controversies, and persistent knowledge gaps in wettability research. Emphasis is placed on the breakdown of classical wetting models at nanometric scales, the non-uniqueness of the contact angle as a sole wettability descriptor, and the role of complementary thermodynamic, structural, and dynamic quantities in characterizing solid–liquid affinity. The review examines how interfacial modeling choices, including surface preparation, interaction potentials, mixing rules, and electronic structure approximations, systematically influence predicted wettability and contribute to inconsistent conclusions across studies. By integrating interfacial chemistry, molecular-scale structure, and macroscopic observables, this work provides a conceptual roadmap for designing wettability studies that are more consistent, reproducible, and predictive across methodologies and length scales.

Received 26th December 2025,  
 Accepted 24th March 2026

DOI: 10.1039/d5nr05460e

[rsc.li/nanoscale](http://rsc.li/nanoscale)

<sup>a</sup>Department of Mechanical Engineering, The Pennsylvania State University, University Park, PA 16802, USA. E-mail: [bzr52@psu.edu](mailto:bzr52@psu.edu)

<sup>b</sup>Richard J. Resch School of Engineering, University of Wisconsin-Green Bay, Green Bay, Wisconsin 54311, USA



**Emdadul Haque Chowdhury**

*Emdadul Haque Chowdhury is currently pursuing his PhD in Mechanical Engineering at The Pennsylvania State University. He holds a Bachelor of Science (BSc) in Mechanical Engineering from the Bangladesh University of Engineering and Technology. His research focuses on the fundamental study of nanoscale thermal, physical, and mechanical properties through atomistic level modeling, as well as the study of solid–liquid interfacial phenomena.*



**Md Shahed Hossain Sohan**

*Md Shahed Hossain Sohan is currently a Ph.D. student in Mechanical Engineering at The Pennsylvania State University. He earned his B.Sc. in Mechanical Engineering from Bangladesh University of Engineering and Technology (BUET). His research focuses on the atomistic simulation and computational modeling of materials to investigate physical and chemical properties at nanoscale.*



# 1. Introduction

## 1.1 Importance of wettability in nature, surface science, and engineering

Wettability refers to a liquid's ability to spread over a solid surface, which is influenced by the balance of adhesive forces between the solid and liquid, as well as cohesive forces within the liquid itself.<sup>1</sup> Wetting properties serve as a critical indicator of solid–liquid affinity by bridging molecular-level interactions with macroscopic observables, such as the contact angle.<sup>2,3</sup> The study of wettability has emerged as a topic of significant and growing importance among researchers and engineers owing to its central role in surface engineering. Fig. 1 illustrates how the number of published research articles related to wettability has increased significantly in recent years due to its increasing importance in academia and industry.

Wettability connects fundamental surface science with applications across engineering, materials science, biology, and medicine. Researchers can precisely tune critical interfacial properties, including liquid adhesion, droplet spreading, and fluid transport on surfaces, by controlling surface wettability through tailored surface chemistry and micro/nanoscale topography. On superhydrophilic surfaces, water spreads fully into uniform thin films, while superhydrophobic surfaces facilitate water to bead up and roll off with minimal resistance. These extreme wetting conditions support a broad spectrum of technologies, including self-cleaning coatings, anti-fogging treatments, anti-icing surfaces, and advanced separation

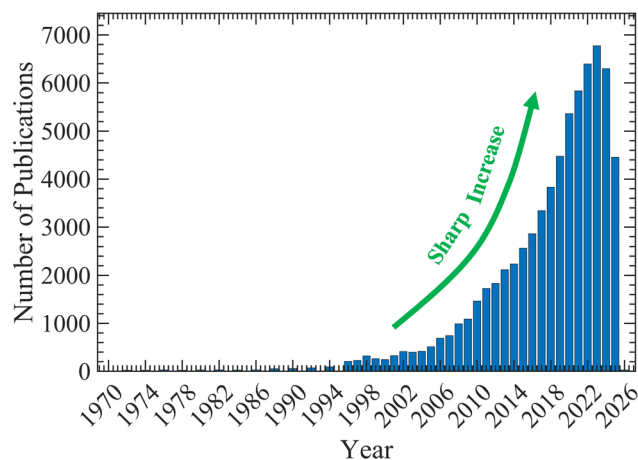


Fig. 1 Number of papers indexed in the Web of Science within the years 1970–2026 by the topic of “wettability”.

membranes.<sup>4–7</sup> Therefore, comprehending the fundamentals of wettability from atomic- to macro-scale has become crucially important in contemporary surface engineering.

The lotus leaf exemplifies naturally existent superhydrophobic surfaces.<sup>4,5,7</sup> It possesses a hierarchical structure consisting of microscale papillae enveloped in nanoscale hydrophobic wax tubes that entrap air pockets beneath water droplets, known as the Cassie–Baxter state.<sup>5</sup> This reduces solid–liquid interaction, rendering the surface extremely non-wetting. As a



C. Ulises Gonzalez-Valle

Dr. C. Ulises Gonzalez-Valle is an Assistant Professor of Mechanical Engineering at the University of Wisconsin-Green Bay. His research focuses on thermal sciences, heat transfer, and advanced cooling technologies for high-performance electronic systems. Dr González-Valle leads research efforts in thermal management, including liquid-cooled heat sinks and advanced cooling architectures for next-generation processors. In

addition to his research activities, he serves as a Subject Editor for the journal *Applied Thermal Engineering*. He obtained a Bachelor's and a Master's degree in Mechanical Engineering from the University of Guanajuato in 2014 and 2017, respectively. He continued his education at Pennsylvania State University, where he obtained a Master's degree and a Ph.D. in Mechanical Engineering in 2020 and 2021, respectively. After completing his doctoral studies, Dr González-Valle joined the University of Wisconsin-Green Bay as an Assistant Professor, where he continues to develop research and educational initiatives in thermal sciences and energy systems.



Adri C. T. van Duin

Dr. Adri C. T. van Duin is a Distinguished Professor of Mechanical Engineering, with courtesy appointments in the departments of Chemical Engineering, Chemistry, Material Science & Engineering and Engineering Science & Mechanics at Penn State University. He is the inventor and main developer of the ReaxFF and eReaxFF reactive force field method, which is currently one of the leading

methods for atomistic-scale simulations of chemical reactions in molecules, materials and their interfaces. He has published over 600 journal papers describing ReaxFF and eReaxFF development and applications, which include material growth, energy storage, combustion, catalysis and material and molecular response to extreme environments. Dr van Duin earned his PhD in Chemistry from the Delft University of Technology in the Netherlands.



result, water droplets slide off easily, carrying away dirt particles and creating the self-cleaning phenomena known as the “lotus effect”. Like the lotus leaf, the rice leaf also exhibits superhydrophobicity but displays anisotropic behavior. The hierarchically structured papillae are arranged parallel to the leaf edge, guiding droplets moving along its length while hindering perpendicular motion.<sup>8</sup> This facilitates directional water transport that helps channel rain or dew towards the stem, promoting self-cleaning and water management around the plant. This has inspired biomimetic surfaces for controlled droplet manipulation and microfluidic applications.<sup>8</sup> Similar phenomena can be observed in insects; the water strider’s legs have long, densely packed hair covered with nanogrooves and a hydrophobic wax coating.<sup>9</sup> This architecture traps air between the hairs, making the legs superhydrophobic, and enables each leg to carry up to 15 times the insect’s body weight without breaking the surface tension. The Namib desert beetle is another remarkable example of special wettability. It has alternating hydrophilic bumps and hydrophobic waxy troughs on its back. The hydrophilic bumps nucleate water droplets from fog. Once droplets grow large enough, they roll down hydrophobic channels towards the beetle’s mouth. Spider silk also displays a unique water-collecting ability through its periodic spindle-knot and joint structure.<sup>10</sup> Upon wetting, this architecture generates both a surface energy gradient and a Laplace pressure difference, making droplets migrate toward the knots where they coalesce into larger drops. These fog harvesting strategies inspire the creation of synthetic surfaces and fibers that may easily collect and trans-

port water in arid environments. These examples of nature employing combinations of surface chemistry and hierarchical micro/nanostructures to modulate wettability have inspired biomimetic surface designs.

The lotus effect has inspired the development of self-cleaning coatings characterized by two key features: hierarchical micro/nanoscale roughness and low surface energy materials.<sup>11</sup> Such coatings have applications in exterior paints, architectural coatings, roof tiles, building facades, automotive windshields, solar panels, and self-cleaning textiles.<sup>4,7</sup> Superhydrophobicity has also found significant application in anti-fouling surfaces.<sup>12</sup> Biofouling refers to the unwanted accumulation of microorganisms (such as bacteria and algae) and macrofoulers (such as mussels, barnacles, and seaweed) on submerged surfaces. This increases hydrodynamic drag and fuel consumption and costs the shipping industry billions of dollars annually in maintenance and operational inefficiencies. Superhydrophobic surfaces have low surface energy that reduces the adhesion strength of fouling organisms. Additionally, they trap air within the hierarchical texture that creates a physical barrier that minimizes direct contact between the surface and biological matter. These anti-fouling coatings have applications in ship hulls, marine sensors and underwater equipment, offshore platforms and pipelines, as well as medical implants and food processing equipment.<sup>12</sup>

Another application of interest is spaceships; space missions on the lunar and Martian surfaces have significant challenges due to the deposition of charged dust particles on spacecraft surfaces, primarily through van der Waals (vdW) interactions. The accumulation of dust can impede the performance of spacecraft by obstructing sunlight, hence diminishing the power output in solar panels. Accumulation of dust on sensors can impair image quality and lead to sensor breakdown. Additionally, they may result in the overheating of electrical devices. Superhydrophobic surface coating minimizes this issue due to having low surface energy and reduced particle-surface contact area, which weakens the vdW interaction and makes it difficult for dust to adhere to the surface.<sup>13</sup> Moreover, superhydrophobic anti-icing surfaces are crucial for aircraft wings, power transmission lines, and wind turbine blades. The texture in those surfaces delays ice nucleation by reducing water-surface contact area. Also, the hierarchical micro/nanostructures trap air pockets that act as a thermal insulator. Consequently, water droplets roll off quickly before freezing, and the reduced ice adhesion strength makes snow removal easier.<sup>14</sup> In thermal power plant condensers, desalination systems, and HVAC applications, a superhydrophobic surface promotes drop-wise instead of film-wise condensation.<sup>15,16</sup> In film-wise condensation, the liquid film on the condenser surface acts as a barrier in thermal energy transport. But in drop-wise condensation, the condensate droplets roll off quickly, exposing the cold surface and facilitating further condensation. Moreover, drop-wise condensation provides 5–10 times higher heat transfer coefficient than film-wise condensation.<sup>15,16</sup> Other superhydrophobic engineering applications include stain-resistant coatings for water bottles and fabrics,<sup>17,18</sup> anti-corrosion surface,<sup>19,20</sup> and drag-reduction.<sup>6</sup>



**Bladimir Ramos-Alvarado**

*Dr. Bladimir Ramos-Alvarado is the Kenneth Kuan-Yun Kuo Early Career Professor and an Associate Professor of Mechanical Engineering, with a courtesy appointment in Chemical Engineering, at Penn State University. He is the Principal Investigator of the Interfacial Phenomena Lab (IPHEL) and a member of the Materials Computation Center, as well as an Associate of the Institute for Computational and*

*Data Sciences (ICDS) at Penn State. In addition, Dr Ramos serves as a Journal Content Editor for Applied Thermal Engineering (Elsevier). Dr Ramos earned a PhD in Mechanical Engineering from the Georgia Institute of Technology in 2016. Dr Ramos’s research focuses on modeling transport processes across multiple length scales, with a strong emphasis on multiphysics and atomistic-scale modeling. His primary research interests center on thermal and momentum transport across solid–liquid interfaces and the role of surface chemistry and interfacial liquid properties in governing these phenomena.*



Superhydrophilic surfaces are important for anti-fogging coatings used in eyeglasses, automotive windshields, mirrors, camera lenses, and solar panels.<sup>7</sup> The discrete microdroplets in fog scatter light and make the surface hazy and opaque. Superhydrophilic coatings force condensed water to form a homogenous, transparent thin film where light can pass through with minimal refraction and no scattering, aiding optical clarity. Such coatings have applications in solar panels as well. These coatings serve a dual purpose: the anti-fogging behavior maintains light transmission, and the water spreading washes away dust and dirt, maintaining energy conversion efficiency.<sup>21</sup> Moreover, the TiO<sub>2</sub> coatings used in building facades, glass tiles, and solar panels display photo-induced superhydrophilicity. Upon UV irradiation, the TiO<sub>2</sub> coatings generate oxygen vacancies and hydroxyl groups that induce superhydrophilicity. This causes water to spread into a thin film. Also, the hydroxyl radicals oxidatively decompose organic contaminants into CO<sub>2</sub> and H<sub>2</sub>O through photocatalysis, inducing effective self-cleaning.<sup>22</sup> Fig. 2(a) and (b) depict some examples of super-hydrophobic and super-hydrophilic surfaces found in nature and their engineering applications, respectively.

Structures with special wettability can provide an efficient solution for environmental remediation. Superhydrophobic-superoleophilic surfaces are used to separate oil from water in oil spill recovery. These surfaces repel water while attracting oil, and are used in absorbent sponges, meshes, and fabrics to selectively absorb and recover oil.<sup>23</sup> Conversely, superhydrophilic but underwater superoleophobic surfaces are used to separate water from oil. They trap water and repel oil when submerged, allowing water to pass through while rejecting oil, and are effective for separating oil-in-water emulsions.<sup>23</sup>

Another application can be found in nanofabrication, given that template surfaces with patterned hydrophilic and hydrophobic zones aid site-selective crystallization. When the solution containing dissolved materials is applied to the surface, it seeks out and confines itself to the hydrophilic zones. Thus, when the solvent evaporates, crystals nucleate and grow in pre-determined hydrophilic zones.<sup>7,24</sup> In addition, controlled wettability in nanochannels gives us precise control over fluid behavior.<sup>24–26</sup> In nanochannels, a significant portion of fluid molecules directly interacts with channel walls. As such, surface wettability becomes the key factor in controlling fluid transport and chemical reactivity.<sup>24,25</sup> Hydrophobic channels can exhibit slip boundary conditions that reduce flow resistance, while hydrophilic channels promote spontaneous capillary filling and can induce ordered molecular layers near the surface. Such controlled fluid behavior is critical for nanofluidic applications, including nanofiltration membranes and nanopore-based molecular sensing. Furthermore, confining chemical reactions in nanochannels can significantly affect reaction kinetics.<sup>27–29</sup> Nanoconfinement increases the reactant's local concentration and enhances effective collision and reaction rates. Furthermore, the geometric constraints of nanochannels can impose preferential molecular orientation that favors desired reaction pathways and reduce activation energy barrier. These confinement effects have been utilized in selective chemical synthesis processes, zeolite catalysis, and fuel cell electrodes.<sup>29,30</sup> In lithium-ion batteries, proper wetting of electrode nanopores by liquid electrolyte is crucial for optimal electrochemical performance, given that the nanoporous structures contain the active material. A complete electrolyte penetration ensures that lithium ions can access all available active sites during charge-discharge cycles.<sup>24,31</sup> Therefore, to opti-



Fig. 2 Application of (a) super-hydrophobic and (b) super-hydrophilic surfaces in nature and in engineering.



mize battery performance, it is crucial to improve electrode wettability using surface modification techniques and employing electrolytes with superior wetting characteristics.

Special wetting surfaces have importance in biomedical and textiles application.<sup>32,33</sup> When contaminated water from coughs, splashes, or contact lands on a fabric, it carries bacteria with it. When water soaks in, it leaves the bacteria behind in contact with the surface. But in a superhydrophobic textile, contaminated droplets roll off, taking bacteria with them.<sup>34</sup> In addition, bacteria need moisture to survive and colonize, thus water-repellent surfaces create an unfavorable environment for bacteria, reducing infection transmission.<sup>34</sup> Similarly, the superhydrophobic outer layer of wound dressing prevents external contamination and bacterial penetration.<sup>35</sup>

## 1.2 Motivation and scope of this review article

Although wettability has widespread application in material design, biology, and engineering, as discussed in section 1.1, significant scientific and real-world challenges remain unresolved, which motivates more in-depth research. Classical wetting theories work at the macroscale but break down at the nanoscale. Young's equation (1805)<sup>36</sup> assumes an ideal, smooth, chemically homogeneous surface, while real surfaces experience nanoscale roughness, chemical patches, defects, and contamination. Although Wenzel<sup>37</sup> and Cassie–Baxter<sup>38</sup> models extended Young to incorporate roughness and surface texture, both models treat roughness as a single number applied uniformly across the entire surface, leading to results that differ significantly from expectations.<sup>7</sup> A deeper problem is that most of the wettability research is centered on the contact angle measurement, which is basically trying to capture complex interfacial physics with a single macroscopic metric. At the nanoscale, interfacial water structuring, hydrogen bond networks, and entropic contributions become important, but these molecular-level features are invisible to macroscopic descriptions.<sup>4</sup> This motivates the need for molecular and electronic-scale understanding of wetting properties alongside continuum models.

Wettability has been widely studied through experiments, molecular dynamics (MD) simulations, and density functional theory (DFT), but there is a clear connection gap between these approaches. Each of them has distinct strengths and limitations. From the experimental side, contact angle measurements vary widely even for almost identical surfaces due to protocol dependence, environmental contamination, and differences in measurement techniques. For instance, the intrinsic wettability of graphite and gold has been debated for decades.<sup>39–41</sup> While MD simulations offer molecular-level insight, they are extremely sensitive to force field selection and the initial interfacial molecular structure. The same material can be found hydrophobic or hydrophilic, depending on the water model employed and cross-interaction parameters utilized. On the other hand, DFT provides an accurate and in-depth understanding of electronic structure, polarization, and chemical bonding, but remains limited to small system sizes and short timescales. Also, the results depend on the choice of exchange correlation functional and dispersion corrections.

Hence, there is a clear disconnection between these approaches: experiments measure highly-protocol-dependent macroscopic observables but cannot resolve molecular details; MD predicts interfacial chemistry but relies on the molecular interactions parameterization; and quantum mechanics calculations achieve electronic accuracy but cannot approach experimental length and time scales. Bridging this gap by employing an integrated framework that enables cross-validation is crucial for an accurate understanding of wettability.

In the last two decades, wettability research has grown exponentially, with thousands of papers being published each year in materials science, chemistry, physics, engineering, and biology (see Fig. 1). However, some disconnect is observed across fields and amongst experiments, simulations, and theories, each describing the same phenomena using varied terminology and failing to reach a consensus. On top of that, existing reviews often concentrate on a certain methodology, whether it is exclusively experimental, computational, or application-driven, or they may focus on specific material categories, such as carbon surfaces or polymers. We still lack a cross-platform analysis of wettability connecting theory, experimental characterization, MD simulations, and first-principles calculations while discussing their strengths and limitations side by side. This review seeks to address this gap by combining insights from these methodologies, identifying areas of consensus, controversy, and significant knowledge gaps, and thereby establishing a unified foundation for future research. Fig. 3 depicts the knowledge map of our wettability review, highlighting the main aspects of wettability research discussed in this paper.



**Fig. 3** Knowledge map of this wettability review article, highlighting the main aspects of wettability research: application, theoretical analyses, computational modeling, experimental studies, and the current knowledge gap in wettability research.



The subsequent sections of this article are structured as follows: the theoretical foundation of wettability is the subject of section 2, which encompasses classical models and molecular-level descriptors. Experimental methodologies and results are the primary focus of section 3, which also addresses methodological constraints. Section 4 addresses MD simulations and recent advancements in parameter optimization and entropy analysis. Section 5 explores DFT and *ab initio* calculations, elucidating the electronic structural contributions and constraints of classical potentials. Section 6 investigates the current knowledge gaps in wettability research. Lastly, section 7 presents findings and prospective research directions.

## 2. Theoretical background on wettability

### 2.1 Classical concepts: contact angle, surface tension, and Young's equation

Thomas Young established the foundational description of wettability on ideal surfaces in 1805.<sup>42</sup> The mathematical expression of Young's theory, formulated by later researchers, describes the mechanical equilibrium at the three-phase contact line, where solid, liquid, and vapor phases meet. Here, three interfacial tensions, which are solid–vapor tension ( $\gamma_{SV}$ ), the solid–liquid tension ( $\gamma_{SL}$ ), and the liquid–vapor tension ( $\gamma_{LV}$ ), act as forces per unit length along the contact line. A balance of the horizontal components of these forces yields:

$$\gamma_{SV} - \gamma_{SL} = \gamma_{LV} \cos(\theta) \quad (1)$$

where  $\theta$  is the contact angle measured through the liquid phase. A large contact angle ( $>90^\circ$ ) indicates hydrophobicity, whereas a small contact angle ( $<90^\circ$ ) implies hydrophilicity. Fig. 4 illustrates the three vector components of Young's equation.

Young's equation obeys some key assumptions.<sup>43,44</sup> It is valid for a perfectly smooth surface with no roughness at any scale, chemically homogeneous, rigid and non-deformable, inert (no chemical reaction between solid–liquid), non-porous,

and insoluble. Young's equation further assumes the system has reached true thermodynamic equilibrium, it has no contact angle hysteresis and maintains constant interfacial tension during measurements. However, real surfaces violate these assumptions in various ways. All practical surfaces possess roughness at some length scale, chemical heterogeneity arising from contamination, oxidation, grain boundaries, or intentional patterning. Deviations from the ideal surface condition lead to measuring the apparent contact angle (APCA), defined as the angle formed between the tangents to the liquid–air interface and the solid surface. The APCA is widely used as a practical indicator of wettability and has a dependence on the roughness, chemical heterogeneity, and composition of the surface.<sup>45</sup> Moreover, soft materials such as polymers and biological tissues deform under capillary forces involving a moving three-phase contact line (TCL). Further, clean surfaces can be contaminated by airborne hydrocarbon adsorption within seconds, thereby altering their wetting characteristics. As such, real surfaces exhibit contact angle hysteresis (CAH); that is, the advancing contact angle (ACA, measured as liquid spreads forward) differs from the receding angle (RCA, measured as liquid withdraws).<sup>46</sup> Because measuring CAH inherently requires a moving TCL, they serve as the foundational metrics for defining the dynamic contact angle on non-ideal surfaces.

The limitations initially motivated the development of extended equilibrium models (Wenzel, Cassie–Baxter (CB), and intermediate Cassie–Wenzel – presented in Fig. 5) as well as the dynamic models to address rough and heterogeneous surface wettability.<sup>47</sup> The following section provides an overview of surface area-dependent static models, followed by a brief discussion of the classical models of dynamic wetting to discuss the effect of a moving contact line.

### 2.2 Surface roughness models: Wenzel and Cassie–Baxter

**2.2.1 Wenzel model.** Robert Wenzel recognized that surface roughness increases the actual solid–liquid contact area compared to the droplet's horizontal projection, and this



Fig. 4 Three vector components of Young's equation: solid–liquid ( $\gamma_{SL}$ ), solid–vapor ( $\gamma_{SV}$ ), and liquid–vapor ( $\gamma_{LV}$ ) surface tensions.  $\theta$  is the contact angle.





**Fig. 5** Schematic depiction of the surface roughness effect on the solid surface wetting by a droplet on (a) an ideal smooth surface, (b) Wenzel state, (c) intermediate state between Wenzel and Cassie–Baxter, (d) Cassie–Baxter state. Reproduced with permission from ref. 47; Copyright 2019 John Wiley & Sons.

should modify the observed contact angle.<sup>37</sup> His model has some key assumptions.<sup>48,49</sup> First, it considers a homogeneous wetting regime, that is, the liquid fully penetrates the surface texture and maintains close contact with all topographical features with no air pockets beneath. Second, the intrinsic contact angle is uniform everywhere. Third, the droplet size is much larger than the characteristic length scale of the roughness. Fourth, the system is at thermodynamic equilibrium, and the contact line adopts its lowest-energy configuration. With these assumptions, Wenzel introduced a dimensionless roughness factor,  $r$  ( $\geq 1$ ) defined as the true solid surface area divided by the projected (flat) area, when  $r = 1$  represents a perfectly smooth surface. Considering the APCA on the rough surface as  $\theta^*$ , and the intrinsic Young angle on the ideally smooth surface as  $\theta$ , the Wenzel equation can be expressed as:

$$\cos \theta^* = r \cos \theta \quad (2)$$

This relationship implies that surface roughness amplifies the intrinsic wetting tendency of the material; that is, a hydrophilic surface becomes more hydrophilic, and a hydrophobic surface becomes more hydrophobic. In addition, this effect explains that roughening a surface can make its wetting behavior more extreme, or in other words, enhanced hydrophilicity or hydrophobicity based on the underlying surface chemistry. Wenzel's model has important limitations.<sup>44,50</sup>

Assuming a complete liquid penetration into the texture may not be true for surfaces with deep and high aspect ratio structures, or intrinsically hydrophobic chemistry, where air can be trapped. The model also assumes a single equilibrium angle. However, real rough surfaces show significant  $\theta$  hysteresis because of contact line pinning at geometric edges and defects.<sup>51</sup> Furthermore, the global roughness factor represents a spatial average, ignoring local texture variations. These limitations motivated the development of the Cassie–Baxter model for scenarios where air entrapment occurs.

**2.2.2 Cassie–Baxter model.** A. B. D. Cassie and S. Baxter extended this analysis to porous and textured surfaces where

the liquid does not fully penetrate the roughness, but rather sits on the texture, with air pockets trapped beneath.<sup>38</sup> This model characterizes the solid as a composite surface with two distinct regions: solid patches where the liquid contacts the substrate, and air pockets where liquid bridges without touching the gap's base.<sup>52</sup> This model introduces the following assumptions:<sup>44,50,52</sup> first, the surface will maintain its composite characteristics by stably trapping air within the texture throughout the measurement; second, the surface texture is chemically homogeneous so that all solid regions will present the same intrinsic contact angle; third, the droplet size is large compared to the texture features; and fourth, the liquid over air pockets is considered to be in a perfectly non-wetting condition with a  $180^\circ$  contact angle.

Assuming that  $f_{\text{SL}}$  is the area fraction of the surface where solid–liquid contact occurs,  $f_{\text{LV}}(1 - f_{\text{SL}})$  is the fraction where the liquid bridges over air, and considering that the effective contact angle over the air fraction is  $180^\circ$  ( $\cos 180^\circ = -1$ ), the Cassie–Baxter equation gives the APCA  $\theta^*$  as:

$$\cos \theta^* = f_{\text{SL}} \cos \theta - (1 - f_{\text{SL}}) \quad (3)$$

Here,  $\theta$  is the intrinsic Young's contact angle on a flat, smooth surface of the same solid material. Eqn (3) can be rewritten as:

$$\cos \theta^* = f_{\text{SL}}(\cos \theta + 1) - 1 \quad (4)$$

Eqn (4) shows that reducing the solid–liquid contact fraction,  $f_{\text{SL}}$ , always increases  $\theta^*$ , regardless of the intrinsic contact angle  $\theta$ . That is, if the texture reduces  $f_{\text{SL}}$  sufficiently, a mildly hydrophobic material ( $\theta$  slightly above  $90^\circ$ ) can achieve superhydrophobicity with APCAs exceeding  $150^\circ$ . This principle motivates designing biomimetic superhydrophobic surfaces (lotus leaf effect), where hierarchical micro- and nanoscale structures maximize air entrapment and minimize solid–liquid contact.



While the Wenzel and CB equations (eqn (2) and (4)) provide foundational frameworks for predicting wettability, they rely on global surface area averages and assume a static, ideal equilibrium contact line. However, as mentioned in section 2.1, the measured  $\theta$  is dependent on the contact line motion direction,<sup>53</sup> and the contact line become stuck at local energy barriers due to roughness, chemical heterogeneities, and flaws, which leads to the CAH.<sup>54</sup> Because the classical Wenzel and CB models fundamentally fail to capture these microscopic events, theoretical predictions from eqn (2) and (4) often deviate from experimental observations.<sup>55,56</sup> The following section discusses the attempts to incorporate microscopic physics into the static models with modifications to the Wenzel and CB equations.

**2.2.3 Modifications to classical models.** To bridge the gap between macroscopic global averages and localized contact line behavior, several studies have been conducted to incorporate additional parameters to address the discrepancies observed by using the Wenzel and CB equations. For example, Choi *et al.*<sup>57</sup> provided a more accurate estimation of roll-off angles and directional wettability on patterned substrates. They introduced a differential surface texture parameter to predict ACA, RCA, and CAH, which is dependent on surface texture anisotropy. However, their approach is somewhat geometry-specific and limited to irregular and well-defined surfaces, hindering the applicability to regular surfaces, though the authors introduced a reasonable idea regarding the interactions on regular surface wettability. Forsberg *et al.*<sup>56</sup> addressed the issues in Wenzel's equation, explaining the elevated values observed for ACA on microstructure pillars. The author proposed a contact line pinning mechanism to replace the global roughness factors with a line fraction approach, which only considers the portion of the pinned contact line on surface roughness. The authors produced a valid qualitative approach; however, this method was strongly dependent on pillar geometry and arrangement, limiting the generalization of their approach.

The attempts to correct the Wenzel and CB equations were limited to two-dimensional efforts until Yamaguchi *et al.*<sup>58</sup> extended the study to incorporate three-dimensional effects into the Wenzel equation, redefining the pitch and depth of nano-periodic structures. Yamaguchi *et al.*<sup>58</sup> claimed that their 3-D model agreed with experimental results on nano-fabricated silicon structures and identified a method to find threshold pitch and depth values for the transition between hydrophilic and hydrophobic surfaces. Nonetheless, their work only focused on Wenzel-type surface roughness, Liu *et al.*<sup>59</sup> proposed a solution to update the CB equation and render the model applicable to dynamic 3-D droplets. They reasoned that in a 3-D system, frictional resistance only acts on the portion of the contact line that is physically in contact with the solid structures. A new geometric parameter called the line solid fraction ( $\lambda_s$ ) was introduced, defined as the length ratio of the real (microscopic) contact line on the solid to the apparent (macroscopic) contact line, shown in eqn (5).

$$\cos \theta_R = \cos \theta' + (\cos \theta_R - \cos \theta_Y) \lambda_s \quad (5)$$

where  $\theta_R$  is the apparent receding angle,  $\theta'$  is the static CB angle, and  $(\cos \theta_R - \cos \theta_Y)$  represents the hysteresis. Liu *et al.*<sup>59</sup> claimed that  $\lambda_s$  scales the hysteresis term in the CB equation successfully to predict a wide range of 3-D microstructures.

While the introduction of line fractions and 3-D corrections extend classical wetting models down to the microscale, these modified equations presume that the liquid acts as a continuous medium and that the contact line remains a macroscopic boundary. As the dimensions of the system approach the molecular level, the modified equations begin to lose their physical validity as discussed in the next sections.

### 2.3 Limitations of macroscopic descriptions at the nanoscale

Young's equation and the classical wetting models work well at macroscopic scales, but their underlying assumptions do not hold at smaller length scales. They assume that solid-liquid and liquid-vapor interfaces have sharp boundaries with well-defined surface tensions. They further assume that bulk liquid properties hold right up to the interface. However, close to the liquid-vapor interface, the liquid's density changes gradually over a few molecular diameters.<sup>24,60,61</sup> Similarly, ordered liquid molecular layers and orientation preferences are observed near the solid interface.<sup>24,60,61</sup> In the case of nanoscale confinement, such as water in a nanochannel or a nanoscale droplet, the thickness of these interfacial regions scale to the system's size itself, and these interfacial regions can overlap.<sup>24,61</sup> At this point, the concept of a single contact angle becomes ambiguous. Atomistic simulations demonstrated that near a solid-liquid interface, water molecules organize themselves with a specific arrangement of hydrogen bonds.<sup>41,60-63</sup> These atomistic features cannot be captured with a single contact angle measurement and the necessity of calculating the APCA at the interface becomes clear.

Finite-size effects add another layer of complexity in contact angle calculation. Nanoscale droplets have highly curved surfaces, whereas the surface tension used in Young's equation is for a flat interface. Molecules at a curved interface have a different local environment than those at a flat interface, and this can change the effective surface tension.<sup>64</sup> These changes in surface tension with curvature can be quantified through the Tolman length correction.<sup>64,65</sup> The correction becomes significant for nanoscale droplets with a radius of only a few nanometers, and the effective surface tension differs from the bulk value. Another finite-size effect arises from line tension.<sup>66,67</sup> Line tension describes the excess energy per unit length at the one-dimensional boundary where the solid, liquid, and vapor phases meet.<sup>68</sup> The effect of droplet size on the APCA can be obtained from the modified Young's equation:<sup>66,68,69</sup>

$$\cos \theta = \cos \theta_\infty - \frac{\tau}{\gamma_{LV} r} \quad (6)$$

Here,  $\theta$  is the APCA of the droplet,  $\theta_\infty$  is the intrinsic Young contact angle for an infinitely large droplet,  $\tau$  is the line tension,  $\gamma_{LV}$  is the liquid-vapor surface tension, and  $r$  is the



radius of the contact line. It is apparent from eqn (6) that the line tension effect becomes significant when the contact-line radius  $r$  is small, and for nanoscale droplets, this correction can shift the observed contact angle substantially. As a result, even for nominally identical materials, the contact angles of nanoscale droplets predicted by MD simulations often differ from experimental measurements. Eqn (6) demonstrates the impact of the three-phase contact line (TCL) at the nanoscale; the extent of its influence on real-world macroscopic surfaces has been a subject of considerable debate in the literature. As discussed in section 2.4, this realization challenges classical area-based models.

#### 2.4 The role of the three-phase contact line

Real surfaces often contain micro-structural defects, and experimental disturbances such as viscous forces during deposition, droplet impact force, and instrument vibration result in the formation of an intermediate Wenzel-CB state.<sup>70</sup> In these non-ideal scenarios, several works indicate that APCA is primarily governed by the physical interactions and geometry at the TCL rather than the macroscopic solid-liquid contact area.<sup>71–73</sup> Gao and McCarthy<sup>74</sup> reported that the major limitation of the Wenzel and CB models is the exclusion of the influence of TCL, adding that the factors  $r$  and  $\lambda_s$  in eqn (2) and (5) can be attributed globally only if the surface is isotropic. Moreover, unlike liquid molecules, solid atoms at interfaces are somewhat restricted and cannot be rearranged to form a true equilibrium surface structure. This physical restriction challenges the direct application of eqn (2) and (5) to real scenarios, as these equations depend rigidly on the principle of surface area minimization.<sup>45</sup>

However, for measuring the APCA as the governing parameter, the TCL introduces new complexities in the description of rough surfaces. In a completely penetrated Wenzel state, changes in the contact angle occur through the movement of the exterior contact line at the droplet periphery. Conversely, in the CB state, multiple interior contact lines coexist beneath the droplet. While the stability of  $\theta$  is governed by the minimized energy state along these interior lines, and shifts in the exterior TCL or transitions between CB to Wenzel states alter both the solid-liquid contact area and the measured APCA.<sup>73</sup> Hence, identifying the droplet perimeter alone as the TCL is insufficient; the internal contact line geometry beneath the droplet must also be considered. Experimental validations comparing CB and intermediate-state droplets confirm that the outermost TCL determines the measured APCA, whereas the contact area enclosed within the droplet is largely irrelevant, and droplets sharing the same outermost TCL configuration exhibit nearly identical  $\theta$ , regardless of differences in the internal wetting state beneath the droplet.<sup>70</sup> The theoretical and experimental findings indicate that the outermost TCL plays an important role in establishing interfacial equilibrium, whereas the interior contact area contributes only marginally to the apparent wetting behavior. Despite recent progress in understanding the wetting behavior of a wide range of surfaces, the absence of a comprehensive theory relating the geo-

metry and chemical heterogeneity of the TCL to the measured APCA remains a fundamental gap.

This theoretical shortcoming becomes even more critical when transitioning from equilibrium to kinetic regimes. Because classical macroscopic models fail to capture the interactions at the TCL even in static cases, they are fundamentally unequipped to describe systems where the TCL is forced into motion. When a droplet spreads, recedes, or is driven across a surface, the observed dynamic contact angle ( $\theta_D$ ) deviates further from equilibrium due to energy dissipation at the moving TCL. Understanding this dynamic behavior needs shifting focus from surface area minimization to the classical models of dynamic wetting as discussed in section 2.5.

#### 2.5 Understanding dynamic wetting

As established in comprehensive reviews of wetting and spreading,<sup>75</sup> the motion of the TCL is governed by the capillary forces and resistive dissipative forces. The force dissipation mechanisms and boundary dynamics are described through the following theoretical frameworks.

**2.5.1 The hydrodynamic model.** The classical hydrodynamic model treats the liquid as a continuum and attributes the deviation of  $\theta_D$  to viscous dissipation within the bulk liquid. As the fluid flows near the moving TCL, viscous friction causes the liquid-vapor interface to bend. The most widely used expression of this macroscopic bending is the Cox-Voinov law<sup>76</sup> shown in eqn (7), which relates the cube of  $\theta_D$  to the capillary number ( $Ca$ ).

$$\theta_D^3 = \theta_s^3 \pm 9 \cdot Ca \cdot \ln\left(\frac{L}{L_m}\right) \quad (7)$$

Here,  $\theta_s$  is the static contact angle,  $L$  is a characteristic macroscopic flow length, and  $L_m$  is a microscopic slip length. High-resolution experiments such as micro-particle image velocimetry ( $\mu$ -PIV) show that classical hydrodynamic models fail to capture complex three-dimensional interfacial curvature and often require non-physical slip lengths. To address these limitations, recent modifications incorporate CAH and replace the artificial slip parameter in eqn (7) with a precursor film model, resulting in a modified expression for the advancing  $\theta_D$  as shown in eqn (8),

$$\cos \theta_D - \cos \theta'_A = \frac{2Ca}{\beta} \frac{\sin^2 \theta_D}{(\sin \theta_D \cdot \cos \theta_D - \theta_D)} \quad (8)$$

where  $\theta'_A$  is the initial ACA with hysteresis effect,  $\beta = \lambda/c$  is a fitting factor that relates the precursor film length to a stress proportionality constant  $c$ , and  $\lambda$  is the characteristic parameter that propagates ahead of the macroscopic contact line.<sup>77</sup>

**2.5.2 Molecular-kinetic theory (MKT).** In contrast to the continuum-based hydrodynamic approach, which attributes energy loss to bulk fluid viscosity, the Molecular-Kinetic Theory (MKT) formulated by Blake and Haynes<sup>78</sup> focuses exclusively on the non-hydrodynamic energy dissipation occurring directly at the solid-liquid interface. MKT treats the movement



of the three-phase contact line not as a fluid flow, but as a rate-activated statistical process. It envisions the advancing or receding contact line as a series of discrete, thermally activated jumps of liquid molecules between adjacent adsorption sites on the solid surface. When the contact line is at rest, the molecules jump forward and backward at an equal equilibrium frequency ( $\kappa_0$ ). When driven out of equilibrium, the out-of-balance capillary forces bias these jumps in the direction of motion. The fundamental equation of MKT relates the macroscopic velocity of the contact line ( $u$ ) to the  $\theta_D$  through these molecular parameters:

$$u = 2\kappa_0\lambda \sinh \frac{\gamma\lambda^2(\cosh \theta_0 - \cos \theta)}{2\kappa_B T} \quad (9)$$

where  $\lambda$  is the distance between adsorption sites (the jump length),  $\gamma$  is the liquid–vapor surface tension,  $\theta_0$  is the static equilibrium contact angle,  $\kappa_B$  is the Boltzmann constant, and  $T$  is the absolute temperature.<sup>79</sup> While the MKT explains dynamic wetting behavior quite well by linking the macroscopic contact angle directly to molecular-scale surface diffusion and the work of adhesion ( $W_{ad}$ ), its classical form completely ignores bulk viscous dissipation. Consequently, comprehensive models in modern literature frequently combine MKT with the hydrodynamic model to account for both localized contact line friction and bulk viscous bending across different velocity regimes. The experimental techniques used to measure the static and dynamic  $\theta$ s will be discussed further in section 3.

Combined dynamic models provide mathematical framework for ideal substrates, relying on macroscopic  $\theta$ s, whether static or dynamic; however, they still present fundamental limitations for real materials with anisotropic wetting behavior, which introduces complexities in describing true interfacial physics. The physical and geometric limitations motivate the need for alternative descriptors to capture solid–liquid interfacial thermodynamics, as explored in the following subsection 2.6.

## 2.6 Thermodynamic and molecular descriptors of wettability

The limitations of contact angle resolution motivated researchers to develop alternative parameters to provide a more comprehensive understanding of solid–liquid affinity. These descriptors can be divided into two categories: thermodynamic quantities calculated from interfacial free energies, and molecular-level structural parameters obtained from simulations or experiments. The  $W_{ad}$  is one of the most fundamental thermodynamic parameters that represent the work per unit area required to separate a liquid from a solid surface in a reversible path.<sup>63</sup> The classical expression for  $W_{ad}$  is given by the Young–Dupre equation<sup>36</sup> as follows:

$$W_{ad} = \gamma_{LV}(1 + \cos(\theta)) \quad (10)$$

where  $\gamma_{LV}$  is the liquid–vapor surface tension, and  $\theta$  is the contact angle. By combining eqn (1) and (10), we obtain:

$$W_{ad} = \gamma_{SV} + \gamma_{LV} - \gamma_{SL} \quad (11)$$

$W_{ad}$  is more useful than  $\theta$  in the sense that it remains meaningful even when the contact angle approaches zero.<sup>63</sup> For highly wettable surfaces, while  $\theta$  saturates and loses sensitivity,  $W_{ad}$  continues to increase, which helps differentiate interfaces demonstrating almost identical contact angles. Moreover,  $W_{ad}$  is less dependent on  $\gamma_{LV}$ , which can vary between different water models in simulations; thus, it is more related to the solid–liquid interaction.<sup>80,81</sup>

In addition, we can express each interfacial tension as  $\gamma = \Delta F/A$ , where  $\Delta F$  represents the Helmholtz free energy associated with forming the interface, and  $A$  is the interfacial area.<sup>82</sup> Hence,  $W_{ad}$  inherently includes an entropy term as the free energy contains both energetic and entropic contributions ( $F = U - TS$ ). Studies based on first-principles MD showed that this entropic contribution can be significant, *e.g.*, in palladium–water systems, the entropy term is found to lower the solid–liquid interfacial tension by a measurable amount.<sup>82</sup> This ultimately increases the inferred  $W_{ad}$ . Therefore, energy-only approaches that ignore this term can inaccurately evaluate surfaces having similar interaction energies yet different interfacial entropies.<sup>82</sup>

Another useful descriptor that is often used in molecular simulations is the minimum of the solid–liquid interaction potential,  $E_{min}$ .  $E_{min}$  can be obtained from an adsorption–energy curve by placing the liquid molecule near the surface and recording the deepest point of the distance *vs.* energy attraction well. For water on graphitic carbon, where the interaction is largely nonreactive and dominated by dispersion and short-range repulsion, a linear correlation has been observed between  $W_{ad}$  and  $E_{min}$ .<sup>39,60,83,84</sup> However, this correlation does not apply to all interfacial properties. For instance, thermal boundary conductance does not show any clear correlation with  $W_{ad}$  and  $E_{min}$ .<sup>60,85</sup> Hence, neither  $W_{ad}$  nor  $E_{min}$  alone explains properties that depend on interfacial structure and dynamics.

Other molecular level wettability descriptors include the interfacial liquid layering. On hydrophilic surfaces, the liquid density profile typically exhibits pronounced oscillations. A sharp first peak is observed that indicates an ordered adsorption layer where molecules occupy preferential positions.<sup>62</sup> Alternatively, on hydrophobic surfaces, the first peak is broader and less intense, and a region of reduced density may appear between the surface and the bulk liquid.<sup>62</sup> However, as discussed above, the specific shape of the density profile depends not only on the solid–liquid interaction strength but also on the atomic structure of the surface. The hydrogen-bond network topology is another relevant factor, which indicates how water molecules coordinate with each other and with surface sites.<sup>86</sup> Near a surface, this network is more disrupted than the bulk water, and quantifying the average number of hydrogen bonds per molecule, their orientation, and their lifetime can reveal how strongly the surface perturbs the liquid structure.<sup>63,87</sup> The effect of these structural and dynamic descriptors on wettability is examined through MD simulations in section 4 and through first-principles calculations in section 5.



### 3. Experimental approaches to measuring wettability

#### 3.1 Contact angle measurements

Contact angle measurement is one of the most common methods for understanding surface wettability. As discussed in section 2, Young's equation provides a foundational principle to quantify the static  $\theta$ , assuming the solid surface is in an ideal condition (perfectly smooth, rigid, homogeneous, and non-reactive to the contacting liquid). With these assumptions, experimental measurements should provide value of  $\theta$  for the surface. To study this wide range of wettability through  $\theta$  measurement, there are two main surface-wetting characterization methods available: the optical or direct method and force-based or indirect methods.<sup>88</sup>

**3.1.1 Optical methods: sessile drop method.** Among the direct methods to measure  $\theta$ , sessile-drop goniometry is one of the most used due to its simplicity. Sessile-drop goniometry is an optical imaging method, where a water droplet on a solid surface is recorded, and the  $\theta$  from the image is measured by following eqn (1) (Young's equation). The experimental measurements of  $\theta$  have shown its dependency on several variables, such as surface cleaning, droplet volume, and the time of measurement.<sup>89</sup> These variables hamper the finding of a reproducible true equilibrium  $\theta$ ; instead, the sessile droplet method incorporates the RCA and ACA, occupying any of the local minimum energy states within the CAH range, representing a metastable state. Drelich<sup>90</sup> cited that these quasi-static measurements are more reproducible and accurate than the static  $\theta$  measurements. Part of his contributions included a detailed experimental procedure for measuring RCA and ACA. However, the effects of the chemical composition and surface geometrical structure on wetting properties were not discussed. Kung *et al.*<sup>47</sup> provided a detailed overview of the sessile droplet  $\theta$  measurements technique. They reported that the reliability of the sessile drop method is constrained by metastability, size effects, model inconsistencies, and optical limitations.

In practice, the sessile droplet method is often implemented with other advanced imaging techniques to overcome such limitations. For example, Santini *et al.*<sup>91</sup> combined X-ray micro-computed tomography (microCT), and the sessile droplet technique to reconstruct the three-dimensional drop surface and to measure the  $\theta$  of a complex opaque geometry at a high resolution. In addition, the droplet size dependency across macro to nano scale on  $\theta$  measurements is another limitation of the sessile droplet method. At the microscale, evaporation of the sessile droplet occurs significantly and cannot be neglected, which eventually changes the volume of the droplet during the observation period.<sup>42</sup> To directly visualize and measure droplets resolving the evaporation issue, Park *et al.*<sup>92</sup> used a cryogenic-focused ion beam (FIB) milling and the SEM imaging technique (cryo-FIB/SEM), which is advantageous in decreasing the evaporation effect using a rapid freezing rate. Their findings indicate that at larger scales, sur-

faces exhibit hydrophobic behavior, gradually evolving into superhydrophobic at the submicron range, where a nonlinear dependence between the cosine of contact angle and contact line curvature is reported.

**3.1.2 Optical methods: tilted plate method.** In addition to sessile  $\theta$ , dynamic (ACA and RCA)  $\theta$  provides a more informative measurement of surface wettability as discussed in section 2.6. The dynamic  $\theta$  can be determined using methods such as the tilting plate or volume-change techniques discussed in ref. 93 and 94. Gao and McCarthy<sup>74</sup> reported on the interactions between Teflon and water to show the role of dynamic  $\theta$  in wettability. The authors proposed the concepts of shear and tensile hydrophobicity based on ACA and RCA to explain the contrasting results from sessile  $\theta$ . Shear hydrophobicity is related to droplet roll-off, which can be quantified using the Furmidge equation<sup>95</sup> by predicting the tilt angle, whereas tensile hydrophobicity represents the  $W_{ad}$ , dependent on RCA. These parameters underscore the role of hysteresis as a more important metric than absolute  $\theta$  in evaluating hydrophobicity. However, as for the sessile  $\theta$ , measurements of the dynamic  $\theta$  could also be complicated by contact line pinning and the restricted smooth droplet motion, surface heterogeneity, and sensitivity to droplet size.<sup>93</sup> Consequently, while the dynamic  $\theta$  provides deeper insight into wetting and adhesion, its evaluation could be experimentally challenging due to the complexities linked to the measurements reproducibility. Moreover, the theoretical foundations of dynamic  $\theta$  remain debated.

Several studies have been conducted to address the reproducibility issues observed in the measurements of the static  $\theta$  and dynamic  $\theta$ . Huhtamäki *et al.*<sup>88</sup> presented a detailed protocol for reliable and reproducible  $\theta$  measurements, minimizing the systematic and random errors. The protocol further provides practical guidance on droplet size selection, equipment setup, curve fitting (Young-Laplace, circle, polynomial, spline), and sample preparation. They also noted that reproducibility depends on the strict control of experimental parameters. The authors further recommended to focus on the reproducible parameters ACA, RCA, and CAH, obtained by gradually increasing or decreasing droplet volume.<sup>90</sup> Although ACAs and RCAs are often considered dynamic, they are more accurately described as quasi-static values. Since true dynamic  $\theta$  occur only under continuous contact line motion, such as spreading or flow, and are dependent on the velocity and dissipation mechanisms.<sup>96</sup>

**3.1.3 Forced-based method: Wilhelmy balance method.** The complex experimental procedure for the tilted plate method hinders the reproducibility of the measured dynamic  $\theta$ . Alternatively, the Wilhelmy method provides a fully automatic, comparatively simple, and reproducible technique with precise control over kinetic parameters, *e.g.*, immersion speed. This method was broadly discussed by Volpe *et al.*<sup>97</sup> The mechanism involves immersing a thin, rigid, and symmetrically shaped plate or fiber into a liquid. Then the force balance acting at the solid-liquid-vapor interface is recorded with a sensitive microbalance. By applying the Wilhelmy equation,



formulated in eqn (12), the method determines ACA and RCA from the measured force.

$$F_m + F_C + F_B + F_g = 0 \quad (12)$$

In eqn (12),  $F_m$ ,  $F_C$ ,  $F_B$ , and  $F_g$  are the measured, capillary, buoyancy, and gravitational forces, respectively. Further studies by Karim and Kavehpour<sup>98</sup> demonstrated that the conventional force balance, shown in eqn (12) and accounting for capillary force, buoyancy, and the weight of the plate, is fundamentally incomplete. This is because the viscous forces acting on the moving plate are not taken into consideration. To demonstrate this limitation, a series of experiments were conducted, and true dynamic  $\theta$  were measured using an independent optical method, showing a discrepancy in the measured parameters. Thus, it was confirmed that neglecting the viscous force introduced a substantial error.

To address this issue, Karim and Kavehpour<sup>98</sup> proposed a modified force balance, depicted in Fig. 6 and described by eqn (13), incorporating the theoretical viscous force model ( $F_v$ ) derived from boundary layer theory, where  $F_v$  is positive for ACA and negative for RCA.

$$F_m - F_C + F_B - F_g + F_v = 0 \quad (13)$$

Karim and Kavehpour<sup>98</sup> used a thin glass plate, which was immersed in a silicone and glycerin (with different viscosities) pool to determine how liquid viscosity and immersion speed affect dynamic  $\theta$ s. While they modeled both ACA and RCA, they experimentally validated only the ACA. For low viscosity silicone, the authors reported ACA values from 17° to

69°, whereas for glycerin, this range was 34° to 63°, and for high viscosity silicone, a range of 57° to 115° was reported. However, the authors also noted a significant limitation to their proposed correction. The viscous force term in the model depends on the slip length and capillary number. Therefore, to apply this correction, the precise value of the slip length is required, and the sample must have the same composition and morphology on all surfaces. The relationship between the measured force and the obtained dynamic  $\theta$  depends on the length of the contact line, which may be complicated to determine for rough surfaces. Despite these challenges, the Wilhelmy method remained one of the most reliable techniques in surface wettability characterization, especially when corrections were applied. Table 1 compares the advantages and limitations of the methods described briefly.

Both the static and dynamic  $\theta$  measurement techniques have been well developed over the years, as discussed above. Furthermore, these methods are widely used due to the simple experimental procedure of direct methods like the sessile droplet or tilting plate methods. However, these direct approaches often suffer from limited resolution due to the simplified algorithms and formulas used for fitting droplet profiles. Indirect techniques like the Wilhelmy plate method offer a highly versatile alternative for characterizing dynamic wetting behavior.<sup>99</sup> However, this method fails to provide visual feedback on how wetting occurs or provide information on surface roughness.<sup>88</sup> Moreover, in the submicron (below 100 nm thickness), a transition region can be observed with a varying micro contact angle instead of the concept of a single

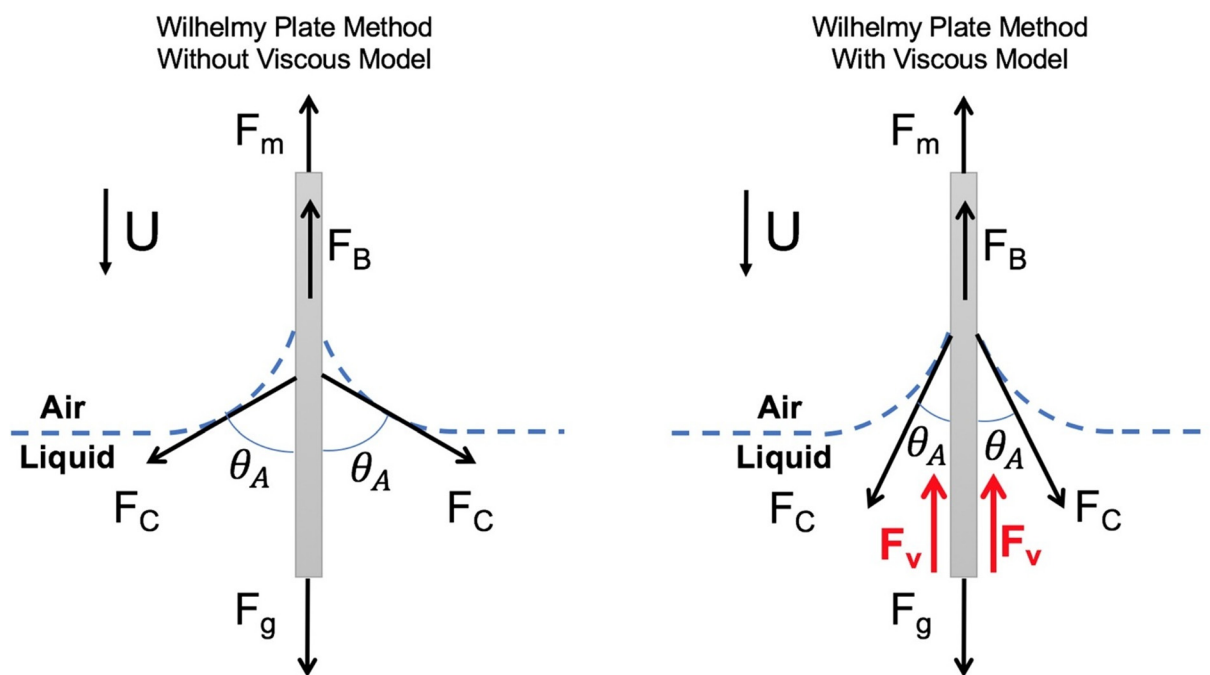


Fig. 6 Effect of viscous force on dynamic contact angle measurement using the Wilhelmy plate method. Reproduced with permission from ref. 98. Copyright 2018 Elsevier.



**Table 1** A brief comparison between the sessile droplet, the tilted plate, and the Wilhelmy plate methods

Method	Description	Advantages	Limitations
Sessile-drop	ACA and RCA are measured by increasing the volume of the droplet.	Simple to execute and compatible with samples with a small surface area	Prone to operator errors, time-consuming, and sensitive to impurities.
Tilting plate	The leading and trailing edges of a distorted droplet on a tilted surface make a sliding angle, which can be measured as a droplet mobility parameter	Simple and less time-consuming	No true indication of ACA and RCA can be obtained; thus, contact angle hysteresis cannot be identified.
Wilhelmy plate	A thin plate of the sample surface is immersed in the liquid, and dynamic $\theta$ s can then be measured from the cumulative calculated force.	Automated, prone to less human error, and large area wettability information can be obtained in less time.	Homogenous sample composition is required morphologically, faces hardship in measuring rough surfaces, and no information on surface uniformity can be gathered.

macro contact angle. Thus, conventional optical approaches cannot access this micron region, where intermolecular forces become dominant.<sup>100</sup>

Theoretical models of interfacial wetting through  $\theta$  were initially developed around the assumption of ideal macroscopic surfaces. Nonetheless, real-world surfaces deviate significantly from these ideal scenarios, introducing limitations to conventional measurement techniques. For example, the optical methods may provide a distorted TCL approximation due to diffraction and scattering, causing errors in the evaluation of  $\theta$ .<sup>101</sup> Moreover, for highly rough surfaces, finding out the contact points of a projected drop shape on the contact line is complex due to gravity-induced drop sagging of the droplet near the tangent line, which was reported by Dorrer and R uhe.<sup>102</sup> They further commented that for surfaces with large angles ( $\theta \sim 180^\circ$ ) showing superhydrophobicity, various existing Young–Laplace fitting equations can cause an underestimation of the true contact angle. Additionally, these macroscopic techniques often fail to capture local variations in wetting by chemical heterogeneity or surface texture.<sup>103</sup> The following section describes some advanced methods for characterizing wettability and surface roughness throughout the literature, addressing these limitations.

### 3.2 Surface characterization techniques: AFM, ESEM, and LSCM

Atomic Force Microscopy (AFM) is one of the most popular surface characterization methods, featuring sub-micron level resolution to directly scan the liquid film near the contact line. Thus, AFM can, in general, reveal important surface features with a higher level of accuracy and resolution than optical methods, but limitations can arise. In an early work, Wang *et al.*<sup>104</sup> applied digital microscopy and non-contact mode AFM (NC-AFM) to measure macro and micro wetting  $\theta$ s of water droplets on various metal surfaces, *e.g.*, chromium, nickel, iron, and their oxides. The authors defined the  $\theta$ s measured by the conventional digital microscope as macro-wettability, while  $\theta$ s measured by AFM was referred as micro-wettability. The comparative study revealed that the micro-wettability was consistently higher than the macro-wettability measured by conventional optical methods on the same surfaces. The authors correlated the changes to the chemical com-

position of the surface, such as wet polishing, air oxidation, and pure water immersion. The authors also reported a large degree of scattering and significantly more stable droplets in the micro-wetting case. The study highlighted that AFM could not accurately scan the profile of droplets with  $\theta$  greater than  $90^\circ$  because the cantilever used was unable to scan the lower part of the water droplet, limiting the analysis mostly to hydrophilic metal surfaces.

While Wang *et al.*<sup>104</sup> reported the differences between the macro and microscale measurements of wettability, in a later study, Checco *et al.*<sup>105</sup> explained the physical mechanism behind these differences by implementing NC-AFM on several methyl-terminated substrates or self-assembled monolayers or SAM (*e.g.*, alkyltrichlorosilanes on silica, alkylthiols on gold, alkyl chains on hydrogen-terminated silicon, and crystalline hexatriacontane chains on silica). The authors showed that mesoscale heterogeneity is one of the dominating factors, in addition to the line tension (arising from dispersive solid-liquid interactions), for the observed differences in wettability measurements. Moreover, they reported that this purely dispersive interaction, where the vdW interaction is the only significant force, is negligibly small for contact line curvature less than  $10 \mu\text{m}^{-1}$ . It is noteworthy that this study involved the partial wetting of SAMs on these organic monolayers, where all measured  $\theta$  were in a hydrophilic state, and did not encounter the limitations associated with measuring hydrophobic ( $\theta > 90^\circ$ ) systems. To address the issue with the hydrophobic surface  $\theta$  measurement, Nguyen *et al.*<sup>106</sup> continued with the idea that the contact angle measurement is fundamentally dynamic, and not static. The authors attached a spherical solid polyethylene particle to the cantilever of the AFM and measured the interaction force with a submerged air bubble. Their goal was to measure the interaction forces between the particle and the surface to calculate  $\theta$  indirectly from the force–distance curve. The authors specified that the measured value corresponded to the RCA, as it was determined during the piezoelectric translator approach and penetration into the bubble. It was observed that RCA changed significantly with the translator speed of the AFM. Due to the dynamic effects and uncertainty of contact line pinning, the authors were skeptical about whether the measured  $\theta$  could be a true representation of the intrinsic hydrophobicity of the surface.



It is necessary to understand the behavior of the liquid film near TCL for a comprehensive idea of wetting. Targeting this, Yu *et al.*<sup>107</sup> attempted a state-of-the-art tapping mode AFM (TM-AFM) technique near the contact line, revealing droplet film-TCL features such as film profile and  $\theta$ . To analyze a wide range of  $\theta$ , two distinct substrates, high-surface-energy mica and low-surface-energy polystyrene, were considered, and both surfaces were wetted with glycerol. The authors applied the direct optical method and the AFM in sequence to measure  $\theta$  on these surfaces and found a very good agreement between the methods, as shown in Table 2. Moreover, by scanning across the contact line with AFM, at a distance of several to tens of microns from the contact line, a highly linear film profile was observed. However, in the immediate vicinity of the contact line (film thicknesses below  $\sim 100$  nm), a non-linear transition region was found, where the concept of a single macro contact angle is invalid.

Deng *et al.*<sup>108</sup> also used TM-AFM for the first direct measurement of water droplet equilibrium  $\theta$  on the surface of rough quartz grains found in natural sand rocks. Previous studies were focused on idealized, smooth, artificial mineral crystals; however, this work addressed a significant gap in wettability research by studying mineral surfaces found in real reservoirs, given that traditional optical methods are unsuitable for micro-sized mineral surfaces. The authors studied asymmetrical water micro-droplets on the natural quartz with contact lines displaying imperfect curvatures and observed variations of  $\theta$  along the contact line of a single droplet ranging from 27.8° to 50.3°. The authors attributed these variations to the surface roughness, chemical heterogeneity, and the atomic arrangement of the quartz crystal face. In a recent study, Huo *et al.*<sup>109</sup> performed a micro-scale investigation on

shale reservoir rock employing a dual-method approach by combining the sessile drop contact angle method and AFM visualization. For direct comparison of wettability, the authors defined two dimensionless wettability indices:  $W$ , based on the sessile drop, and  $I$ , derived from AFM adhesion force measurements; these parameters are defined in eqn (14) and (15), respectively.

$$W = (\theta - 90^\circ)/90^\circ \quad (14)$$

$$I = (F_{os} - F_{ws})/(F_{os} + F_{ws}) \quad (15)$$

Here,  $F_{os}$  and  $F_{ws}$  are the oil–solid and water–solid adhesion forces, respectively. It was concluded that both the AFM ( $I$ ) and sessile drop ( $W$ ) indices highlighted oil-wet behavior of the surfaces. However, the sessile drop method could not capture the true degree of oil-wetness compared to AFM. This discrepancy was attributed to the roughness of the surface, given that rougher and organic-rich areas on the shale surface were more prone to oil adhesion than smoother regions. Moreover, the study indicated that surface roughness can trap air pockets, preventing the water droplet from fully contacting the solid. Thus, the nanoscale AFM probe provided a more precise and better assessment of the wettability by addressing the impact of surface roughness. Table 2 summarizes some of the corresponding contact angle measurements for different materials by implementing AFM contact measurements in the literature:

Recent studies have been using AFM to directly quantify the internal nanoscale phenomena, such as local adhesion forces, the role of surface heterogeneity, and the structure of the interface, which can provide a more fundamental understanding of wettability. For example, Castillo *et al.*<sup>110</sup> applied contact mode

**Table 2** Summary of  $\theta$ s measured from macroscopic and AFM-based micro/nano-scale methods

Study	Liquid	Solid substrate	Method	Measured contact angle(s)
Wang <i>et al.</i> <sup>104</sup>	Pure water	Pure Cr	Macro (digital microscope)	64–78° (depending on surface treatment)
		Pure Ni	Micro (AFM)	8–60° (max scatter range)
			Macro (digital microscope)	64–72° (depending on surface treatment)
		Pure Fe	Micro (AFM)	10–35° (max scatter range)
			Macro (digital microscope)	66–96° (depending on surface treatment)
SUS304 steel	Micro (AFM)	10–22° (wet polished only)		
	Macro (digital microscope)	64–68° (depending on surface treatment)		
	Micro (AFM)	2–38° (max scatter range)		
Nguyen <i>et al.</i> <sup>106</sup>	Deionized water	Polyethylene (PE) particle	Macro (sessile drop on flat PE)	92° (ACA), 67° (RCA)
Checco <i>et al.</i> <sup>105</sup>	<i>n</i> -Alkanes	(Octadecyltrichlorosilane (OTS) on silica)	Micro (colloidal probe AFM)	19.5–41.5° (RCA)
			Macro (goniometer)	43° (ACA)
		Dodecanethiol (DT) on ultra-flat Au	Nano (AFM)	7–25°
Yu <i>et al.</i> <sup>107</sup>	Glycerol	Mica	Macro (goniometer)	45° (ACA), 41° (RCA)
			Nano (AFM)	15–29°
		Polystyrene (PS)	Macro (optical method)	17 ± 1°
			Micro (AFM)	16.958 ± 0.005°
Deng <i>et al.</i> <sup>108</sup>	Water	Natural, rough quartz in reservoir rock	Macro (optical method)	67 ± 2°
			Micro (AFM)	67.965 ± 0.018°
			Micro (AFM)	27.8–50.3°
Huo <i>et al.</i> <sup>109</sup>	Distilled water	Shale reservoir rock	Macro (sessile drop)	112.3° to 133°



AFM to determine the nanoscale adhesion forces, surface topography, and morphology of SiO<sub>2</sub> nanoparticles. Their goal was to create superhydrophobic surfaces with silica nanoparticles and analyze the wettability at both macroscopic and nanoscopic levels. The authors applied the sessile droplet method to measure the  $\theta$  at the macroscale and AFM for the nanoscopic level. The silica nanoparticles are inherently hydrophilic, but after modification by wet impregnation and grafting with stearic acid, the particles displayed hydrophobic and even superhydrophobic behavior, resulting in  $\theta$  values from 145 to 151°. A study presented by Wanli *et al.*<sup>111</sup> reported on the use of silica nanoparticles from rice husk (RH-SNP) to alter the wettability of mineral surface material, creating a hydrophilic surface with low  $\theta$  to improve enhanced oil recovery. Silica nanoparticles serve as a mask on the muscovite mineral surface, effectively modifying its wettability from an oil-wet to a water-wet state. To understand the implications for wetting behavior, the SCA measurement technique was implemented both in the presence and absence of RH-SNP. The study showed that RH-SNP can significantly stabilize the hydrophilicity of the surface; moreover, the adsorption of RH-SNP was also influenced by the brine solution they used. Interestingly, the presence of Ca<sup>2+</sup> ions served as an electrostatic bridge that promoted nanoparticle adhesion, resulting in enhanced stability of the hydrophilic wetting state. In these studies, sessile droplet method was applied to find the macroscale  $\theta$ , and for further understanding of the surface structure and physical interactions, AFM was implemented complementarily.

AFM provides a high-resolution imaging capability of the outer profile of a droplet near the TCL by scanning the cantilever tip directly over the sample surface. However, the actual solid-liquid interface underneath the droplet remains inaccessible to the probe. In this context, to visualize the solid-liquid interface beneath the droplet, laser scanning confocal microscopy (LSCM) can easily penetrate the transparent droplet and scan the interface by measuring the differences in optical reflection; thus, a 3-D image of the interface is created.<sup>112</sup> Hongru *et al.*<sup>113</sup> measured the Wenzel roughness factor ( $r$ ) to characterize superhydrophobic surfaces, showing that for texture-irregular surfaces with small roughness, LSCM measurements agreed with those obtained by AFM. The primary advantage of LSCM is its unique capability to characterize texture-irregular surfaces with large roughness, an area where AFM is inapplicable. However, the authors reported that the main limitation of the LSCM method is its resolution, which is dependent on the wavelength of the laser; therefore, the technique is effective for surfaces with micro or larger-sized textures but faces difficulties in characterizing nano-scaled structures. Haimov *et al.*<sup>114</sup> showed that LSCM allows direct visualization of hidden interfaces by using a confocal microscope with an immersion lens submerged directly within the water drop, which allowed them to analyze the Cassie-Baxter state shape. It was reported that the local mean curvature of the interface is constant and approaches zero at every point. The authors claimed that it was the first direct experi-

mental proof of theoretical predictions based on the Young-Laplace relation,

$$\Delta p = \gamma \left( \frac{1}{r_1} + \frac{1}{r_2} \right) \quad (16)$$

where,  $\gamma$  is the surface tension of the liquid-gas or liquid-liquid interfaces,  $r_1$  and  $r_2$  are the radius of curvature of the droplet. The term  $(1/r_1 + 1/r_2)$  is often referred to as mean surface curvature. While the mean curvature remained consistently near-zero, the standard deviation of the mean curvature increased with higher density and lower surface tension. This phenomenon was attributed to the interplay between the pressure difference at the interface and the surface tension. Furthermore, the researchers explored this behavior by varying the droplet density (using H<sub>2</sub>O-D<sub>2</sub>O mixtures) and surface tension (using water-ethanol mixtures). This work established a powerful method for *in situ* characterization and offered fundamental insights into the precise nature of the composite interface that defines superhydrophobicity. The study by Papadopoulos *et al.*<sup>115</sup> also provided time-resolved 3-D visualizations of superhydrophobicity by imaging the Cassie-to-Wenzel transition using LSCM of evaporating water droplets on polydimethylsiloxane (PDMS) micropillar arrays. The evaporation-induced transition of the water droplet changed the thickness of the air gaps, as shown in Fig. 7(a); the variation of the apparent contact angle with time is also shown in Fig. 7(b). It was evident that the ACA tends to decrease over time while transitioning from Cassey to Wenzel type wettability. Nonetheless, the main limitation of this procedure lies in the transparency of the substrate analyzed using LSCM.

Another method to measure  $\theta$  is the Environmental Scanning Electron Microscopy (ESEM), which applies high spatial resolution, allowing the implementation of smaller droplets to minimize gravitational distortion. This feature enables experimental study of phenomena like the line tension effect that are inaccessible with conventional goniometry.<sup>116-118</sup> Jenkins and Donald noted that, by condensing microdroplets directly on the surface,  $\theta$ s can be evaluated with improved accuracy, and the ability to image through the liquid phase enhances contact point and edge detection for  $\theta$  analysis.<sup>119</sup> ESEM has been successfully applied to dynamic wetting studies of superhydrophobic patterned surfaces,<sup>117</sup> real-time imaging of contact line structures, and investigations of line tension effects.<sup>120</sup> In fiber wetting studies, ESEM circumvents the distortions in sessile static  $\theta$  measurements caused by cylindrical geometries and avoids the uniformity requirements of Wilhelmy plate techniques.<sup>121</sup> One of the limitations of the ESEM method is that the detector observes the sample at an oblique angle rather than parallel to its surface, resulting in geometric distortion of the droplet profile in the acquired images. Consequently, the APCA measured from an ESEM imaging is not the true angle. To account for the sample tilting during the imaging process and correct the measured  $\theta$ , mathematical models have been proposed by Brugnara *et al.*<sup>122</sup> Their study made it possible to directly measure  $\theta$  on



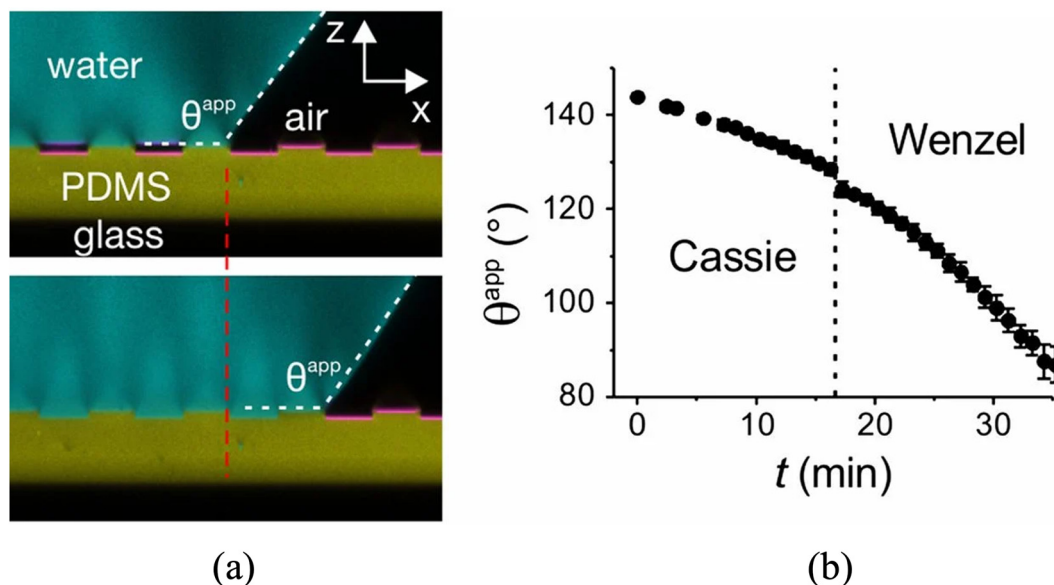


**Fig. 7** (a) Confocal microscopy section image of a water droplet before Cassie to Wenzel transition and after the Cassie-to-Wenzel transition, and (b) change of the ACA with time. Reproduced with permission from ref. 115. Copyright (2013) National Academy of Sciences.

micron range surface regions, showing a good agreement with the existing data from literature. Based on these mathematical models, Marbou *et al.*<sup>123</sup> attempted an *in situ* characterization of highly ordered pyrolytic graphite (HOPG) surface to successfully explain the graphite/graphene wettability alteration. Their observations provided evidence that the graphitic surface is intrinsically hydrophilic (with a measured contact angle as low as 37°). It was concluded that the hydrophobic behavior of graphite reported in the literature is caused by the presence of airborne contaminants on the surface. However, from the study of Brugnara *et al.*<sup>122</sup> and Marbou *et al.*,<sup>123</sup> it was clear that due to the heating effect of the electron beam on the surface as well as on the droplet, complexity arises in wettability measurement with ESEM. The heating effect causes drop shape deformation through condensation, evaporation, and coalescence. Therefore, it becomes necessary to control the environment (*e.g.*, temperature, pressure, and relative humidity) of the ESEM chamber, to reduce these beam-induced deformities. Moreover, it was also mentioned that for a smaller droplet (thickness <1 μm), it was not possible to measure the contact angle with enough accuracy due to distortion.

To address this issue, Barkay<sup>124</sup> proposed an indirect method for wettability analysis for smaller droplets (diameter <1 μm) by implementing wet scanning transmission electron microscopy (wet-STEM) in ESEM. By implementing this method, the 2-D map of electron intensity was obtained, as well as measurements of the intensity profile of the nanodroplet. To resolve the shape and  $\theta$ s of various shaped droplets, Monte Carlo simulations were applied. By fitting the experimental intensity profile to the simulated results, the 3-D geometry of the nanodroplet was determined, and  $\theta$ s were calculated. Alternatively, it has been shown that it is possible to cal-

culate  $\theta$  directly from experimental data through *in situ* condensation of water in the ESEM environment. For example, Körber<sup>125</sup> presented an ESEM technique to determine microscopic  $\theta$  on capillary building materials to understand their hydrophobicity. For *in situ* condensation of water vapor, the building material sample was first placed on a cooling table inside the ESEM chamber. The temperature and pressure of the ESEM chamber were controlled so that the vapor could condense into droplets on the sample surface. Then,  $\theta$  was determined by taking images of these droplets from the ESEM and analyzing the contour of the droplet using Drop Shape Analysis (DSA) algorithm. Moreover, Al-Naimi *et al.*<sup>126</sup> showed almost similar techniques for finding the microscopic wettability of carbonate rocks, under three conditions: natural, aged in crude oil, and aged in a cationic surfactant, by ESEM *in situ* condensation. Images of these condensed micro-droplets were captured through ESEM, and equilibrium  $\theta$  were measured using the ImageJ software. The authors also compared the results from ESEM with the macroscale  $\theta$ s found from sessile drop goniometry. It was reported that the micro-scale ESEM method captured the non-uniform wetting behavior properly, which was caused by the chemical and physical heterogeneity of the sample surface. Although ESEM provides a proper and versatile visualization of the surface wettability with high resolution image, its applicability is limited to water-based wetting experiments only.

### 3.3 Effects of surface heterogeneity and surface chemistry on wettability (other techniques: XPS, FTIR, Raman, NMR)

For a better understanding of surface chemistry, macroscopic surface characterization techniques such as X-ray Photoelectron Spectroscopy (XPS),<sup>127</sup> Nuclear Magnetic Resonance (NMR),<sup>128</sup> Fourier Transform Infrared Spectroscopy



(FTIR),<sup>129</sup> and Raman Spectroscopy (RS),<sup>130</sup> are some popular methods often listed in the literature. AFM can provide better surface physical attributes, while XPS, FTIR, NMR, or RS are ideal for providing chemical state information correlated with wetting behavior. XPS is significantly surface sensitive as the X-rays can penetrate micrometers deep into the sample, enabling the XPS method to provide information exclusively from the material surface, which is crucial to study properties such as wettability, adhesion, and for surface characterizations.<sup>131</sup> XPS provides quantitative elemental analysis of a surface, chemical state, and bond distinction, while other methods, such as FTIR, can be used to identify the presence of functional groups, *e.g.*, carboxyl, hydroxyl, or alkyl chains, and hydrogen bonding. For nanomaterial surface analysis, FTIR is usually applied in attenuated total reflection (ATR) or diffuse reflectance (DRIFTS) mode, giving the FTIR technique an advantage over XPS in studying liquid-nanoparticle interfaces.<sup>132</sup>

These methods are often implemented with other  $\theta$  measurement techniques to correlate the surface chemical compositions with wettability. Zhou *et al.*<sup>133</sup> analyzed the implementation of XPS on the evaluation of the effects of coal dust on the surface chemistry across different stages of geological formations. The SCA measurements were carried out using a technique similar to the sessile method between coal dust and water droplet, and the authors found that as coal changes from lignite to anthracite, the surface becomes less wettable. The  $\theta$ s for the deashed coal samples used for the XPS analysis ranged from 50.13° for the most wettable sample (Beizao Lignite) to 71.47° for the least wettable sample (Yangquan anthracite). This wettability alteration was associated with a decline in oxygen content and a corresponding decrease in the abundance of hydrophilic polar functional groups, including carboxyl and hydroxyl moieties. Similarly, Xu *et al.*<sup>134</sup> also found a consistent trend of decrements in the wettability as the metamorphic degree of coal increased. The static  $\theta$  was observed to rise from 47.05° to 72.88° as lignite transformed into anthracite, and to elucidate the microscopic origins of this enhanced hydrophobicity, XPS and NMR techniques were employed. NMR characterized the carbon skeleton to identify the carbon-containing groups, especially the increase in aromatic carbon groups, which showed a strong correlation with the  $\theta$ . On the other hand, XPS was used to analyze the surface chemistry and quantify the effects of oxygen-containing functional groups on  $\theta$ . Their result also denoted hydroxyl groups as a significant contributor to wettability by enhancing hydrophilicity. The authors concluded that the poor wettability of high-ranked coal was caused by the increased hydrophobic aromatic C structures and the loss of strong hydrophilic groups, *e.g.*, hydroxyls.

Woche *et al.*<sup>135</sup> also used XPS to link wettability to the surface elemental composition. The authors demonstrated that the atomic surface O/C ratio could be a significant indicator of soil wettability. In this investigation, soil samples collected along the Damma Glacier chrono sequence exhibited a progressive change in surface wettability from completely wet-

table (0° contact angle) to subcritically wettable and ultimately to hydrophobic (98° contact angle) across an age span of 0 to 120 years. From XPS analysis, it was revealed that the C and N content of the soil sample progressively increased while the O content and mineral-derived cations (Si, Al, Ca) decreased with time. Consequently, the study established a strong negative correlation between the surface O/C ratio, which was also corroborated by measurements of samples obtained from different sources.<sup>136,137</sup> The authors concluded that the surface O/C ratio is a general parameter that could connect wetting properties and surface composition, especially for materials consisting of inorganic solid matter coated with organic components. This relationship showed validity for  $\theta$  in the range from 0° to around 120°, independent of surface roughness, which is another crucial physical property that affects both the adsorption capacity and wettability of materials.

Jiang *et al.*<sup>138</sup> further investigated the dependability of coal dust wettability on different functional groups by combining experimental analysis and MD simulations. In this process, bituminous coal was chemically modified to enhance the concentration of surface oxygen-containing functional groups (OFGs) and to examine their influence on wettability. FTIR and XPS analyses were used to identify and quantify the OFGs, respectively, and the  $\theta$  measurements were subsequently correlated with the variations in these groups. The initial  $\theta$  for the raw bituminous coal was around 92.47°, which decreased to 80.2° when the coal was modified with OFGs, making it more hydrophilic. On the other hand, the MD simulations were performed by grafting eight different functional groups on a graphene substrate to study the effect of each group on water molecule adsorption. The results confirmed that strong polar groups such as -COOH and -OH enhance hydrophilicity by promoting the formation of hydrogen bonding with water molecules. Thus, the water molecules spread out on the surface, resulting in a lower  $\theta$ . In contrast, non-polar groups like the alkyl groups (-CH<sub>3</sub>, -C<sub>2</sub>H<sub>5</sub>, and -C<sub>3</sub>H<sub>7</sub>) are bound through weaker vdWs interaction, increasing the hydrophobic nature with longer C chains. Yang *et al.*<sup>139</sup> investigated the surface wettability and hydrothermal stability of methyl-modified silica film, demonstrating that their hydrophobicity can be altered by tuning the surface chemistry. The authors mentioned that the water  $\theta$  could be significantly increased by increasing the concentration of the methyl groups on the silica surface. By applying vibrational spectroscopy methods, *e.g.*, FTIR and RS, direct evidence of this wettability modification was obtained. The substitution of polar hydrophilic hydroxyl groups with non-polar methyl groups was found to increase the contact angle from 46° to 98°, leading to a decrease in the overall surface energy of the silica films. Moreover, the modified silica films showed thermal stability up to a calcination temperature of 350 °C while still maintaining their hydrophobicity. However, after 400 °C, the methyl groups started to decompose, and the silica film turned hydrophilic again with a  $\theta$  around 25°. The influence of aging on the modified film was further evaluated, and the results showed that the methyl-



silica film preserved its hydrophobic character after one week, while the unmodified sample exhibited a reduction in  $\theta$  of about 32.6%.

An approach to control the graphene surface wettability was introduced by Vijayarangamuthu *et al.*<sup>140</sup> by applying an electrical bias across a single-layer graphene oxide (SLGO) to observe the reversible electromigration of oxygen adatoms. By using RS and 2-D Raman mapping, the migration of oxygen atoms was visualized, while XPS was used to confirm the presence of oxygen and quantify the changes in the C–O and C–C bonds, which served to validate the RS results. In the meantime, the SCA was measured. Their finding indicated that the static  $\theta$  decreased from  $\sim 76^\circ$  to  $\sim 67^\circ$  in the oxygen-rich region, making it more hydrophilic, whereas the oxygen-depleted region became more hydrophobic with an increase in the static  $\theta$  to around  $83^\circ$ . To minimize the effect of contamination, the experiments were conducted under vacuum after a nitrogen purge to avoid humid environments around the sample surface.

### 3.4 Experimental studies on metals, graphitic carbon, and oxides

Chow *et al.*<sup>141</sup> investigated the wettability of mono- and few-layered MoS<sub>2</sub> and WS<sub>2</sub> through RS and focused on the ACA, since a CAH of  $\sim 20^\circ$  suggested considerable variability in the static measurements. The wettability of the monolayer materials was measured on layers supported by SiO<sub>2</sub>/Si wafers. The bulk wetting behavior was approximated as the number of layers of 2-D material increased; after three layers, no significant differences were observed with respect to the bulk wetting behavior. The authors developed two models, dispersive-only and dipole–dipole-only interaction models, and these models were built using Hamaker's constants to find the energy interaction. Their findings indicated that experimental observations lie somewhere between dispersive-only and dipole–dipole-only behavior. Furthermore, aging effects were observed just as in the case of graphene; thus, MoS<sub>2</sub> and WS<sub>2</sub> are hydrophilic ( $\theta \sim 70^\circ$ ) and become hydrophobic after exposure to ambient conditions.

Kozbial *et al.*<sup>142</sup> provided a comprehensive overview of the wettability of graphitic carbon and graphene-coated surfaces, documenting the evolution in understanding from the traditional view of graphite as hydrophobic to recent evidence demonstrating the hydrophilic characteristics of carbon surfaces. Different measuring techniques have shown that hydrocarbons constitute the main form of contamination on carbon surfaces. Clean carbon surfaces exhibit approximately 20% polar contribution to their surface tension, reflecting an inherent affinity for water. This polar contribution is diminished when hydrocarbons are adsorbed on the surface. Furthermore, a number of studies have reported that hydrogen bonding plays a significant role in governing water–graphite interactions.<sup>143–145</sup> Moreover, Hong *et al.*<sup>146</sup> investigated the wettability of graphene-coated SiO<sub>2</sub>/Si substrate surfaces, noting the effect of hydrocarbon contamination. Nonetheless, unlike previous investigations, the authors suggested a modifi-

cation of the Fermi level as the origin of the hydrophilicity of graphene. For a hydrophobic condition, after applying a negative/positive voltage, the surfaces became hydrophilic and maintained that condition after the voltage was removed. Alternatively, for hydrophilic conditions, a  $\theta$  change was not observed after applying a voltage. Furthermore, DFT simulations showed that charged graphene layers (both electron-doped,  $-1e$ , and hole-doped,  $+1e$ ) generate a larger adsorption energy than neutral surfaces. This increased the surface interaction between water and graphene, thus enhancing the hydrophilicity of the charged graphene layer. The study concluded that both chemical modification and the application of electrical potential can increase the electron or hole density of states, thereby rendering the surface more hydrophilic. Ashraf *et al.*<sup>147</sup> conducted a similar investigation, reaffirming the reported findings. In this investigation, graphene was doped with both electron donors and acceptors to alter its electronic structure. This doping shifted the Fermi level, leading to enhanced hydrophilicity of the graphene-coated surfaces. In other words, the charge carrier density of graphene was modified by doping, resulting in a modification of the surface wetting and turning the substrate to display more hydrophilic behavior. In addition to doping, a metal–graphene heterojunction was also analyzed (graphene–gold), and the resulting  $\theta$  seemed to increase as the distance of the droplet from the metal–graphene junction increased, thus indicating that the presence of the metal changed the surface potential of graphene. DFT simulations demonstrated that doped systems displayed changes in their absorption energy and force potential. These values were subsequently used in classical MD simulations of droplet wetting, predicting an increase in hydrophilicity for doped surfaces relative to neutral graphene. This investigation highlighted that wetting transparency is governed more by the doping level of graphene than by the properties of the supporting substrate.

Terzyk *et al.*<sup>148</sup> further studied the wettability of hydrophobic (graphene and gold) and hydrophilic (polytetrafluoroethylene, PTFE) surfaces in the presence of airborne contaminants, to align the study with real-world environmental conditions. The authors demonstrated that the pristine surfaces of gold and graphene are both hydrophilic in nature; however, their wettability depends on the adsorption of airborne hydrocarbons (*e.g.*, *n*-decane, *n*-tridecane, and *n*-tetracosane). It was reported that static  $\theta$  increases non-linearly for both gold and graphene with the increment in the hydrocarbon concentration. For gold, the change was drastic, shifting from a complete wetting state ( $0^\circ$ ) to a hydrophobic state ( $110^\circ$ ). On the other hand, static  $\theta$  of PTFE decreased to a more hydrophilic state. The authors offered a two-state model based on classical thermodynamics to explain this phenomenon, where the contaminants mask the original surface by forming a stable monolayer under the droplet. The wettability of gold, specifically whether it is intrinsically hydrophilic or hydrophobic, has long been debated in the literature. Smith<sup>149</sup> addressed this controversy by examining the wettability of clean gold surfaces using Auger Electron Spectroscopy (AES) under ultra-high



vacuum conditions. Their results demonstrated that clean gold is intrinsically hydrophilic, with an SCA close to  $0^\circ$ . After exposure to atmospheric air, the angle increased significantly, leading the authors to conclude that the apparent hydrophobic behavior of gold originates primarily from carbonaceous contamination rather than from the gold surface itself.

The impact of airborne hydrocarbons on both metals and 2-D materials highlights a critical bottleneck in macroscopic experimental wetting studies. Because extreme conditions, such as ultra-high vacuum, are required simply to observe the true intrinsic wettability of a clean surface, isolating the solid-liquid interactions from environmental artifacts remains experimentally challenging. To bypass these environmental vulnerabilities and investigate the uncontaminated solid-liquid interface, atomistic computational methods could be a solution. These simulation techniques, *e.g.*, molecular dynamics, provide the controlled environments necessary to isolate and resolve the fundamental physics of wetting at the nanoscale, which serves as the focus of the following section.

## 4. Molecular dynamics models of wettability

### 4.1 Overview of simulation methods: droplet, film, and indirect techniques

As discussed in section 3, the characterization of surface wetting has been the focus of extensive studies, and multiple approaches have been proposed to quantify solid-liquid affinity. However, experimental methods remain constrained by several intrinsic limitations that hinder their ability to fully capture interfacial phenomena. Techniques such as sessile-drop goniometry, tilted-plate measurements, and even advanced imaging techniques like AFM, LSCM, and ESEM are often affected by contact-line pinning, metastable states, optical distortion, and surface contamination. Moreover, the determination of true equilibrium contact angles becomes increasingly challenging at micro- and nanoscale dimensions, where intermolecular and capillary forces dominate and the assumptions of continuum theory begin to fail.

To overcome these limitations, MD simulations have emerged as a powerful complementary tool for studying wettability at the atomic scale. By directly resolving molecular interactions and dynamic processes at the solid-liquid interface, MD simulations enable the quantitative evaluation of parameters such as contact angle, work of adhesion, interfacial density, and interfacial free energy with exceptional spatial and temporal resolution. These capabilities make MD methods indispensable for elucidating the microscopic origins of wetting behavior and for providing insights that remain inaccessible through experimental observation alone. Nevertheless, defining quantities such as the contact angle or the solid-liquid interfacial free energy at nanometric scales remains a subject of ongoing discussion, since curvature, line tension, and thermodynamic ensemble choice can yield non-unique interpretations. These conceptual aspects are revisited

in later sections, where the limitations and consistency of different definitions are analyzed in detail. Depending on the level of detail required and the target property of interest, MD simulations of wettability are commonly performed using three principal approaches: the droplet method, the film or slab method, and indirect free-energy-based techniques. Each of these methods provides complementary insights into the thermodynamic and structural characteristics of the solid-liquid interface, differing primarily in computational cost, the ease of interpretation, and sensitivity to finite-size effects.

Droplet-based MD simulations represent one of the most intuitive and widely employed approaches for characterizing wettability at the nanoscale, as these simulations closely replicate the classical sessile-drop experiments used in macroscopic measurements. In this technique, a nanometric droplet is equilibrated on a solid substrate, and the liquid-vapor interface is analyzed to determine the APCA from the equilibrium meniscus profile. One of the earliest and most influential implementations of this methodology was reported by Nijmeijer *et al.*,<sup>150</sup> who investigated the wetting and drying transitions of a Lennard-Jones fluid on an atomically smooth, inert wall. Their study demonstrated that contact angles extracted from the time-averaged density contour of the droplet were consistent with those obtained independently from interfacial-tension calculations, thereby validating the droplet-shape analysis as a robust measure of solid-liquid affinity in molecular simulations. Moreover, their results emphasized the need for long equilibration and sampling times to suppress capillary fluctuations and achieve accurate curvature determination. Beyond the equilibrium requirements of individual cases, reliable estimation of contact angles and interfacial energies generally demands extensive temporal averaging and ensemble sampling to suppress thermal noise and capillary-wave effects. In practice, convergence can require nanosecond-to-microsecond trajectories, particularly for droplets with slow relaxation dynamics or strong surface interactions. Building on this foundation, de Ruijter *et al.*<sup>151</sup> extended the droplet method to explore dynamic wetting phenomena by simulating the spontaneous spreading of Lennard-Jones droplets on solid substrates. Their simulations successfully captured the transition between molecular-kinetic and hydrodynamic regimes of contact-line motion and reproduced experimentally observed spreading behaviors, including Tanner's law and the predictions of the molecular-kinetic model. This work was among the first to demonstrate the capability of MD simulations to bridge microscopic and macroscopic descriptions of wetting, simultaneously resolving molecular displacement frequencies, interfacial frictional dissipation, and transient variations in the dynamic contact angle.

Subsequent advances by Werder *et al.*<sup>39</sup> further refined the droplet-based approach by calibrating the water-carbon Lennard-Jones cross-interaction parameters to reproduce experimentally measured contact angles on graphite surfaces. This calibration yielded one of the first systematic parametrizations of heterogeneous solid-liquid interactions, establishing



a benchmark that remains widely adopted in simulations involving graphitic and carbon-nanotube interfaces. Fig. 8(a) and (b) illustrate how Werder *et al.*<sup>39</sup> connected force-field parameter tuning to wettability on graphite. In their simulations, they observed that increasing water-carbon attraction linearly strengthens interfacial binding (Fig. 8(a)) and systematically reduces the droplet contact angle (Fig. 8(b)). Following this work, several studies extended droplet-based simulations to more complex wetting scenarios, including dynamic spreading, contact-line hysteresis, and metastable Cassie-Wenzel transitions. These developments bridged molecular and continuum descriptions of wetting and provided new insights into the role of interfacial friction and surface heterogeneity.<sup>152–155</sup> Most early MD studies adopted the spherical droplet geometry owing to its direct analogy with experimental sessile-drop configurations, while later variants introduced alternative geometries to minimize curvature effects (discussed further in section 4.2). Overall, the droplet method remains a cornerstone of nanoscale wettability studies due to its conceptual simplicity and close analogy with experimental observations. Nevertheless, it is intrinsically affected by finite-size and curvature effects, as well as by the presence of line tension, which can introduce notable deviations from macroscopic behavior. Consequently, accurate quantitative analysis often requires either explicit size corrections or extrapolation toward the macroscopic limit.

In contrast to the droplet configuration, the film or slab method eliminates the need to analyze a curved liquid-vapor meniscus by modeling a planar liquid film adsorbed on a solid substrate under periodic boundary conditions. The key quantities obtained are the  $W_{\text{ad}}$  and the solid-liquid interfacial free energy ( $\gamma_{\text{SL}}$ ), both extracted from potential-energy differ-

ences between bound and separated configurations or *via* equilibrium free-energy sampling. The total interaction energy is commonly decomposed into enthalpic ( $\Delta U_{\text{SL}}$ ) and entropic ( $T\Delta S_{\text{SL}}$ ) terms, providing a rigorous thermodynamic basis for wettability analysis.

The foundations for computing interfacial free energies *via* thermodynamic integration were established by Broughton and Gilmer,<sup>156</sup> who used cleaving potentials to reversibly separate crystal and melt phases. Later, Davidchack and Laird<sup>157</sup> subsequently refined the method by employing planar cleaving walls constructed from properly oriented crystal layers. Although developed specifically for crystal-melt interfaces, their framework provided a rigorous thermodynamic route to interfacial free energies and established key principles that inspired subsequent adaptations to general solid-liquid systems relevant to wettability. Building on the cleaving-wall concepts, Leroy *et al.*<sup>158</sup> developed a thermodynamic-integration framework to compute interfacial excess free energies for solid-liquid systems. Their goal was to compute a free-energy difference between the real solid-liquid system and a reference system where the liquid interacts with an unstructured repulsive wall. They implement this through a cleaving procedure in which repulsive walls move from inside the solid to a position where the liquid is separated from the solid, and the reversible work is obtained by thermodynamic integration. Subsequently, Leroy and Müller-Plathe<sup>159</sup> referred this thermodynamic integration approach as the “phantom-wall method” and utilized it to investigate the influence of surface topography on solid-liquid surface free energies. They explicitly studied how nanoscale roughness changes the computed solid-liquid surface free energy compared with smooth surfaces. They observed that roughness lowered the surface free

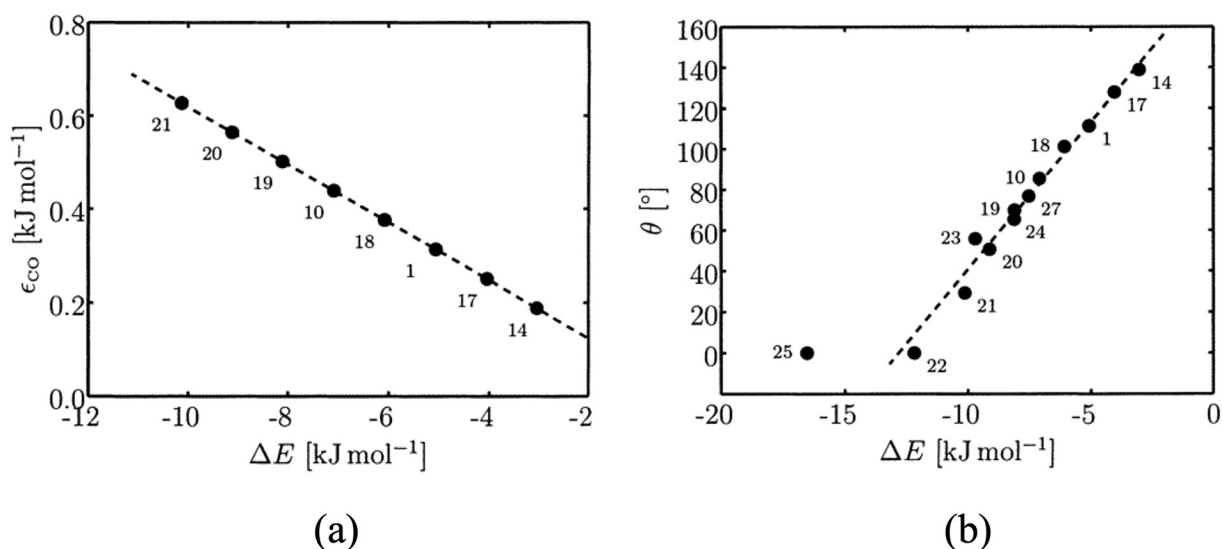


**Fig. 8** (a) Relation between different Lennard-Jones parameters  $\epsilon_{\text{CO}}$  considered in the study of Werder *et al.*<sup>39</sup> and the water monomer binding energy  $\Delta E$  on graphite. The numbers 14–21 denote different sets of interaction parameters considered by the authors. The dashed line is a linear fit to the data points. (b) Contact angle  $\theta$  of water droplets on graphite as a function of the binding energy  $\Delta E$  of a single water molecule obtained from different Lennard-Jones parameters considered by Werder *et al.*<sup>39</sup> The dashed line is a linear fit excluding the cases 22, 25, and 27. Reproduced with permission from ref. 39. Copyright (2003) American Chemical Society.



energy on surfaces with favorable liquid interactions while raising it on surfaces with weak liquid interactions. This finding is consistent with the macroscopic Wenzel framework. Fig. 9(a) illustrates the solid–liquid surface free energy difference as a function of groove number density for two solid–liquid interaction strengths ( $\Sigma = 0.6$  and  $\Sigma = 0.4$ ), illustrating that increasing roughness decreases  $\gamma_{SL}$  on strongly interacting surfaces while increasing it on weakly interacting surfaces.

As an alternative to the phantom-wall approach, Leroy and Müller-Plathe<sup>160</sup> introduced the dry-surface simulation scheme, which calculates the work of adhesion as the reversible work to turn off the attractive part of the solid–liquid interaction potential. This method employs thermodynamic integration to transform the actual solid–liquid interface into

an effectively repulsive (“dry”) interface. Their results demonstrated that  $W_{ad}$  (represented by  $-\Delta\gamma_{AB}$  in their formulation) varies nonlinearly with the solid–liquid Lennard-Jones energy parameter  $\epsilon_{SL}$  (see Fig. 9(b)), with values spanning from hydrophobic surfaces such as polymers and carbon materials ( $\epsilon_{SL} < 0.5 \text{ kJ mol}^{-1}$ ) to metallic substrates like gold ( $W_{ad} \sim 317 \text{ mJ m}^{-2}$ ). Consequently, the “dry-surface” method provides a continuous thermodynamic description of wettability from low-energy nonpolar surfaces to strongly interacting metals. Later, using the dry-surface method, Leroy *et al.*<sup>83</sup> established a relationship between the macroscopic  $W_{ad}$  ( $W_{SL}$  in their study) and the single-molecule adsorption energy, demonstrating that  $W_{ad}$  depends mainly on the effective binding energy  $E_{min}$  at the interface and that this relationship holds for water on



**Fig. 9** (a) Solid–liquid surface free energy difference as a function of the groove number density per unit area in rough surface systems (in reduced units). Reproduced with permission from ref. 159. Copyright (2010) AIP Publishing. (b) Variations of  $-\Delta\gamma_{AB}$  (equivalent to  $W_{ad}$ ) over the range of  $\epsilon_{SL}$  values considered in the study of Leroy and Müller-Plathe<sup>160</sup> using the “dry-surface” method. The dashed lines are guides to the eye. Reproduced with permission from ref. 160. Copyright (2015) American Chemical Society. (c) Schematic illustrating linear fits (dashed lines) to  $\cos\theta$  versus  $1/a$ .  $\theta$  is the contact angle and  $a$  is the radius of the 3-phase contact line. Reproduced with permission from ref. 161; Copyright 2019 Elsevier. (d) The apparent line tension,  $\tau_a$ , versus the Young contact angle  $\theta_0$ . The curve shows an asymmetric U-shaped trend and a sign change at intermediate wettability, illustrating that the extracted  $\tau_a$  depends strongly on wetting state. The dashed line is the baseline prediction, while the red and blue curves show the small changes obtained when a Tolman correction and an assumed intrinsic line tension are included. Reproduced with permission from ref. 162. Copyright 2023 American Physical Society.



graphene, graphite, and hexagonal boron nitride surfaces. More recently, Surblys *et al.*<sup>163</sup> extended the dry-surface method to systems with long-range electrostatic interactions by incorporating damped Coulomb potentials. They acknowledged that when long-range Coulombic interactions are present at the interface, special treatment is required that is not typically implemented in generic molecular dynamics software. By replacing long-range Coulombic interactions with damped interactions, Surblys *et al.*<sup>163</sup> demonstrated that the  $W_{\text{ad}}$  can be accurately computed for polar interfaces such as water on silica and metal oxide surfaces, thereby broadening the applicability of thermodynamic integration methods to technologically relevant systems. Together, these developments from the cleaving-wall framework to the phantom-wall and dry-surface methods, established a robust computational framework for quantifying interfacial energetics on both flat and textured surfaces.

While both the droplet and film approaches aim to quantify solid–liquid affinity, they differ fundamentally in scope and practical implementation. The droplet method reproduces the geometry of macroscopic experiments and provides a direct and visually intuitive measure of the APCA while capturing transient wetting dynamics and spreading behavior. However, its quantitative accuracy is often limited by curvature and line-tension effects that become pronounced at the nanoscale. In contrast, the film or slab configuration eliminates these geometric artifacts by employing a planar interface under periodic boundary conditions, which allows the evaluation of absolute interfacial free energies that can be decomposed into enthalpic and entropic contributions. The trade-off lies in interpretability since droplet simulations connect naturally with experimental observables, whereas film-based calculations offer a more rigorous thermodynamic route to  $W_{\text{ad}}$  and  $\gamma_{\text{SL}}$  but lose direct information on dynamics. These two techniques are therefore best regarded as complementary because droplet models elucidate kinetic and morphological aspects of wetting, while planar films provide benchmark thermodynamic data for comparison with theoretical and continuum descriptions. Most of these studies considered chemically homogeneous and atomically smooth substrates to isolate fundamental wetting mechanisms, yet real surfaces often exhibit chemical heterogeneity, nanoscale roughness, and defects that profoundly affect both static and dynamic  $\theta$ . These effects and their treatment in molecular simulations are discussed in section 4.4.

The range of MD methodologies available for studying wettability provides a comprehensive framework for connecting microscopic interfacial phenomena with macroscopic observables. Droplet configurations capture the morphological and dynamic aspects of spreading, film geometries provide direct access to interfacial energetics, and free-energy-based approaches yield thermodynamic quantities that can be rigorously compared across materials and conditions. Despite their methodological differences, all these techniques ultimately rely on the accuracy and transferability of the underlying force fields used to describe solid–liquid interactions. Thus, the pre-

dictive capability of MD simulations depends critically on how well the employed interaction potentials reproduce dispersion, polarization, and cross-species effects at the interface. Taken together, these methodologies now form a mature simulation framework that enables both qualitative and quantitative investigation of wetting phenomena across a wide range of materials. Yet, their predictive power continues to evolve as advances in force-field design and interfacial thermodynamics improve the consistency between atomistic and continuum descriptions of wetting. Section 4.3 examines these aspects in detail, emphasizing the parameterization strategies, mixing rules, and cross-interaction models that govern the quantitative reliability of wettability predictions.

#### 4.2 Size effects, line tension, and curvature corrections

The quantitative interpretation of wetting behavior in molecular simulations is strongly influenced by finite-size effects and interfacial curvature, which alter the apparent thermodynamic quantities extracted from nanoscale droplets and films. One of the primary consequences of nanoscale modeling is the size dependence of the ACA. Because MD droplets typically range from 2 to 10 nm in radius, their pronounced curvature produces a significant Laplace pressure that modifies the internal structuring of the fluid and shifts the balance of interfacial tensions. Classical Young's law does not include this curvature dependence, and as a result, simulated contact angles tend to deviate systematically from macroscopic measurements. Numerous studies have shown that the ACA varies approximately linearly with the inverse droplet radius, allowing extrapolation toward the macroscopic limit through relations of the form  $\cos \theta$  versus  $1/r$ , where  $r$  is the contact-line radius, see Fig. 9(c). This linear scaling behavior has been demonstrated consistently for both spherical and cylindrical droplets.<sup>161,164–166</sup> These observations highlight the importance of size scaling and extensive ensemble averaging when interpreting contact angles from MD simulations, as the apparent wettability can otherwise be strongly biased by nanometric curvature effects.

Beyond the curvature-induced deviations captured through inverse-radius scaling, several additional factors complicate the interpretation of size-dependent contact angles in MD simulations. At very small radii, typically below 2–3 nm, the assumption of a smooth macroscopic interface breaks down due to molecular granularity, leading to nonlinear deviations from the expected  $\cos(\theta) - 1/r$  behavior and limiting the reliability of extrapolation procedures.<sup>167–169</sup> Moreover, the degree of size dependence varies substantially across different force fields and substrate–liquid interaction strengths, reflecting differences in liquid structuring, density oscillations, and layering at the solid–liquid interface.<sup>170,171</sup> The choice of droplet geometry also plays a significant role since cylindrical droplets often exhibit weaker size dependence than spherical droplets, given that cylindrical configurations eliminate curvature in one dimension, whereas spherical droplets suffer more pronounced Laplace-pressure variations and require larger simulation domains to converge.<sup>172,173</sup> Periodic boundary con-



ditions further modulate these effects by constraining capillary fluctuations of the liquid–vapor interface and introducing long-range interactions between droplet images. Taken together, these considerations highlight that finite-size effects in nanoscale droplets arise from a combination of geometric curvature, molecular structuring, and boundary artifacts, and that careful control of these variables is essential for extracting physically meaningful wettability descriptors from molecular simulations.

A second source of deviation from classical wetting behavior arises from line tension, the excess free energy associated with the three-phase contact line. While negligible for droplets larger than tens of micrometers, line tension can exert a measurable influence on nanoscopic droplets, effectively modifying the balance of interfacial forces and shifting the equilibrium  $\theta$ . MD simulations suggest that line tension may be either positive or negative depending on the intrinsic structure of the interface and the degree of liquid layering near the substrate.<sup>164,174,175</sup> A positive line tension tends to increase the  $\theta$  of small droplets, making the surface appear less wetting, whereas negative line tension has the opposite effect. In practical terms, line-tension contributions are incorporated into modified forms of Young's equation, where the ACA becomes explicitly dependent on droplet size. Extracting line tension from MD simulations often involves fitting the size-dependent  $\theta$  to these extended models or computing the free-energy change associated with incremental variations of the contact-line length. The sensitivity of these estimates to noise, sampling time, and droplet geometry highlights the need for rigorous statistical averaging.

In practice, the quantitative determination of line tension from MD simulations remains highly controversial. Reported values span several orders of magnitude, typically from  $10^{-12}$  to  $10^{-9}$  N, depending on the model system and analysis protocol, which raises questions about whether  $\tau$  can be regarded as a well-defined material parameter.<sup>66,176,177</sup> A major source of uncertainty stems from the ambiguity in defining the droplet size and contact radius in nanoscale systems, where thermal fluctuations, density oscillations, and deviations from a perfect spherical-cap shape blur the location of the three-phase contact line.<sup>172,178</sup> Different fitting strategies, such as using  $\theta$  versus  $1/r$ ,  $\cos\theta$  versus  $1/r$ , or free-energy-based constructions, can produce significantly different estimates of  $\tau$  for the same underlying trajectory, highlighting the sensitivity of line-tension extraction to the chosen geometric or thermodynamic definition.<sup>66,161,164–166,173</sup> Moreover, line tension is strongly influenced by microscopic details including liquid layering at the substrate, the range and shape of wall–fluid interaction potentials, and the amplitude of capillary waves along the interface.<sup>162,179,180</sup> This sensitivity is illustrated in Fig. 9(d) (adapted from ref. 162), where the apparent line tension extracted from nanoscale droplet fits varies non-monotonically with wettability and even changes sign with increasing contact angle. These sensitivities imply that  $\tau$  is not a universal constant of a given solid–liquid pair but rather an effective parameter that depends on droplet size, thermo-

dynamic state, surface chemistry, and the specific operational definition employed in the analysis.

Overall, the influence of finite-size effects and line tension on nanoscale droplets highlights that ACAs derived from MD simulations are effective, scale-dependent quantities shaped by curvature, molecular layering, capillary fluctuations, and definition-dependent geometric choices. These factors complicate direct comparison with macroscopic measurements and require explicit treatment through careful size scaling, consistent operational definitions, and rigorous statistical sampling. Rather than small perturbations, these contributions can substantially alter the apparent wettability at nanometric dimensions, underscoring the need for methodological consistency and clear thermodynamic interpretation when extracting interfacial properties from simulation data. These considerations also interact strongly with other sources of deviation from continuum wetting descriptions, including system anisotropy, substrate heterogeneity, and the coupling between interfacial structure and dynamic relaxation, which are addressed in the following subsections.

### 4.3 Force fields and cross-species interaction potentials

The accuracy of the simulation methods described in section 4.1 largely depends on the accuracy of the underlying interatomic potentials representing the solid–liquid interface. Accurate prediction of wettability for a particular interface is very sensitive to the selection of the water model, the intramolecular potential for the solid phase, and the cross-species solid–liquid interaction potential.<sup>40,61</sup> Studies demonstrated that the same interface can be predicted as hydrophobic, partial wetting, or even hydrophilic based on the selection of these interaction potentials, making appropriate force-field selection crucially important for MD simulations on wettability.<sup>39,40,181</sup>

**4.3.1 Simple Lennard-Jones models.** Early wettability MD studies used simplified systems where both the liquid and solid atoms were considered as identical and interacting only through the LJ potential.<sup>182</sup> Although these hypothetical monoatomic LJ fluids do not represent any real substance, they remove many properties associated with real molecules, such as complex geometry, electric charges, and hydrogen bonding. Several early studies confirmed that Young's equation, which relates the  $\theta$  to interfacial free energies, does hold for nanoscale droplets of LJ fluids on LJ solid walls.<sup>40,182–184</sup> Surblys *et al.*<sup>182</sup> summarized these findings and demonstrated that systematically varying the solid–liquid LJ well depth results in a change in the contact angle in a predictable manner following Young's equation. It has been observed that increasing solid–liquid attraction causes the  $\theta$  to decrease. By observing this linear relationship between the LJ energy parameter and wetting behavior, researchers concluded that the fundamental physics of wetting can be predicted by these simple models even for microscopic droplets. These studies also established a foundation for more complex studies involving realistic molecular liquids.

Building on these foundations, researchers tried to obtain a direct connection between the microscopic interaction para-



meter and the macroscopic thermodynamic quantity. Using the phantom-wall thermodynamic integration method, Leroy and Müller-Plathe<sup>159</sup> demonstrated that for LJ liquids on LJ solids,  $W_{\text{ad}}$  varies linearly with the solid–liquid LJ energy parameter over a wide range of values. More recently, researchers have moved from simple LJ fluids to studying real water on solid surfaces. However, they face additional complexity since water molecules have unique properties that simple LJ atoms cannot capture, *e.g.*, water has a specific bent geometry, carries partial electric charges, forms hydrogen bonds with neighbors, and exhibits bulk properties like surface tension and density. For addressing these criteria, researchers developed sophisticated water models, such as SPC/E (Extended Simple Point Charge)<sup>185</sup> and TIP4P (Transferable Intermolecular Potential with 4 interaction sites),<sup>186</sup> describing intermolecular water interactions. These models are designed to include partial charges and specific bond geometries, and to reproduce experimental properties of liquid water. Nonetheless, while using these sophisticated water models, researchers typically describe the water and non-polar surfaces (such as graphite or carbon nanotubes) interaction using a simple LJ potential between specific atom pairs (*e.g.*, C–O pairs). This method maintains the water model's accuracy for water–water interactions while leveraging the tunable LJ potential for the solid–water interaction for predicting wetting behavior.<sup>40,182,183</sup>

**4.3.2 Classical and DFT-informed water models and non-polar surfaces.** One of the most extensively studied cases of wettability using MD simulations is water on graphitic and related nonpolar carbon surfaces. Researchers typically use explicit water models such as SPC/E and describe the water–carbon interaction with a LJ potential between water oxygen atoms and solid carbon atoms.<sup>39,40</sup> The landmark study by Werder *et al.*<sup>39</sup> established the foundation for calibrating water–carbon interaction parameters. In their investigation, the authors placed water droplets on graphite surfaces, implementing the SPC/E water model while the graphite surface was modeled as discrete carbon atoms. The solid–liquid interactions were modeled through a simple C–O LJ potential with a fixed distance parameter  $\sigma_{\text{CO}} = 3.19 \text{ \AA}$  and varying energy well depth  $\epsilon_{\text{CO}}$ . For each  $\epsilon_{\text{CO}}$  value, they computed both the equilibrium  $\theta$  and the binding energy of a single water molecule adsorbed on the graphite surface. The authors observed that a stronger water–surface attraction (increased well depth) leads to a more negative binding energy and a smaller  $\theta$ . This linear relationship provided a practical calibration strategy, given that if the experimental  $\theta$  of water on a surface is known, we can determine the appropriate  $\epsilon_{\text{CO}}$  value for the simulation to reproduce this experimental result. Werder *et al.*<sup>39</sup> suggested several quantitative benchmarks that later became reference points for the field. In addition, the authors reported a critical binding energy value (approximately  $-12.82 \text{ kJ mol}^{-1}$ ) below which water completely wets the graphite surface. Lastly, the optimum  $\epsilon_{\text{CO}}$  value ( $0.392 \text{ kJ mol}^{-1}$ ) was calibrated to reproduce the experimental  $\theta$  of approximately  $86^\circ$ ,<sup>187</sup> and predicted a binding energy of about  $-6.33 \text{ kJ mol}^{-1}$  for water droplets having 2000 molecules.

Later, Jaffe *et al.*<sup>40</sup> corroborated this procedure to calibrate water–carbon LJ parameters from  $\theta$  data rather than relying on adsorption energies from quantum calculations. The authors comprehensively surveyed water–carbon interaction potentials from the literature and found dramatic inconsistencies in wettability prediction. It was found that different studies calibrated their parameters based on different experimental values, and some parameter sets predicted complete wetting of graphite, while others predicted contact angles ranging from about  $40^\circ$  to over  $100^\circ$ . Further observations indicated that some researchers included C–H LJ interactions along with the C–O terms, while others did not, and this choice affects the predicted  $\theta$ . The effect of the long-range cutoff distance was also investigated, and it was found that this interaction cutoff modifies the effective interaction strength and the  $\theta$ . An important takeaway from these studies is that for water–graphite systems, researchers should calibrate the solid–liquid interaction potential properly against experimental measurements, rather than relying on standard Lorentz–Berthelot mixing rules that are used to estimate LJ parameters between unlike atoms by taking arithmetic and geometric means of the pure-components.<sup>40</sup> In conclusion, Werder's and Jaffe's results demonstrate that even after using the same SPC/E water model and identical non-polar carbon surface, predicted wettability can range from complete wetting to a  $\theta$  over  $100^\circ$  (just as observed in experimental setups) depending on the chosen water–carbon LJ parameters and surface representation.

Recently, researchers have developed DFT-informed classical potentials with a view to combining the accuracy of QM calculations and the computational efficiency of classical MD simulations. In one notable study, researchers utilized a graphene–water potential developed by using an adaptive force matching (AFM) method.<sup>188</sup> They fit the graphene–water interaction parameters to reproduce forces obtained from DFT calculations (at PAW-PBE-D3 level) while keeping the water model (BLYPSP-4F) and the graphene potential (PPBE-G) unchanged. The ultimate potential function provided a computationally inexpensive approximation of the DFT calculation that includes many-body polarization effects. The study further revealed that when they expressed the graphene–water interaction in a Buckingham form (different than 12-6 LJ), they obtained a lower root-mean-square error between fitted and DFT forces compared to a standard LJ cross interaction.

Using this DFT-trained potential, they obtained a macroscopic water–graphene contact angle of about  $86^\circ$ , which showed very good agreement with an experimental value of  $85^\circ \pm 5^\circ$  on suspended graphene.<sup>189</sup> This DFT-informed approach shows a promising path for developing water–surface potentials that can retain QM accuracy while remaining computationally inexpensive.

**4.3.3 Force fields for wettability on 2-D materials, oxides, and metals.** For more complex solids than graphite, researchers still rely on the same basic force field ingredients. Many studies use Lennard-Jones and Coulomb interactions, and the difference arises from the choice of force field ingredients and their combination. Some studies treat  $\text{MoS}_2$  sheet as non-reactive.



tive and keep the water model standard, then tune the MoS<sub>2</sub> parameters. One such study modeled water using SPC/E, while the atoms in MoS<sub>2</sub> carried partial charges and interacted with water through a standard 12-6 LJ and Coulomb parameters. The water–solid LJ cross terms were generated using a geometric-mean mixing rule.<sup>181</sup> The partial charges on Mo and S atoms were derived using the DFT-based charge derivation approach (DDAP). Then the LJ parameters for Mo and S were fitted using lattice dynamics to reproduce the bulk MoS<sub>2</sub> lattice and elastic properties. Hence, the charges were derived from the electronic structure, while the LJ parameters were tuned to match the mechanical structure. The authors validated this force field by comparing the force field-predicted interlayer interaction energy between two MoS<sub>2</sub> nanosheets to values obtained from dispersion-corrected DFT. An additional key finding of this study was obtained by comparing simulations performed with and without partial charges. This comparison showed that MoS<sub>2</sub>–liquid interactions are overwhelmingly governed by dispersion forces, with electrostatic contributions accounting for less than 1% of the total interaction energy.

On the other hand, for oxides and glass surfaces, electrostatics and hydrogen bonding are significantly more important. Consequently, force fields for these surfaces typically assign fixed charges to the solid atoms and combine that with a water model. Thus, wettability predictions largely depend on charge values, surface chemistry, and long-range electrostatics. In one glass wettability study, the substrate was modeled as amorphous SiO<sub>2</sub>, and the surface region was allowed to move while interacting with water. The COMPASS force field was used for both the glass and the water.<sup>190</sup> The authors compared untreated glass with surfaces modified by plasma treatment and observed that surface functionalization changed wettability significantly. Hydroxylated surfaces were found to have a stronger interaction with the water droplet and showed significant improvements in wetting. A study performed by Surblys *et al.*<sup>182</sup> shows a more mechanistic point. The authors studied water on a crystalline silica surface ( $\alpha$ -cristobalite (101)) without silanol groups. The water molecules were modelled through the flexible SPC/Fw model, and silica parameters were obtained from Emami *et al.*,<sup>191</sup> while the cross-interaction parameters were obtained from Lorentz–Berthelot mixing rules.<sup>182</sup> The authors found that increasing either LJ or Coulombic strength results in an increased value of  $W_{\text{ad}}$ . In addition, it was noted that the system having both LJ and Coulombic interactions can provide a lower  $W_{\text{ad}}$  than an LJ-only system having the same total solid–liquid interfacial energy, which was attributed to the entropic contribution. Electrostatic interactions created a broader range of local interfacial energies, which could increase entropy contributions that reduced the  $W_{\text{ad}}$ . These examples demonstrate that for oxides and glass surfaces, along with the water models, researchers should specify what charge model is used, what functional groups are present, and how electrostatic interactions are computed, as all of these affect the predicted contact angle and  $W_{\text{ad}}$ .

For metal–water interfaces, many classical MD studies used three parts: a many-body potential for the metal, a rigid water model, and an empirical metal–oxygen interaction. For a gold–water interface, Paniagua-Guerra and Ramos-Alvarado<sup>41</sup> used an embedded atom method (EAM)<sup>192</sup> potential for Au–Au interactions and SPC/E for water, while the Au–water interactions were defined through several parameter sets from the literature. The authors tested nine different Au–water interaction parameter sets from the literature, including different functional forms, such as LJ 12-6, LJ 9-6, Buckingham, Morse, and Morse + Born–Mayer–Huggins.<sup>41</sup> Each of these parameter sets was originally derived by fitting to different target properties, including experimental  $\theta$ , experimental adsorption energy, experimental surface tension, and DFT-derived binding energies. All these force fields predicted almost complete wetting on gold, so that a macroscopic  $\theta$  could not be resolved within the simulation; thus, the authors used interfacial interaction energy as a practical metric instead of  $\theta$ .<sup>41</sup> Even though the  $\theta$  was essentially zero for all Au–water force field options, the computed thermal boundary conductance varied significantly. In fact, it varied by a factor of four to five, ranging from 98 to 472 MW (m<sup>2</sup> K)<sup>−1</sup>. This variation highlights that even if different metal–water potentials predict similar wetting behavior, they can produce substantially different interfacial transport properties. The authors also argued that the changes in thermal boundary conductance could not be fully explained by the interaction energy alone. The authors found that the density depletion length provided better characterization of thermal boundary conductance and observed an exponential relationship between the thermal boundary conductance and the depletion length. Overall, metal–water wettability simulations are highly sensitive to the exact parameterization of the metal–water potential. Hence, while discussing the wettability of metals, researchers should clarify the metal potential, the water model, and the full metal–water interaction model used.

**4.3.4 Force-field sensitivity and non-uniqueness of wettability.** Examples in earlier subsections indicate that MD wettability calculations do not solely depend on the chosen system setup (droplets *vs.* films, dry-surface *vs.* phantom-wall), but also depend strongly on the chosen interatomic potentials.<sup>193</sup> For graphite–water and carbon nanotube–water systems, the MD studies by Werder *et al.*<sup>39</sup> and the follow-up work by Jaffe *et al.*<sup>40</sup> demonstrated that changing the water–carbon LJ parameters can strongly shift the wetting behavior, *e.g.*, some parameter sets predicted the surface to be strongly hydrophobic, while others predicted full wetting. Their findings explained this sensitivity in terms of how strongly the chosen potential binds a single water molecule to graphene or graphite. Werder *et al.* suggested a critical binding energy of water–graphite (about 12.8 kJ mol<sup>−1</sup> for their setup) below which the model predicts complete wetting. Jaffe *et al.* found that high-level QM predicts a much stronger water–graphene binding energy (around 24 kJ mol<sup>−1</sup>), and so, a potential calibrated to match that binding energy will predict complete wetting, although some experiments report a finite  $\theta$  of around 84–86°.<sup>40,187,194</sup>



MoS<sub>2</sub>-wettability is another example of force-field parameter sensitivity; Leroy<sup>184</sup> showed that the direct combination of existing force-field parameters can lead to opposite wetting characteristics, from complete wetting to hydrophobic behavior. In addition, it was shown that if the surface tension of the chosen water model is not considered, then droplet-based force field fitting for MoS<sub>2</sub> can be misleading. That is, if the water model has a surface tension different from the experimental value, and such a model is used to parametrize the force field to reproduce a target  $\theta$  or adhesion behavior, then the fitting procedure can push the substrate-water LJ parameters to unrealistic values.<sup>195</sup> Similarly, Govind Rajan *et al.*<sup>181</sup> found that dispersion interactions dominate the interfacial behavior on the MoS<sub>2</sub> basal plane and electrostatic interactions play a negligible role.

For metal–water systems, particularly Au–water interfaces, the choice of interatomic potential significantly affects wettability prediction. Classical MD studies using various LJ and Morse-type force fields predict strong hydrophilicity with complete wetting for Au surfaces. These force fields were parameterized from Lorentz–Berthelot mixing rules, experimental  $\theta$ , experimental adsorption energies, or DFT-derived binding curves.<sup>41</sup> However, although all of them show complete wetting, these models can give very different interaction energies and density depletion lengths near the surface, indicating that microscopic structure and energetics can differ significantly even when the droplet shape looks similar. In stark contrast, *ab initio* MD simulation has predicted Au(111) to be weakly hydrophobic, with a  $\theta$  around 95°,<sup>82</sup> which is fundamentally different from other classical MD results for Au. This gap suggests that common classical pairwise metal–water potentials may be missing important physics. The missing information could be related to electronic response at the interface and entropy-related effects that are present in *ab initio* simulations but are absent in simple empirical pair potentials.

Surblys *et al.*<sup>182</sup> pointed out an important non-uniqueness for silica–water interfaces. The authors reported that two interfaces can have almost the same average solid–liquid interaction energy but still depict different values of  $W_{\text{ad}}$ . If the interface is modeled primarily using LJ interactions, a higher work of adhesion  $W_{\text{ad}}$  is obtained for a given average interaction energy. However, when solid–liquid Coulomb interactions are included while maintaining the same average total solid–liquid energy,  $W_{\text{ad}}$  can decrease by approximately 25 mN m<sup>-1</sup>. All these examples explain a common problem in the wettability literature, namely, the same interface has been reported to have different values of  $\theta$ , depletion lengths, slip lengths, and  $W_{\text{ad}}$ .<sup>60,61,193</sup> Many times, this discrepancy is not due to a methodological error by a particular research group, but rather to the use of different force fields calibrated against different target properties. Because wettability is not uniquely determined by a single fitting parameter, several studies recommend that future interfacial force fields be validated against a broader set of observables, rather than relying on a single  $\theta$  alone.<sup>41,60,61,82,182,193</sup> Examples of such validation

targets include adsorption energies, interfacial density profiles, hydrogen-bond statistics, interfacial free energies, and, when possible, transport-related quantities such as slip length or thermal boundary conductance.<sup>196</sup>

**4.3.5 Systematic force-field verification, optimization, and emerging potentials.** The force-field sensitivity documented in sections 4.3.1–4.3.4 highlights the need for systematic verification and optimization strategies. Rather than calibrating interfacial force fields against a single target property, a multi-property validation protocol should be adopted that simultaneously benchmarks against contact angles or work of adhesion, single-molecule adsorption energies from high-level quantum mechanical calculations, interfacial density profiles, hydrogen-bond statistics in the first hydration layer, and at least one transport quantity such as thermal boundary conductance or slip length.<sup>41,60,61</sup> Heinz *et al.*<sup>197</sup> proposed such a philosophy for the INTERFACE force field, emphasizing simultaneous reproduction of surface energies, lattice parameters, and densities with considerable accuracy. Beyond validation, the parameterization process itself benefits from multi-objective optimization frameworks that identify Pareto-optimal parameter sets balancing multiple target properties simultaneously. Jaramillo-Botero *et al.*<sup>198</sup> developed GARFField, a genetic algorithm-based multi-objective optimizer for reactive force fields, while Verstraelen *et al.*<sup>199</sup> introduced a balanced loss function for ReaxFF parameterization that replaces manual weight assignment with category-specific tolerances for water adsorption on alumina. Bayesian optimization approaches further complement these methods by providing uncertainty estimates on fitted parameters and guiding efficient exploration of high-dimensional parameter spaces.<sup>200</sup> Applying such frameworks to wettability-specific parameterization, where contact angles, adhesion energies, and interfacial structure are optimized simultaneously, remains a largely unexplored but promising direction.

Emerging potential energy descriptions offer additional pathways to mitigate force-field limitations. Machine learning interatomic potentials (MLIPs) learn the potential energy surface directly from *ab initio* reference data through flexible representations such as neural networks or equivariant message-passing architectures, capturing many-body effects and polarization without imposing fixed functional forms.<sup>201</sup> Recent applications to solid–liquid interfaces demonstrate that MLIPs can reproduce AIMD-quality interfacial structures at a fraction of the computational cost. For instance, high-dimensional neural network potentials and DeePMD have been applied to oxide–water interfaces, including magnetite, mica, and calcium-silicate-hydrate systems, enabling nanosecond-scale simulations with near-DFT accuracy.<sup>202,203</sup> However, challenges remain in treating long-range electrostatic and dispersion interactions critical for wettability, and universal MLIPs trained predominantly on bulk data require further benchmarking at interfaces.<sup>204,205</sup> Reactive force fields such as ReaxFF<sup>206</sup> complement these approaches by enabling bond formation and breaking through a bond-order formalism, which is essential for surfaces where dissociative water adsorp-



tion, proton transfer, or hydroxylation govern the wetting state.<sup>207</sup> ReaxFF has been applied to water interactions with calcium oxide,<sup>208</sup> alumina,<sup>199</sup> and silicate glasses,<sup>209</sup> capturing reactive wetting events inaccessible to non-reactive potentials. While neither MLIPs nor reactive force fields have yet been systematically deployed for contact angle calculations in the manner of classical non-reactive potentials, their ability to capture electronic-level accuracy and interfacial reactivity positions them as key tools for next-generation wettability simulations.

#### 4.4 Interfacial structure: density profiles and hydrogen bonding

A detailed understanding of wettability at the nanoscale requires examining how liquid molecules reorganize in response to the chemical and physical nature of a solid surface. Surface composition, polarity, functional groups, and atomic topology strongly modulate the local arrangement of interfacial molecules, yet macroscopic descriptors such as the contact angle cannot reveal these underlying structural mechanisms. Thus, MD simulations uniquely resolve these microscopic features, liquid layering transitions, orientational ordering, and hydrogen-bond restructuring that are inaccessible through conventional experimental techniques. These interfacial signatures directly influence the solid–liquid interfacial free energy, the  $W_{\text{ad}}$ , and the hydrophobic or hydrophilic character of a surface. The associated structural modifications alter the energetic cost of displacing interfacial molecules and therefore serve as the microscopic origin of macroscopic wetting behavior, linking molecular organization to adhesion and contact-angle trends. Because the microscopic structure of interfacial liquids responds sensitively to chemical termination, surface polarity, defect sites, and the choice of interaction potential, characterizing these structural arrangements provides a mechanistic foundation for understanding and predicting wetting behavior across diverse material systems.

The density profile, perpendicular to the solid surface is one of the most fundamental structural descriptors for characterizing a solid–liquid interface in MD simulations, as it directly quantifies how the local number density of water reorganizes in response to the chemical and topographical features of the substrate. Studies of graphitic materials consistently report pronounced oscillatory layering within the first few molecular layers, arising from excluded-volume effects and the corrugation of the underlying carbon lattice.<sup>60</sup> This behavior has been demonstrated in detailed interfacial analyses of graphite–water systems, where the first-layer adsorption peak and the subsequent decay length correlate with the interfacial free energy and wettability.<sup>60,85,210</sup> Comparable trends are observed for transition-metal dichalcogenides such as MoS<sub>2</sub>, where density layering and decay constants track variations in hydrophobicity and are strongly coupled to interfacial thermal resistance.<sup>211</sup> In contrast, polar and partially ionic ceramics such as 3C-SiC or Al<sub>2</sub>O<sub>3</sub> exhibit stronger layering amplitudes, shorter structural relaxation lengths, and more prominent first-layer adsorption, reflecting their higher surface polarity and stronger water–solid interactions.<sup>87,212</sup> Fig. 10(a) illustrates

interfacial density profiles for 3C-SiC surfaces, where Si-terminated planes exhibit significantly higher first-layer adsorption peaks ( $\sim 3.5 \text{ g cm}^{-3}$ ) and deeper penetration of liquid structuring into the bulk compared to C-terminated surfaces.<sup>87</sup> These system-specific observations collectively support the broader trend that enhanced layering and rapid structural decay correlate with higher solid–liquid adhesion and reduced contact angle. Taken together, graphitic, MoS<sub>2</sub>, SiC, and alumina systems illustrate a continuum in which increasing surface polarity and electronic heterogeneity strengthen first-layer adsorption, amplify structural ordering, and reduce the equilibrium contact angle. Thus, density profiles serve as a primary microscopic observable that connects interfacial molecular organization with emergent wetting behavior.

Beyond the oscillatory density layering observed at most solid–liquid interfaces, the specific structural response of water depends strongly on the chemical identity, charge distribution, and lattice geometry of the substrate. On covalent substrates such as 3C-SiC, the interfacial water structure is strongly influenced by the atomic arrangement and termination of the surface. Simulations show that water molecules tend to adopt positional patterns that mirror the underlying distribution of Si and C atoms, forming density maxima above specific surface sites determined by the lattice geometry.<sup>212</sup> The degree of water adsorption depends on the surface termination: more hydrophilic terminations promote stronger alignment of water molecules with the substrate, producing higher-density regions within the first hydration layer, whereas hydrophobic terminations yield weaker layering and reduced occupation of interfacial sites. These high-density interfacial regions exhibit vibrational characteristics reminiscent of solid-like, ice-like structures, reflecting constrained molecular motion and reduced diffusivity relative to the bulk. Such structural signatures highlight the strong coupling between local surface chemistry and the molecular organization of interfacial water on SiC. Alumina–water interfaces represent another case where the solid's electronic structure imposes pronounced ordering on the adjacent liquid. Partial ionic character and strong electrostatic interactions anchor water molecules within the first few hydration layers, leading to tightly bound interfacial water, restricted reorientation, and well-defined hydrogen-bond networks.<sup>87</sup> These features produce large layering amplitudes and significantly lower mobility compared to non-polar surfaces. Weakly interacting substrates such as graphite present an opposite limit: interfacial layering arises primarily from excluded-volume effects and the corrugated sp<sup>2</sup> lattice, with reduced hydrogen-bond coordination and preferred in-plane dipole orientations that correspond to low adhesion and high interfacial slip.<sup>60,85</sup> Comparisons among SiC, alumina, and graphite highlight how interfacial density, hydrogen bonding, and orientational ordering are dictated by the local electronic structure and surface chemistry of the solid.

Hydrogen bonding and molecular orientation provide a complementary perspective on interfacial structure, since variations in hydrogen-bond topology are expected to have a further effect on wettability than density alone. At hydrophobic





**Fig. 10** (a) Interfacial water density profiles perpendicular to 3C-SiC surfaces with different crystallographic planes and atomic terminations. Si-terminated surfaces exhibit higher first-layer adsorption peaks and more extended liquid layering compared to C-terminated surfaces, reflecting stronger solid–liquid interactions and enhanced hydrophilicity. Reproduced with permission from ref. 87. Copyright 2018 American Chemical Society. (b) Molecular dynamics snapshots of interfacial water at an amorphous alumina–water interface. Atoms are colored by instantaneous heat transfer rate (red: low, white: medium, blue: high). Tracked water molecules in deep potential wells (orange) remain spatially confined with restricted mobility, while those in weaker interaction regions (green) retain greater translational and rotational freedom. Adapted with permission from ref. 87. Copyright 2021 American Chemical Society. (c) Temperature dependence of the work of adhesion  $W_{\text{ad}}$  for water near a Lennard-Jones 9-3 wall at varying substrate strengths. Curves from bottom to top correspond to surface strengths of  $\epsilon_{\text{sf}} = 0.831, 1.66, 2.49, 3.33, 4.16, 4.99,$  and  $5.82 \text{ kJ mol}^{-1}$ . Adapted with permission from ref. 213. Copyright 2013 American Chemical Society. (d) Number of hydrogen-bond donors (HBDs) per water molecule in the adlayer region as a function of surface hydrophilicity, quantified by the work of adhesion ( $W_{\text{ad}}$ ). Data span hydrophobic carbon surfaces (fluorographene, graphene, graphite) to hydrophilic metal surfaces (Ag, Au, Pt, Pd) with (100) and (111) facets. The horizontal dashed line indicates the bulk water value of 1.70. The strong linear correlation ( $R^2 = 0.92$ ) demonstrates that hydrogen-bond network connectivity serves as a molecular-level descriptor of macroscopic wettability. Reproduced from ref. 63, under the terms of the Creative Commons Attribution 4.0 License (CC BY 4.0). Changes: none.

surfaces such as graphite, the hydrogen-bond network remains close to bulk-like in the second and third layers, but water molecules in direct contact with the solid tend to orient one OH group toward the vapor phase, generating a population of undercoordinated “dangling” OH bonds and reduced hydrogen-bond saturation at the interface.<sup>211,214</sup> On weakly interacting surfaces, density layering and orientational ordering often play a more decisive role in determining interfacial structure than hydrogen-bond rearrangements, which remain relatively bulk-like and only modestly perturbed by the substrate. This

broken coordination pattern is consistent with the weaker solid–liquid adhesion and enhanced slippage reported for graphitic substrates, where interfacial water exhibits preferential in-plane dipole orientation and diminished hydrogen-bond connectivity within the first layer.<sup>60,85,214</sup> On hydrophilic and partially ionic surfaces, hydrogen bonding reorganizes much more strongly. At alumina–water interfaces, for example, partial charges on surface Al and O atoms stabilize a dense network of surface-anchored hydrogen bonds, producing tightly bound hydration layers with restricted rotational



freedom, enhanced tetrahedral order, and solid-like vibrational signatures within the first two to three molecular layers.<sup>87</sup> This stabilization is captured in Fig. 10(b), depicting the interfacial atomic trajectories for an amorphous alumina surface. In this snapshot, the color-coded spheres reveal the instantaneous interatomic heat transfer rates, while tracked water molecules (highlighted in orange) are shown trapped in large attractive potential wells caused by the outermost solid atoms. These molecules maintain fixed positions and orientations throughout the observation period, which illustrates the strong mobility constraints and the absorption mechanism that facilitates vibrational energy transmission parallel to the substrate. Si-terminated 3C-SiC surfaces exhibit a different but equally pronounced structural response. Simulations show higher density peaks in the first hydration layer and strongly confined interfacial regions with ice-like characteristics, indicating that water molecules adopt highly ordered configurations that closely follow the underlying lattice.<sup>212,215,216</sup> Although explicit hydrogen-bond statistics were not reported in this study, the combination of large first-layer densities and solid-like vibrational behavior suggests the presence of a strongly coordinated hydrogen-bond network within these interfacial regions. Across these systems, quantitative metrics such as hydrogen-bond coordination numbers, donor-acceptor lifetimes, angular distributions, and tetrahedral order parameters consistently correlate with calculated adhesion energies, interfacial thermal conductance, and macroscopic contact angles, underscoring the central role of hydrogen-bond networks and orientation in determining wetting behavior.<sup>85,214,217</sup>

The structural signatures discussed above, density oscillations, orientational ordering, and the degree of hydrogen-bond stabilization or disruption, have direct consequences for macroscopic wettability and interfacial energetics. Systems that promote tightly bound, strongly coordinated hydration layers, such as alumina-water interfaces, exhibit large adhesion energies and low interfacial thermal resistance, consistent with enhanced solid-liquid affinity.<sup>87</sup> In contrast, surfaces that generate weak or diffuse first-layer structuring, as reported for graphitic substrates, typically display lower  $\gamma_{SL}$  values, reduced vibrational coupling, and higher thermal boundary resistance.<sup>60,85</sup> The SiC studies demonstrate an intermediate behavior: the formation of dense, ice-like hydration layers on Si-terminated surfaces correlates with stronger adhesion and reduced interfacial resistance compared to C-terminated surfaces, where weaker structuring accompanies reduced wettability.<sup>212</sup> Across these materials, MD evidence consistently shows that the characteristics of the first one or two hydration layers are strongly predictive of both macroscopic contact angles and thermal transport properties, underscoring the central role of interfacial liquid structure in governing the strength and functionality of solid-liquid interactions. Collectively, these findings emphasize that wettability does not arise from a single microscopic descriptor but instead emerges from the coupled interplay among density structuring, molecular orientation, hydrogen-bond coordination, and interfacial

dynamics, all of which define the energetic landscape at the solid-liquid boundary.

#### 4.5 Entropy, diffusion, and dynamic properties

MD simulations show that the wetting behavior of a solid surface is closely related to entropy, diffusion, and other dynamic properties. As discussed earlier, Surblys *et al.*<sup>182</sup> showed that two interfaces can have almost the same average solid-liquid interaction energy but still have different  $W_{ad}$  due to entropic contributions. The authors showed that adding electrostatic interactions may broaden the distribution of interfacial energies that can increase the solid-liquid entropy and change the  $W_{ad}$  even when the average interfacial energy is similar. This suggests that  $\theta$  and wetting cannot be explained by interaction energy alone.

Temperature dependence is another simple way to probe the effects of entropy. Kumar and Errington<sup>213</sup> studied water near nonpolar flat surfaces using an interface-potential approach and found that the  $W_{ad}$  changes almost linearly with temperature. Fig. 10(c) illustrates the variation of  $W_{ad}$  with temperature  $T$  for a range of surface-liquid interaction strengths ( $\epsilon_{sf}$ ). The slope of each curve directly yields the entropy of adhesion, while the intercept provides the enthalpic contribution, with stronger substrates exhibiting steeper slopes indicative of greater entropic penalties upon wetting. This entropic penalty is not negligible. By evaluating the temperature dependence of contact angles across a range of solid-liquid-vapor systems, Weber and Stanjek<sup>218</sup> discussed that the excess entropy of adhesion falls within a consistent, narrow range (0.1 to 0.2 mJ m<sup>-2</sup> K<sup>-1</sup>). Notably, their quantification showed that at room temperature (25 °C), entropic contributions make up 30% to 50% of the total work of adhesion.<sup>219,220</sup> This contribution invalidates classical approaches that treat surface tension components as purely mechanical or energetic constants, proving the temperature dependence of wettability. Furthermore, MD simulations by Orselly *et al.*<sup>221</sup> demonstrated that if  $\gamma_{SV}$  is estimated using only the cohesive energy difference (neglecting entropy), the model predicts that surface tension increases with temperature. However, when the entropic contribution, which was estimated to be  $\sim 171$  mJ m<sup>-2</sup> at 450 K, was properly integrated into the free energy calculations, the surface tension showed a physically accurate decrease with temperature.

In short, if wetting behavior changes with temperature, then entropy plays a significant role, since entropy is related to the temperature-dependent part of free energy. Govind Rajan *et al.*<sup>181</sup> reported a similar observation for MoS<sub>2</sub>, indicating that the surface tension of SPC/E water decreases noticeably over the temperature range of 280–350 K, while the changes in water  $\theta$  on MoS<sub>2</sub> were very small (less than 3°). The authors attributed this result to the compensating effects of entropy on wettability. An analysis of the temperature dependence allowed them to separate enthalpic and entropic contributions, revealing a significant entropic component that counterbalances temperature-induced changes in interaction energies and maintains an approximately constant contact angle across the studied temperature range.



Wetting is also connected to diffusion and molecular mobility near the surface; thus, using a first-principles-based multi-scale method (DFT-CES), Gim *et al.*<sup>63</sup> studied water on clean metal surfaces. The authors evaluated wettability using the  $W_{\text{ad}}$ , and found that clean Ag, Au, Pd, and Pt surfaces are strongly wetting, producing 0° contact angles. The wetting strength was then related to the microscopic structure and dynamics of interfacial water. Water molecules adjacent to the metal surface were found to organize into well-defined adsorption layers. An analysis of hydrogen bonding within the first water layer revealed systematic shifts in the donor structure as surface hydrophilicity increased, as quantified by the work of adhesion. Notably, the number of hydrogen-bond donors (HBD) per water molecule in the adlayer increases linearly with  $W_{\text{ad}}$  (Fig. 10(d)), rising from values below bulk water at hydrophobic surfaces such as fluorographene and graphene to values approaching the ice-like limit of 2 at strongly hydrophilic metal surfaces.<sup>63</sup> These findings indicate that the hydrogen-bond pattern of the adlayer can serve as a molecular-level indicator of hydrophilicity. Furthermore, mean-squared displacement analyses showed that interfacial water exhibits reduced mobility compared to bulk water. Both translational and rotational diffusion coefficients decrease with increasing work of adhesion, demonstrating that stronger wetting is associated with increasingly hindered interfacial dynamics.

## 5. First principles and *ab initio* studies

### 5.1 DFT-based modeling of solid–liquid interfaces

Predicting surface wettability depends on the ability to describe intermolecular interactions at the electronic scale, where charge redistribution, polarization, and chemical bonding govern the affinity between a liquid and a solid. These effects lie beyond the reach of classical force fields and empirical surface-energy models. *Ab initio* simulations, particularly those based on Density Functional Theory (DFT), provide a rigorous quantum-mechanical framework to probe these interactions with chemical accuracy. First-principles analyses capture the formation and breaking of interfacial bonds, electron-density rearrangements, and subtle polarization effects that emerge when a fluid molecule approaches or adsorbs on a solid surface. Such capabilities make DFT key for elucidating the mechanisms governing hydrophilicity, hydrophobicity, and surface-specific reactivity. This section reviews recent progress in DFT-based wettability studies, emphasizing how descriptors such as adsorption energies, charge-density differences, interfacial dipoles, and work-function modifications relate to macroscopic  $\theta$ . These insights not only bridge electronic-structure effects with continuum theories of wetting but also guide the rational design of functional surfaces for catalysis, coatings, energy conversion, and liquid–solid interfacial engineering.

**5.1.1 DFT-based models: exchange–correlation functionals and dispersion corrections.** DFT provides a theoretical framework for studying interfacial physics and offers a predictive

approach for describing the electronic structure<sup>222,223</sup> and surface free energy ( $\gamma$ )<sup>224</sup> of the solid–liquid interfaces. However, the accuracy of DFT-based descriptions is dependent on the parameters such as exchange–correlation (XC) functional, representation of the solvent (explicit and implicit), and the boundary conditions (slab models and electrified interfaces). For the structural accuracy of surface wetting, the choice of the XC functional is critical. The simplest XC energy description for solids can be provided by the local density approximation (LDA) functionals; however, LDA overapproximates the energy by 1 eV per bond.<sup>225</sup> To overcome this issue, Generalized Gradient Approximation (GGA) functionals were introduced. In previous studies, GGA functionals, such as the Perdew–Burke–Ernzerhof (PBE),<sup>226</sup> Becke–Lee–Yang–Parr (BLYP)<sup>227,228</sup> and revised-PBE (RPBE),<sup>229</sup> have been used to model solid (*e.g.*, transition metals, Pd, or Pt) and liquid (water) interfaces.<sup>223,230,231</sup> Standard PBE functionals have failed in modelling the liquid water properly, as these functionals tend to overpredict binding and structuring, yielding a more ice-like liquid with low diffusivity. In contrast, RPBE tends to have an opposite effect, given the underestimation of binding and structuring (less ordered water), leading to higher diffusivity and a lower density compared to experimental observations.<sup>232,233</sup> The reason behind this discrepancy could be attributed to the fact that standard GGA functionals fail to describe the proper balance between H-bond and vdW forces in water systems.<sup>231,233,234</sup> Lastly, to address the GGA shortcomings in predicting the non-covalent interactions of water and other molecular systems, modern interface models incorporate semi-empirical dispersion corrections by adding an auxiliary energy term to the DFT functionals' energy, as shown in eqn (17).

$$E_{\text{tot}} = E_{\text{DFT}} + E_{\text{disp}} \quad (17)$$

where  $E_{\text{tot}}$  is the total energy,  $E_{\text{DFT}}$  is the energy calculated with a given functional, and  $E_{\text{disp}}$  is the dispersion interaction.<sup>235</sup>

To account for the missing vdW interactions, eqn (17) is implemented in the widely used DFT-D family of approaches (*e.g.*, DFT-D1, D2, D3). Developed by Grimme *et al.*<sup>236</sup> DFT-D methods evaluate  $E_{\text{disp}}$  as a sum of atom-pairwise potential terms using the positions of the atoms and their atomic numbers. Thus, DFT-D methods are often termed as geometry-based methods, providing advantages such as simplicity, computational speed, and robustness.<sup>237</sup> Another approach for deriving the dispersion coefficients is from the electron density, known as the TS method proposed by Tkatchenko,<sup>238</sup> which allows for the dispersion correction to respond to local polarization and charge transfer events. The TS method employs Hirshfeld partitioning to derive effective atomic volumes from the electron density and divide it by the standard volume of the free atom to find the scaling factor. However, these semi-empirical approaches have some limitations in describing the atomic interactions. For example, the standard TS method neglects the electrodynamic screening by



the surrounding dielectric medium, eventually leading to overestimation of energies for condensed or ionic systems.<sup>239</sup> Furthermore, both standard TS and DFT-D methods rely on a pairwise-additive approximation, in which interactions are summed over atom pairs while the influence of the surrounding atomic environment is neglected. For resolving the electrodynamic screening and energy overestimation problem, the many-body dispersion effects should be taken into consideration.<sup>240</sup> The Many-Body Dispersion (MBD) method addresses these deficiencies with pairwise methods by modeling the system as a set of coupled quantum harmonic oscillators. Thus, MBD can capture infinite-order many-body effects, as well as electrodynamic screening, and calculate the binding energies accurately for periodic systems, such as crystals and layered materials. Table 3 provides a summary of the dispersion techniques discussed in this section.

Thus, dispersion corrections significantly improve the predicted density and structure of water when combined with RPBE functionals; however, the same improvement is not observed for PBE. Because PBE already overestimates the strength of directional hydrogen bonding, it tends to overbind aqueous structures. Since vdW dispersion forces are purely attractive, adding a dispersion correction further exacerbates this overbinding problem.<sup>241</sup> A significant advancement in this regard is the Strongly Constrained and Appropriately Normed (SCAN) meta-GGA functional.<sup>242</sup> With the implementation of SCAN, it is possible to predict the structural, electronic, and dynamic properties of liquid water as well as the density difference between water and ice with high accuracy. For example, SCAN predicts the room temperature density for liquid water ( $1.050 \text{ g cm}^{-3}$ ), which is much closer to the experimental value ( $0.997 \text{ g cm}^{-3}$ ) compared to PBE-GGA results ( $\sim 0.850 \text{ g cm}^{-3}$ ).<sup>243</sup> However, for water specifically, SCAN suffers from density-driven errors like self-interaction delocalization, leading to an overcalculation of the 2-body interaction energies in water clusters.<sup>244</sup> Moreover, the inclusion of standard dispersion corrections, such as SCAN-D3(0) or SCAN-D3 (BJ), often degrades the accuracy for water systems by introducing additional attractive interactions into systems that are already overbound.<sup>245</sup> Furthermore, SCAN often overestimates the magnetic properties of certain transition metals and the lattice constants of alkali metals.<sup>246–249</sup> Advanced strategies like Density Corrected-SCAN (DC-SCAN) and SCAN0 may mitigate the self-interaction error of the SCAN functional. However, running first-principles simulations for thousands of steps with these meta-GGA functionals becomes significantly expensive.<sup>245</sup>

While the meta-GGA SCAN functional offers superior accuracy for the prediction of the liquid water properties, its application is limited by the higher computational cost compared to standard GGA functionals. In this context, RPBE functional, when implemented with dispersion corrections like RPBE-D3, serves as an efficient alternative. By reducing the PBE problem of overestimation of water structuring, RPBE-D3 achieves the necessary chemical accuracy for predicting the wetting behavior and density profiles, while maintaining the computational efficiency needed to run longer timescales. After choosing the right functional, the next step is the selection of an appropriate solvation model to make the solid–liquid interface simulation feasible and computationally efficient. The following section discusses the available solvation techniques applied to wettability research, ranging from explicit atomistic models to implicit continuum methods for modeling wettable surface chemistry.

### 5.1.2 DFT-based models: explicit vs. implicit solvation.

DFT can provide a good perspective of electronic structures; however, when the system becomes dynamic, such as the interactions of solid and liquid at the interface, DFT alone cannot provide complete dynamic information. To accurately model solvation in complex aqueous solutions or at solid–liquid interfaces, the trade-off between precision and algorithmic efficiency must be balanced. There are two primary methodologies for this purpose, the explicit (atomistic) solvation models and the implicit (continuum) solvation models. Explicit models such as *ab initio* molecular dynamics (AIMD) or DFT-MD simulations solve the electronic and nuclear equations of motion, treating the entire solute and solvent system from a quantum mechanical perspective to capture the complex liquid environment and interactions.<sup>250</sup> The explicit solvation methodologies are preferred when the solvent actively participates in chemical processes. For interpreting experimental data like NMR, UV-vis, and IR spectra, studying localized phenomena such as reaction free energy profiles<sup>251</sup> H-bond dynamics, proton transfer processes, and the electronic charge distributions are crucial, and explicit models are helpful in these studies.<sup>233,252</sup> AIMD is one of the preferred applied methods in understanding the underlying physics at the solid–liquid interfaces<sup>241,253–255</sup> given that AIMD can provide a fundamental understanding of water/metal interfaces, *e.g.*, strong polarization effects occurring at these interfaces.<sup>256</sup> However, such methods are computationally expensive and commonly used for benchmarking computationally less expensive empirical approaches.<sup>257</sup>

**Table 3** Comparison between the GGA dispersion correction methods

Feature	DFT-D (D2/D3)	TS	MBD
Physics	Geometry (coordination number)	Electron density (Hirshfeld volumes)	Electron density + coupled oscillators
Interaction order	Pairwise + 3-body	Pairwise	Infinite-order many-body
Best application	Rapid screening, organic chemistry	Molecules, non-metallic solids	Metals, interfaces, layered materials, crystals
Computational cost	Negligible	Low	Medium



Early AIMD studies (Car-Parrinello MD or CPMD<sup>258</sup>) were mostly limited to modeling a single adsorbed water layer on metal surfaces. Such a limitation arose due to the high computational cost required for solving the electronic structure at every time step in multilayer water films.<sup>259,260</sup> In addition, and for computational efficiency, these simulations only considered areas where water and metal chemisorption or structured hydrogen bonding occur. CPMD considers the electronic orbitals as dynamical DOFs using a pseudo-Newtonian dynamics,<sup>261</sup> helping to avoid solving the full electronic problem at every step and making the calculation faster. However, this method requires controlling the pseudo-Newtonian dynamics (fictitious mass) to keep the electrons close to the ground state.<sup>262</sup> Another method for AIMD calculation is the Born–Oppenheimer MD (BOMD),<sup>263,264</sup> where the electronic structure is solved to convergence (ground state) for every single time step, ensuring that the nuclei always move on to the true Born–Oppenheimer potential energy surface by fully relaxing the Kohn–Sham orbitals. BOMD can be applied to both metallic and insulating systems without requiring any algorithmic modifications, which is a key advantage of this approach.<sup>235</sup> Furthermore, recent adaptation of BOMD-AIMD to advanced DFT software, *e.g.*, Quantum Espresso, CP2K, has increased its popularity<sup>265,266</sup> and made it possible for robust applications across a variety of systems ranging from clean close-packed metal surfaces (Pt(111), Au(111), Ag(111), Pd(111), and Ru(0001)) at lower temperature of ~100 K (ref. 267 and 268) as well as deformed surfaces like Au(511).<sup>269</sup>

Simulations reveal that step edges can effectively pin water networks, and similar behavior is observed at room temperature, where these pinned networks maintain stable interfacial structures.<sup>270</sup> In addition, for surfaces doped with species such as hydrogen (H), hydroxide (OH), and carbon monoxide (CO), AIMD simulations can be used to elucidate their effects on interfacial water structure by analyzing properties such as the vibrational spectrum, obtained from the Fourier transform of the velocity autocorrelation function (VAF). For example, interfacial water species can be distinguished from VAF vibrational spectrum specific peaks (*e.g.*, O–H stretch). VAF provides the specific orientation and bonding of water species, which induce a net dipole moment, modifying the work function at solid–liquid interfaces.<sup>271</sup> Furthermore, the modification of the work function by the water layer provides an estimation of the Potential of Zero Charge (PZC) at which no excess charge exists on metal surfaces,<sup>272</sup> relative to the Standard Hydrogen Electrode (SHE). The PZC is a reference point for understanding the thermodynamics at solid–liquid interfaces, providing information on the structural orientation of the interfacial water molecules.<sup>273</sup> In addition to describing the structural properties of the water/metal interface, AIMD also captures the electronic polarization effects, such as the significant charge transfer from water layers to Pt(111), creating an interface dipole.<sup>274</sup> To calculate these important surface properties, explicit methods treat every solvent molecule separately by full relaxation of electronic and ionic DOFs, incurring high computational costs even after applying simplifications

such as treating atomic nuclei as classical particles, neglecting quantum effects. There are AIMD methods available that consider quantum nuclear effects, *e.g.*, path-integral (PI-AIMD),<sup>274</sup> but these are computationally heavy, making AIMD only suitable for smaller system sizes and shorter time scales.<sup>275,276</sup> The computational constraints of AIMD make it insufficient for modeling slow processes like ion diffusion at the Electrical Double Layer (EDL), processes that demand nanosecond-scale sampling to achieve statistical accuracy.<sup>277</sup>

An alternative strategy is the implicit solvation method, where the solute is modelled quantum-mechanically while the solvent is treated as a continuous medium, as if the solute is immersed in the solvent. Implicit methods were first applied by Fattebert and Gygi<sup>278</sup> to periodic DFT and also added to the Joint Density Functional Theory (JDFT)<sup>279</sup> with further extension to account for dispersion effects.<sup>280</sup> Thus, instead of tracking detailed atomic movements, this method implicitly averages over the solvent DOFs, promoting a significant reduction in computational cost.<sup>281</sup> For example, implicit models can model the entire EDL by allowing the capacitive charging of the EDL beyond the confines of the finite supercell, which can stretch up to 100 Å, a size impossible for explicit models to handle.<sup>277</sup> Implicit models, *e.g.*, Grand Canonical DFT (GC-DFT), enable simulations of the electrochemical conditions properly by introducing necessary counter charges to maintain the electrode potential fixed and calculate the PZC.<sup>282</sup> GC-DFT is highly efficient for bulk systems with inert solvents; however, to maintain computational efficiency, GC-DFT relies on fitted parameters and inherently neglects directional bonding and steric interactions, which are critical for describing polar solvents like water.<sup>283</sup> Therefore, implicit methods need to be paired with explicit models for capturing complex chemical reactions to maintain a balance between computational efficiency and atomistic accuracy.

**5.1.3 COSMO-RS approach for interfacial tension and wettability.** To overcome the computational limitation and achieve the necessary balance between continuum efficiency and atomistic accuracy discussed above, advanced frameworks such as the Conductor-like Screening Model for Real Solvents (COSMO-RS) are a powerful extension of implicit solvation.

COSMO-RS computes the polarization charge density ( $\sigma$ -profile) of molecules using DFT and applies statistical thermodynamics to quantify intermolecular interactions.<sup>284</sup> COSMO-RS bypasses explicit sampling of large configurational ensembles, to make it faster as well as preserving quantum-chemical accuracy. For fluid interfaces, the COSMO-RS framework uses molecular surface contacts and  $\sigma$ -moments to model macroscopic tension. Early implementations coupled these  $\sigma$ -moments with artificial neural networks to estimate the temperature-dependent surface tension of various organic compounds,<sup>285</sup> which expanded the capability of COSMO-RS to evaluate complex multi-component mixtures, such as cosmetic oils,<sup>286</sup> and refined through direct empirical corrections to calculate both gas–liquid and liquid–liquid surface tensions.<sup>287</sup>



Beyond liquid systems, the thermodynamic outputs generated by COSMO-RS can be related to Young's equation to predict solid surface wettability ( $\theta$ ). Notably, combining DFT with COSMO-RS allows for the calculation of the solvation contribution to solid–liquid interfacial tension.<sup>288</sup> The method predicts the wetting behavior of a solid surface in contact with competing liquids by treating surface features like deprotonation explicitly, showing agreement with experimental water-in-oil contact angles on silica wafers, SAMs, and functionalized polymeric networks.<sup>288</sup> Furthermore, the methodology can be implemented with complex fluids, *e.g.*, ionic liquids, on polar and non-polar substrates by correlating experimental  $\theta$ s with cation–anion pair interaction energies for predicting the wettability.<sup>289</sup>

Integrating DFT-derived electronic structures with statistical thermodynamics *via* COSMO-RS creates a balanced computational method while operating on a timescale that facilitates the screening of solvents, ionic liquids, and solid surface modifications.

## 5.2 Role of electronic structure, adsorption, charge transfer, and polarization

The reactivity and stability of solid–liquid interfaces are governed by the electronic structure of the solid, the dipolar properties of the solvent, and the charge distribution across the interface boundary. First-principle-based methods are well-suited for the description of the underlying physics in these systems.<sup>241</sup> For example, the adsorption mechanism of water on clean transition metal surfaces can be described by the hybridization of water orbitals with the metal d-bands, where water molecules typically bind to the flat surface with their oxygen atoms.<sup>290–292</sup> This electronic interaction can be observed in the local density of states (LDOS) analysis derived from periodic DFT calculations.<sup>293</sup> In addition, at oxide interfaces such as TiO<sub>2</sub>, the electronic structure faces localization of states, and to accurately model these oxides, corrections to standard DFT, such as Hubbard U<sup>294</sup> or hybrid functionals (Hartree–Fock) are needed to correctly describe band gaps and charge trapping.

As discussed in section 4.4, interfacial water adopts specific structural orientations depending on the substrate chemistry. The consequence of this orientation is the modification of the metal work function ( $\phi$ ), which is driven by interfacial polarization.<sup>256</sup> While classical electrostatic arguments might suggest that alternating structural orientations (such as the specific H-up or H-down configurations visualized in MD simulations) should produce opposing dipolar effects, *ab initio* calculations show that both orientational states ultimately lower  $\phi$  due to the charge transfer between the water layer and the metal surface.<sup>274</sup> The magnitude of this charge transfer depends on the degree of electronic hybridization, which is lowest on weakly interacting surfaces like Au(111) but highest on strongly interacting transition metals like Ru.<sup>295</sup> However, when the interfaces are electrified, the orientation of interfacial water shows a dynamic change to the surface charge. For instance, at negative potentials on Au(111), water molecules tend to reori-

ent to the H-down position, maximizing the electrostatic attraction.<sup>273</sup> To model the electrified interfaces, excess charge is often introduced to the electrode. This approach requires a corresponding countercharge in the electrolyte to maintain overall charge neutrality within the simulation cell.

## 6. Challenges and knowledge gaps in wettability research

### 6.1. Conceptual limitations of wettability as a single number

Across the literature, the concept of wettability is traditionally expressed by one reported value, which is a static  $\theta$ . However, a critical analysis of the information presented in the earlier sections indicates that a single parameter/metric is not enough to describe the full wetting behavior in real-world systems.<sup>296</sup> This is because a single macroscopic angle is unable to account for surface roughness, chemical heterogeneity, and the complex molecular structuring that dictates interfacial interactions. As discussed in section 2, classical wetting models assume ideal, smooth, and chemically uniform surfaces with sharp phase boundaries. However, real surfaces are far from ideal, which leads to contact-line pinning and CAH. Hence, real surfaces exhibit a spectrum of metastable states ranging between the ACA and RCA. A single static angle, therefore, captures only one of these many metastable states, which is determined by the deposition history of the droplet and not by the intrinsic material properties. In addition, under confinement, the interfacial region can occupy most of the available liquid domain, which makes a single static angle an ambiguous descriptor of the wetting state.

Another important limitation of a single  $\theta$  is the “wettability transparency”, as detailed in section 4.3.3 through MD simulations. The section highlighted simulations of gold–water interfaces using different force field parameters that predicted identical wetting behavior (complete wetting) but predicted thermal boundary conductance values differed by a factor of five, demonstrating that the macroscopic  $\theta$  does not uniquely define the microscopic physics of the interface. Finally, SCA is insensitive to the molecular-level structuring at the interface, which is a key determinant of interfacial properties at the nanoscale. As described in sections 2.3 and 4.4, solid–liquid interfaces experience density depletion zones, oscillatory layering, and hydrogen-bond network disruptions that can extend up to several nanometers into the liquid. Thus, surfaces with the same  $\theta$  can exhibit different interfacial density profiles that alter fluid transport and adhesion.

### 6.2. Classical Young–Wenzel–Cassie pictures and their breakdown

Many studies continue to interpret data using Young, Wenzel, and Cassie–Baxter equations even though these models are based on idealized assumptions that are often not true for real-world surfaces.<sup>297</sup> Real surfaces experience roughness, chemical heterogeneity, and deformability, violating Young's assumption of a perfectly smooth, chemically homogeneous,



rigid, and inert surface. Hence, real surfaces typically do not exhibit the single thermodynamic equilibrium angle predicted by Young; rather they show a range of metastable  $\theta$  values represented as hysteresis.

The limitations become more pronounced for the Wenzel and CB models for rough and textured surfaces. These models introduced global parameters (roughness factor  $r$  or solid fraction  $f$ ), which are averaged uniformly across the interface, but this review has gathered evidence showing that the global averaging often leads to wrong physical behavior. Kung *et al.*<sup>296</sup> highlighted that this global averaging often fails to match measured apparent  $\theta$  on rough surfaces, as it ignores local variations. In particular, local contact line pinning at geometric edges or defects are ignored, and these features can dominate the actual wetting behavior. For instance, experimental studies by Forsberg *et al.*<sup>56</sup> on pillar-structured surfaces have shown that contact line pinning can cause the APCA to remain high ( $\sim 140^\circ$ – $\sim 160^\circ$ ), contradicting Wenzel's prediction that roughness should enhance the intrinsic hydrophilicity of the material. Furthermore, the review by Erbil<sup>298</sup> highlighted that the Wenzel and CB equations can mathematically fit many experimental datasets; however, the same textured surface can support multiple metastable Cassie, Wenzel, or mixed states depending on the deposition history of the droplet. Another critical discrepancy mentioned in recent research is the failure of these area-based models in capturing the dominant role of the three-phase contact line (TCL). The Wenzel and CB equations are derived by minimizing the surface free energy over the entire solid–liquid contact area. However, experimental evidence indicates that the APCA is governed primarily by the physics at the outermost TCL, rather than by the total area beneath the droplet. Yang *et al.*<sup>70</sup> concluded that droplets with the same outermost TCL configuration exhibit nearly identical  $\theta$ , although the internal wetting beneath the drop differed.

### 6.3. Experimental uncertainties and protocol dependence in contact angle measurements

Contact angle measurements are often treated as straightforward; however, section 3 highlighted that they are strongly protocol-dependent and can shift noticeably even for the same surface. Schuster *et al.*<sup>299</sup> showed that the widely used sessile-drop method is highly sensitive to experimental details such as surface cleanliness, drop volume, and the time elapsed after deposition. Moreover, the authors reported that some of these parameters are not properly reported in many published studies. Consistent with this observation, measurements performed on metal surfaces such as  $\text{Ti}_6\text{Al}_4\text{V}$  and AISI 316 revealed that varying the measurement time from 10 to 190 s can alter the measured water contact angle by approximately 6–8°. In addition, insufficient cleaning increased both the magnitude and dispersion of the measured angles, illustrating how modest changes in protocol can shift measured wettability even for the same nominal surface.<sup>299</sup> Furthermore, on non-ideal surfaces, the sessile-drop contact angle is significantly sensitive to how the droplet imaging is acquired and

processed. This is because locating the contact point and fitting the droplet profile depend on image quality and operator choices. It has been observed that for the same droplet, different fitting algorithms can yield differences in  $\theta$  of up to  $20^\circ$ .<sup>296</sup> Section 3 highlighted some additional uncertainties of conventional measurement techniques; for instance, diffraction and scattering can distort the apparent TCL.<sup>101</sup> In addition, on rough surfaces, gravity-induced sagging near the tangent line hinders contact-point identification.<sup>102</sup>

Beyond static measurements, dynamic methods face their own challenges. The Wilhelmy plate method is considered a standard for measuring dynamic  $\theta$ . However, this methodology requires rigid samples with uniform cross-sections and a wetted perimeter that stays constant during immersion, which is often difficult or impossible to achieve for real components.<sup>300</sup> Although modifications like the advanced Wilhelmy approach by Park *et al.*<sup>300</sup> attempt to reconstruct true perimeters from shape analysis, the precise geometric information requirements are difficult to obtain for real-world components. Additionally, as discussed in section 3.1, Karim and Kavehpour<sup>98</sup> demonstrated that the conventional force balance equation used in the Wilhelmy plate method ignores the viscous forces acting on the moving plate, which introduces substantial errors in dynamic  $\theta$  measurements unless corrected with explicit hydrodynamic models. Similarly, single-fiber dynamic  $\theta$  measurements are experimentally demanding due to the need for highly sensitive microbalances and vibration-free conditions to obtain reliable advancing and receding angles.<sup>36</sup> Moreover, advanced imaging techniques, such as ESEM and optical methods, suffer from geometric limitations<sup>301</sup> given that the  $\theta$  is resolved from 2-D projections that rely on spherical-cap approximations. This becomes difficult for strongly distorted droplets or when viewing angles are oblique. Furthermore, in ESEM, the electron beam itself can induce heating and charging effects that distort droplet shape through evaporation and coalescence, further complicating the accurate measurements.<sup>123,301</sup>

It can be argued that surface contamination is the most critical source of experimental uncertainty, as this resulted in long-standing debates over the intrinsic wettability of fundamental materials. Even for nominally flat gold, reported water  $\theta$  spans from complete wetting ( $0^\circ$ ) to about  $90^\circ$ , leading to conflicts on the classification of the surface as either hydrophilic or hydrophobic.<sup>63,302</sup> Similarly, for decades, graphite and graphene surfaces were classified as hydrophobic, but more recent measurements on carefully cleaned, freshly prepared surfaces suggest their mildly hydrophilic nature.<sup>142</sup> Scientists suggested that airborne hydrocarbons are responsible for most hydrophobic readings<sup>142</sup> and further emphasized that airborne hydrocarbon adsorption produces significant time-dependent changes in  $\theta$  on graphene, graphite, gold, and oxide ceramics. It was also noted that the molecular mechanisms underlying this contamination remain poorly understood, and that more effective strategies for removing and inhibiting airborne contamination are still needed.<sup>142</sup>



#### 6.4. Multiscale modeling and force-field limitations

A major bottleneck in wettability research is the absence of a single simulation technique capable of capturing interfacial physics for both micro- and macro-scales. DFT provides the necessary accuracy to treat electronic polarization, charge transfer, and specific adsorption, but DFT simulations are computationally expensive and restricted to systems of a few hundred atoms, which is insufficient to study droplet spreading and  $\theta$  relaxation. On the other hand, classical MD simulation can access larger systems and time scales; nonetheless, these simulations rely on empirical force fields that are fundamentally approximate and often lack transferability.<sup>63</sup> This is why multiscale approaches that combine DFT-level information with MD sampling (for example, DFT-CES) are becoming attractive.<sup>63,82</sup> These approaches can connect microscopic adsorption structure and dynamics to wetting descriptors, like  $W_{ad}$ , but they are also limited by the inherent trade-offs of the underlying techniques.<sup>63,82</sup>

A central limitation highlighted in section 4 is force-field non-uniqueness and sensitivity. Quantitative prediction of  $\theta$  at the atomistic level remains uncertain since the wetting behavior is sensitive to the solid-liquid non-bonded interaction parameters.<sup>303</sup> Such predictions also depend on whether additional cross-terms are included with the non-bonded interaction or what cutoff is used. Recent studies emphasize that empirical force fields derived from different optimization targets can yield vastly different interfacial predictions for the same material pair.<sup>61,303</sup> For instance, Gonzalez-Valle *et al.*<sup>60</sup> analyzed a broad range of literature parameter sets for graphite-water interfaces and found that these parameters predict a wide spectrum of wetting conditions ( $\theta$  ranging from  $<10^\circ$  to  $79^\circ$ ) for the nominally same physical interface and have significant effect on the interfacial thermal transport; a similar ambiguity was discussed for Au-water systems in section 4. In the case of Au-water, nine solid-liquid interaction parameter sets, which were derived from different target properties and even different functional forms, all predicted near-complete wetting. However, the thermal boundary conductance determined using those models varied by roughly a factor of 4–5.<sup>41</sup>

Recent methodological advances offer concrete pathways to mitigate the force-field non-uniqueness and multiscale modeling challenges outlined above. As discussed in section 4.3.5, machine learning interatomic potentials (MLIPs) trained on *ab initio* reference data can capture many-body polarization, charge redistribution, and dispersion effects without relying on fixed functional forms or empirical mixing rules, thereby reducing the parametric ambiguity inherent in classical potentials.<sup>304</sup> When combined with multiscale frameworks such as DFT-CES<sup>82,303</sup> or adaptive force-matching approaches,<sup>188</sup> MLIPs can serve as an intermediate bridge: DFT-level accuracy informs the potential energy surface at the interface, while the computational efficiency of the learned potential enables the large system sizes and long simulation timescales needed to converge contact angles and interfacial free energies. Similarly, reactive force fields such as ReaxFF<sup>206,207</sup> address a specific

limitation of classical non-reactive potentials by modeling dissociative adsorption and surface hydroxylation events that can fundamentally alter the wetting state, particularly on oxide and metal surfaces (see section 4.3.5 for specific applications). A critical remaining challenge is closing the validation loop: force fields or MLIPs optimized at one scale must be systematically validated against both quantum mechanical benchmarks and experimental observables simultaneously, rather than against either in isolation. Adopting multi-objective optimization frameworks<sup>198,199</sup> that target contact angles, adsorption energies, interfacial structure, and transport properties concurrently, as recommended in section 7.2, would help ensure that the resulting potentials are not only accurate for the calibration target but also transferable across interfacial properties, thereby directly addressing the non-uniqueness problem documented throughout this section.

In confined flows, modelling sensitivity creates similar ambiguities. For nanoconfined water in carbon slits, MD simulations reveal that the predicted slip length is very sensitive to the chosen solid-liquid interaction parameters.<sup>61</sup> Paniagua-Guerra *et al.*<sup>61</sup> demonstrated that interface models tuned to produce the same macroscopic  $\theta$  ( $64.4^\circ$ ) can yield slip lengths that differ from 27 nm to 62 nm. Ultimately, these examples highlight the challenges in multiscale computational wettability research. Classical force fields are often calibrated against experimental values of  $\theta$ , but those experimental findings are also uncertain due to surface contamination and protocol dependence. Hence, a parameter set may be effectively calibrated to reproduce contaminated states rather than intrinsic material properties.

#### 6.5. Size dependence and line-tension effects

Droplet size dependence and line tension add further ambiguities in the nanoscale results due to the breakdown of continuum physics. Theoretical treatments based on the modified Young's equation typically suggest minor corrections to the  $\theta$  due to line tension. However, experiments report widely scattered behaviors, such as decreasing, increasing, or size-independent apparent angles.<sup>296,298</sup> In addition, the inferred line tension values span orders of magnitude.<sup>296,298</sup> Park *et al.*<sup>305</sup> utilized Cryo-FIB/SEM to directly image microscale droplets and found that standard line-tension extensions of Young's law failed to reproduce the observed size dependence and yield unphysically large values of line tension. The authors claimed that these discrepancies may arise from the non-equilibrium nature of micro-sessile droplets, where rapid evaporation and condensation kinetics create complex thermodynamics that static continuum models cannot capture.

Section 4.2 discussed how size and line tension effects manifest in molecular simulations, where size-dependent contact angles are routinely observed for droplets below 10–20 nm. In contrast, most experimental measurements involve millimeter-scale droplets where line tension contributions are often assumed negligible. The graphite-water system serves as an instructive case study to illustrate this scale gap. In MD simulations, Werder *et al.*<sup>39</sup> demonstrated



that the predicted contact angle varies from approximately 40° to over 130° depending solely on Lennard-Jones cross-interaction parameters, with their calibrated value yielding ~86° at nanometer-scale radii. Experimentally, however, reported contact angles on nominally identical graphite and graphene surfaces span from below 10° to above 90°, a spread largely attributable to airborne hydrocarbon contamination as documented in section 6.3.<sup>306</sup> This comparison highlights that simulations model atomically clean surfaces while experimental substrates contain heterogeneity, defects, and adsorbates that independently modify the effective contact line energy.

This case study reveals that the simulation–experiment gap arises from three compounding factors: (1) force-field non-uniqueness in MD; (2) surface contamination masking intrinsic wetting behavior in experiments; and (3) scale mismatch between nanometer-scale simulations and millimeter-scale experiments. A closed-loop validation strategy therefore requires simulation of droplets spanning nanometer to mesoscopic regimes, experimental measurements on contamination-controlled and atomically characterized surfaces, and comparison based on interfacial free energies rather than contact angle geometry alone.

### 6.6. Linking nanoscale interfacial structure to macroscopic contact angle

Another limitation is the missing universal bridge between microscopic interfacial structure and macroscopic observables. Many studies agree that water near solids can show modified dynamics relative to the bulk, including layering, orientational ordering, and density changes near the interface, and these structural descriptors do not correlate universally with the contact angle.<sup>61,62,307,308</sup> In addition, there is a dispute among researchers on whether a thermodynamically driven low-density depletion layer exists at hydrophobic interfaces. Experimental results range from distinct depletion gaps to intimate contact or nanobubble formation.<sup>307</sup> On the other hand, while some X-ray and neutron scattering studies identify a depletion region with a thickness of a few angstroms, others report no detectable gap.<sup>307,308</sup> Therefore, both the fundamental existence and the size of the hydrophobic depletion zone remain unresolved.

Moreover, MD simulations on alumina-water systems show that standard wettability descriptors such as  $\theta$ ,  $W_{\text{ad}}$ , total solid–liquid interaction energy, and interfacial H-bond density cannot individually predict the thermal boundary conductance in a consistent way, suggesting that no single wettability descriptor is universally adequate.<sup>87</sup> Taken together, studies show that thermodynamic quantities, hydrogen-bonding metrics, and vibrational spectra can help predict wettability trends for a specific group of materials. But a generally predictive, cross-material framework that translates these microscopic descriptors onto macroscopic wetting behavior is still lacking.<sup>82,87,309</sup>

### 6.7. Bridging experimental and simulation scales

A central challenge in wettability research is the gap between nanoscale molecular simulations and macroscopic experi-

mental measurements. Simulations typically probe nanometer-sized droplets or thin films on idealized, atomically flat surfaces, whereas experiments measure millimeter-scale droplets on chemically heterogeneous and rough substrates. Direct comparison of contact angles; therefore, conflates intrinsic thermodynamic behavior with scale-dependent effects such as roughness and line tension. Bridging this mismatch requires structured experimental–simulation collaborative verification strategies rather than sole reliance on geometric droplet fitting.

One effective strategy is hierarchical observable matching. Instead of validating simulations exclusively against macroscopic contact angles, intermediate thermodynamic quantities should be compared. These include liquid–vapor surface tension, solid surface energy, and work of adhesion derived from Young–Dupré thermodynamics.<sup>310</sup> At the molecular scale, adsorption energetics and interfacial free energies obtained *via* thermodynamic integration or cleaving-wall methods can be mapped to macroscopic observables within the assumptions of Young-type thermodynamic models, enabling thermodynamically consistent comparisons.<sup>158,159</sup> For example, studies of graphite–water interfaces have demonstrated how small variations in cross-interaction parameters can produce large changes in apparent contact angle, emphasizing the need for energetic anchoring rather than geometric agreement alone.<sup>39</sup>

A second bridging pathway involves direct comparison of interfacial structural observables. Interfacial water density layering and molecular orientation can be probed experimentally using X-ray or neutron reflectivity and compared directly to simulated density profiles. As demonstrated by X-ray reflectivity measurements combined with molecular dynamics simulations of interfacial density depletion at hydrophobic interfaces, such structural comparisons enable quantitative assessment of near-surface water organization beyond macroscopic contact angle measurements.<sup>217,311</sup> These structural benchmarks provide an intermediate validation scale that is less sensitive to droplet size effects and surface defects, allowing intrinsic interfacial ordering and depletion phenomena to be evaluated consistently across experiment and simulation.

A third strategy is controlled surface replication. Experimental collaborators can fabricate atomically flat or chemically well-characterized substrates whose roughness, functional groups, and oxidation states are quantified using AFM, XPS, or Raman spectroscopy. Simulations can then explicitly reproduce these surface terminations and defect densities. This direct structural matching reduces ambiguity arising from unknown heterogeneity and allows intrinsic wetting behavior to be isolated.

Finally, multiscale integration offers a systematic route to reconcile protocol dependence. *Ab initio* calculations or machine-learned interatomic potentials trained on density functional theory data can capture adsorption energetics and many-body polarization effects at the atomic level.<sup>312,313</sup> These energetics can then parameterize classical molecular dynamics



simulations of larger droplets, while continuum capillary models incorporate experimentally measured roughness factors to predict apparent macroscopic angles. Such multi-scale feedback loops move wettability research from qualitative agreement toward predictive, reproducible solid–liquid interface modeling.

Together, these collaborative verification strategies transform experimental–simulation comparison from a single-parameter validation problem into a thermodynamically and structurally consistent multilevel framework.

## 7. Conclusions and future directions

This review has combined insights from experimental investigations, MD simulations, and first-principles theory to establish a comprehensive understanding of surface wettability. The cross-platform analysis in this study identified several key findings and persistent challenges.

### 7.1 Summary of key findings

The classical frameworks of Young, Wenzel, and Cassie–Baxter provide foundational descriptions of wetting behavior. However, these models fail to capture the complexity of real surfaces where nanoscale roughness, chemical heterogeneity, and metastable states lead to significant deviations from the theory. At the nanoscale,  $\theta$  alone is often an incomplete descriptor given that interfacial density profiles, hydrogen-bond networks, depletion lengths, and entropy can play an important role in wetting behavior. Experimental characterization faces constant challenges, including surface contamination, measurement protocol variability, and the difficulty of capturing true equilibrium states. The debates over the intrinsic wettability of gold and graphitic surfaces, where reported  $\theta$  ranges from complete wetting to hydrophobic, show how airborne contamination and preparation protocols can dominate observed behavior. On the other hand, MD simulations offer atomic-level insight into the wetting phenomena but introduce several uncertainties. Predicted wettability strongly depends on the chosen water model, solid-phase potential, and cross-species interaction parameters. Thus, depending on the employed force field combination, the same material can appear hydrophobic or exhibit complete wetting. For example, standard Lorentz–Berthelot mixing rules can lead to deviations from experimental findings; moreover, parameters optimized for bulk properties do not always transfer cleanly to interfacial wetting. Alternatively, first-principles calculations provide accurate predictions of electronic structure and adsorption energies, but these methods are limited to small system sizes and timescales. An additional complexity in first-principles simulations is the choice of exchange–correlation functional and dispersion correction that can significantly affect predicted water structure and surface interactions. All these difficulties and drawbacks make no single approach universally optimal across different materials and interfacial systems.

In addition, several fundamental knowledge gaps continue to hinder reliable predictions of wetting behavior. A central challenge is the lack of a universal framework that connects the microscopic molecular arrangement at the interface to the macroscopic  $\theta$ . While molecular features such as interfacial layering, hydrogen bonding patterns, and local depletion effects are known to influence wetting, their direct relationship to continuum scale quantities remains poorly defined. Furthermore, many studies focus primarily on energetic contributions and neglect entropic effects, even though entropy can modify the interfacial free energy sufficiently to change overall wetting trends. Finally, the literature has not yet reached consensus on the role of line tension or on how the APCA depends on droplet size, further complicating the interpretation and comparison of both experimental and computational results.

### 7.2 Guidelines for future research

The primary concerns identified in this review can be effectively addressed through the implementation of the following recommendations:

*Standardized experimental protocols:* standardizing wetting measurements is essential for improving reliability and comparability. Experiments should be conducted under controlled atmospheric conditions, with careful documentation of surface preparation procedures, cleaning methods, and the time elapsed between surface preparation and measurement. Furthermore, reporting both ACA and RCA, along with contact angle hysteresis, provides a more complete characterization than relying solely on static  $\theta$  values, better capturing surface heterogeneity, pinning effects, and dynamic wetting behavior.

*Unified force field frameworks:* the traditional approach of combining separate models for liquids and solids relies on mixing rules that introduce compounding inconsistencies. Prioritizing frameworks that maintain internal consistency across all interaction types, such as DFT-informed potentials or reactive force fields can reduce ambiguity and treat cohesive and adhesive interactions within a single model. Careful parameterization and validation for the target interface remain essential regardless of the framework chosen.

*Multi-property validation and multi-objective optimization:* force field calibration should not rely on a single target property like  $\theta$ , as different parameter sets can match the same angle while producing different interfacial structures and transport properties. Future parameterization should simultaneously target work of adhesion, transport metrics such as thermal boundary conductance, and interfacial structural properties such as hydrogen-bond statistics and density profiles. Multi-objective optimization frameworks, including genetic algorithm-based approaches and Bayesian optimization that identify Pareto-optimal parameter sets balancing multiple target properties, offer a principled route to achieving this, as discussed in section 4.3.5.

*Entropic decomposition:* simulation studies should separate interfacial free energies into enthalpic and entropic contributions to understand whether wetting trends are driven by



energy or entropy. This decomposition is particularly important for systems where temperature-dependent wetting behavior suggests significant entropic effects, as discussed in section 4.5.

**Emerging potentials:** machine learning interatomic potentials trained on *ab initio* reference data and reactive force fields such as ReaxFF offer concrete pathways beyond classical empirical potentials. MLIPs capture many-body polarization and dispersion effects without fixed functional forms, while ReaxFF enables modeling of dissociative adsorption and surface hydroxylation that govern wetting on oxide and metal surfaces. Systematic deployment of these potentials for contact angle and interfacial free energy calculations remains an important open direction, as outlined in section 4.3.5.

**Multiscale integration:** bridging the vast difference in time and length scales requires hybrid approaches coupling electronic accuracy with computational efficiency. Frameworks such as DFT-CES or machine-learned potentials trained on *ab initio* data provide a practical route, where DFT-level accuracy informs interfacial energetics and classical MD or continuum models extend to experimentally relevant scales. Critically, force fields or MLIPs optimized at one scale must be validated against both quantum mechanical benchmarks and experimental observables simultaneously, closing the validation loop discussed in section 6.4.

**Experimental–simulation collaborative verification:** bridging the gap between nanoscale simulations and macroscopic experiments requires structured collaborative strategies beyond simple contact angle comparison. These include hierarchical observable matching using intermediate thermodynamic quantities such as work of adhesion, direct comparison of interfacial structural observables *via* X-ray or neutron reflectivity, and controlled surface replication where simulations explicitly reproduce experimentally characterized surface terminations and defect densities. Such strategies, outlined in section 6.7, transform experimental–simulation comparison from a single-parameter validation into a thermodynamically and structurally consistent multilevel framework.

Addressing these knowledge gaps collectively may enable more reliable prediction of wetting phenomena and accelerate the rational design of surfaces with tailored wettability.

## Author contributions

Emdadul Haque Chowdhury: conceptualization, investigation (literature survey), data curation (literature), formal analysis (critical synthesis), writing – original draft, writing – review & editing. Md Shahed Hossain Sohan: investigation (literature survey), data curation (literature), formal analysis (critical synthesis), writing – original draft, writing – review & editing. C. Ulises Gonzalez-Valle: investigation (literature survey), data curation (literature), formal analysis (critical synthesis), writing – original draft, writing – review & editing. Adri C. T. van Duin: supervision, writing – review & editing. Bladimir Ramos-Alvarado: conceptualization, supervision,

project administration, funding acquisition, writing – original draft, writing – review & editing.

## Conflicts of interest

There are no conflicts to declare.

## Data availability

No primary research results, software or code have been included, and no new data were generated or analyzed as part of this review.

## Acknowledgements

This work was supported by the National Science Foundation, USA (award number: 2430793).

## References

- 1 L. Gao and T. J. McCarthy, Wetting 101°, *Langmuir*, 2009, **25**, 14105–14115.
- 2 Y. Wu and N. R. Aluru, Graphitic Carbon–Water Nonbonded Interaction Parameters, *J. Phys. Chem. B*, 2013, **117**, 8802–8813.
- 3 M. Maccarini, *et al.*, Density Depletion at Solid–Liquid Interfaces: a Neutron Reflectivity Study, *Langmuir*, 2007, **23**, 598–608.
- 4 S. Li, J. Huang, Z. Chen, G. Chen and Y. Lai, A review on special wettability textiles: theoretical models, fabrication technologies and multifunctional applications, *J. Mater. Chem. A*, 2017, **5**, 31–55.
- 5 J. Genzer and K. Efimenko, Recent developments in superhydrophobic surfaces and their relevance to marine fouling: a review, *Biofouling*, 2006, **22**, 339–360.
- 6 M. Liravi, H. Pakzad, A. Moosavi and A. Nouri-Borujerdi, A comprehensive review on recent advances in superhydrophobic surfaces and their applications for drag reduction, *Prog. Org. Coat.*, 2020, **140**, 105537.
- 7 L. Wen, Y. Tian and L. Jiang, Bioinspired Super-Wettability from Fundamental Research to Practical Applications, *Angew. Chem., Int. Ed.*, 2015, **54**, 3387–3399.
- 8 D. Zhu, *et al.*, Mimicking the Rice Leaf—From Ordered Binary Structures to Anisotropic Wettability, *Langmuir*, 2010, **26**, 14276–14283.
- 9 X. Gao and L. Jiang, Water-repellent legs of water striders, *Nature*, 2004, **432**, 36.
- 10 Y. Zheng, *et al.*, Directional water collection on wetted spider silk, *Nature*, 2010, **463**, 640–643.
- 11 B. Bhushan and Y. C. Jung, Natural and biomimetic artificial surfaces for superhydrophobicity, self-cleaning, low adhesion, and drag reduction, *Prog. Mater. Sci.*, 2011, **56**, 1–108.



- 12 K. Liu and L. Jiang, Bio-Inspired Self-Cleaning Surfaces, *Annu. Rev. Mater. Res.*, 2012, **42**, 231–263.
- 13 D. V. Margiotta, *et al.*, *The Lotus coating for space exploration: a dust mitigation tool*, in *Optical System Contamination: Effects, Measurements, and Control 2010*, SPIE, 2010, vol. 7794, pp. 143–149.
- 14 L. Cao, A. K. Jones, V. K. Sikka, J. Wu and D. Gao, Anti-Icing Superhydrophobic Coatings, *Langmuir*, 2009, **25**, 12444–12448.
- 15 Z. Wang, M. Elimelech and S. Lin, Environmental Applications of Interfacial Materials with Special Wettability, *Environ. Sci. Technol.*, 2016, **50**, 2132–2150.
- 16 N. Miljkovic and E. N. Wang, Condensation heat transfer on superhydrophobic surfaces, *MRS Bull.*, 2013, **38**, 397–406.
- 17 S. Martin, *Bioinspired Surfaces Adapted from Lotus Leaves for Superliquiphobic Properties*, The Ohio State University, 2017.
- 18 J. F. Bringley, T. Qiao and S. Sunderrajan, *Stain and soil resistant textile article*, 2011.
- 19 S. Wang, L. Feng and L. Jiang, One-Step Solution-Immersion Process for the Fabrication of Stable Bionic Superhydrophobic Surfaces, *Adv. Mater.*, 2006, **18**, 767–770.
- 20 E. Hermelin, *et al.*, Ultrafast Electrosynthesis of High Hydrophobic Polypyrrole Coatings on a Zinc Electrode: Applications to the Protection against Corrosion, *Chem. Mater.*, 2008, **20**, 4447–4456.
- 21 S. S. Ingle, *et al.*, A review on transparent superhydrophobic coatings for self-cleaning solar cell panels: Its fabrication, robustness and industrial implementation, *Surf. Interfaces*, 2025, **70**, 106794.
- 22 M. Zhou, *et al.*, Visible light-induced photocatalytic and antibacterial adhesion properties of superhydrophilic TiO<sub>2</sub> nanoparticles, *Sci. Rep.*, 2024, **14**, 7940.
- 23 W. Zhang, *et al.*, Superhydrophobic and superoleophilic PVDF membranes for effective separation of water-in-oil emulsions with high flux, *Adv. Mater.*, 2013, **25**, 2071–2076.
- 24 X. Zhang, H. Liu and L. Jiang, Wettability and Applications of Nanochannels, *Adv. Mater.*, 2019, **31**, 1804508.
- 25 K. Wu, *et al.*, Wettability effect on nanoconfined water flow, *Proc. Natl. Acad. Sci. U. S. A.*, 2017, **114**, 3358–3363.
- 26 A. A. Shuvo, L. E. Paniagua-Guerra, J. Choi, S. H. Kim and B. Ramos-Alvarado, Hydrodynamic slip in nanoconfined flows: a review of experimental, computational, and theoretical progress, *Nanoscale*, 2025, **17**, 635–660.
- 27 X. Pan, *et al.*, Enhanced ethanol production inside carbon-nanotube reactors containing catalytic particles, *Nat. Mater.*, 2007, **6**, 507–511.
- 28 A. B. Grommet, M. Feller and R. Klajn, Chemical reactivity under nanoconfinement, *Nat. Nanotechnol.*, 2020, **15**, 256–271.
- 29 Y. Chai, W. Dai, G. Wu, N. Guan and L. Li, Confinement in a Zeolite and Zeolite Catalysis, *Acc. Chem. Res.*, 2021, **54**, 2894–2904.
- 30 C. Bie, *et al.*, Nanoconfinement Effects in Electrocatalysis and Photocatalysis, *Small*, 2025, **21**, 2411184.
- 31 D. Lin, *et al.*, Layered reduced graphene oxide with nanoscale interlayer gaps as a stable host for lithium metal anodes, *Nat. Nanotechnol.*, 2016, **11**, 626–632.
- 32 E. J. Falde, S. T. Yohe, Y. L. Colson and M. W. Grinstaff, Superhydrophobic materials for biomedical applications, *Biomaterials*, 2016, **104**, 87–103.
- 33 H. Ge, *et al.*, Up to Date Review of Nature-Inspired Superhydrophobic Textiles: Fabrication and Applications, *Materials*, 2023, **16**, 7015.
- 34 H. Zhou, Q. Li, Z. Zhang, X. Wang and H. Niu, Recent Advances in Superhydrophobic and Antibacterial Cellulose-Based Fibers and Fabrics: Bio-inspiration, Strategies, and Applications, *Adv. Fiber Mater.*, 2023, **5**, 1555–1591.
- 35 S. Chen, *et al.*, Superhydrophobic and superhydrophilic polyurethane sponge for wound healing, *Chem. Eng. J.*, 2022, **446**, 136985.
- 36 M. A. Hubbe, D. J. Gardner and W. Shen, Contact angles and wettability of cellulosic surfaces: A review of proposed mechanisms and test strategies, *BioRes*, 2015, **10**, 8657–8749.
- 37 R. N. Wenzel, RESISTANCE OF SOLID SURFACES TO WETTING BY WATER, *Ind. Eng. Chem.*, 1936, **28**, 988–994.
- 38 A. B. D. Cassie and S. Baxter, Wettability of porous surfaces, *Trans. Faraday Soc.*, 1944, **40**, 546–551.
- 39 T. Werder, J. H. Walther, R. L. Jaffe, T. Halicioglu and P. Koumoutsakos, On the Water–Carbon Interaction for Use in Molecular Dynamics Simulations of Graphite and Carbon Nanotubes, *J. Phys. Chem. B*, 2003, **107**, 1345–1352.
- 40 R. L. Jaffe, P. Gonnet, T. Werder, J. H. Walther and P. Koumoutsakos, Water–Carbon Interactions 2: Calibration of Potentials using Contact Angle Data for Different Interaction Models, *Mol. Simul.*, 2006, **30**, 205–216.
- 41 L. E. Paniagua-Guerra and B. Ramos-Alvarado, Thermal transport across flat and curved gold–water interfaces: Assessing the effects of the interfacial modeling parameters, *J. Chem. Phys.*, 2023, **158**, 134717.
- 42 H.-J. Butt, D. S. Golovko and E. Bonaccorso, On the Derivation of Young's Equation for Sessile Drops: Nonequilibrium Effects Due to Evaporation, *J. Phys. Chem. B*, 2007, **111**, 5277–5283.
- 43 J. W. Drelich, *et al.*, Contact angles: history of over 200 years of open questions, *Surf. Innovations*, 2019, **8**, 3–27.
- 44 K. Seo, *et al.*, *Re-derivation of Young's Equation, Wenzel Equation, and Cassie-Baxter Equation Based on Energy Minimization*, in *Surface Energy*, IntechOpen, 2015. DOI: [10.5772/61066](https://doi.org/10.5772/61066).
- 45 H. Y. Erbil, The debate on the dependence of apparent contact angles on drop contact area or three-phase contact line: A review, *Surf. Sci. Rep.*, 2014, **69**, 325–365.
- 46 D. Quéré, Wetting and Roughness, *Annu. Rev. Mater. Res.*, 2008, **38**, 71–99.



- 47 C. H. Kung, P. K. Sow, B. Zahiri and W. Mérida, Assessment and Interpretation of Surface Wettability Based on Sessile Droplet Contact Angle Measurement: Challenges and Opportunities, *Adv. Mater. Interfaces*, 2019, **6**, 1900839.
- 48 C. Ma, *et al.*, Plasma-controlled surface wettability: recent advances and future applications, *Int. Mater. Rev.*, 2023, **68**, 82–119.
- 49 K. Liu, X. Yao and L. Jiang, Recent developments in bio-inspired special wettability, *Chem. Soc. Rev.*, 2010, **39**, 3240–3255.
- 50 L. Gao and T. J. McCarthy, How Wenzel and Cassie Were Wrong, *Langmuir*, 2007, **23**, 3762–3765.
- 51 P. S. H. Forsberg, C. Priest, M. Brinkmann, R. Sedev and J. Ralston, Contact Line Pinning on Microstructured Surfaces for Liquids in the Wenzel State, *Langmuir*, 2010, **26**, 860–865.
- 52 A. Lafuma and D. Quéré, Superhydrophobic states, *Nat. Mater.*, 2003, **2**, 457–460.
- 53 H. B. Eral, D. J. C. M. 't Mannetje and J. M. Oh, Contact angle hysteresis: a review of fundamentals and applications, *Colloid Polym. Sci.*, 2013, **291**, 247–260.
- 54 J. Sun and P. B. Weisensee, Tailoring wettability to push the limits of condensation, *Curr. Opin. Colloid Interface Sci.*, 2023, **67**, 101739.
- 55 Y. Kwon, *et al.*, Is the Cassie–Baxter Formula Relevant?, *Langmuir*, 2010, **26**, 17528–17531.
- 56 P. S. H. Forsberg, C. Priest, M. Brinkmann, R. Sedev and J. Ralston, Contact Line Pinning on Microstructured Surfaces for Liquids in the Wenzel State, *Langmuir*, 2010, **26**, 860–865.
- 57 W. Choi, A. Tuteja, J. M. Mabry, R. E. Cohen and G. H. McKinley, A modified Cassie–Baxter relationship to explain contact angle hysteresis and anisotropy on non-wetting textured surfaces, *J. Colloid Interface Sci.*, 2009, **339**, 208–216.
- 58 M. Yamaguchi, *et al.*, Fabrication of nano-periodic structures and modification of the Wenzel model to estimate contact angle, *Sens. Actuators, A*, 2014, **212**, 87–92.
- 59 T. L. Liu, Z. Chen and C.-J. Kim, A dynamic Cassie–Baxter model, *Soft Matter*, 2015, **11**, 1589–1596.
- 60 C. U. Gonzalez-Valle, L. E. Paniagua-Guerra and B. Ramos-Alvarado, Implications of the Interface Modeling Approach on the Heat Transfer across Graphite–Water Interfaces, *J. Phys. Chem. C*, 2019, **123**, 22311–22323.
- 61 L. E. Paniagua-Guerra, C. U. Gonzalez-Valle and B. Ramos-Alvarado, Effects of the Interfacial Modeling Approach on Equilibrium Calculations of Slip Length for Nanoconfined Water in Carbon Slits, *Langmuir*, 2020, **36**, 14772–14781.
- 62 B. Ramos-Alvarado, S. Kumar and G. P. Peterson, On the wettability transparency of graphene-coated silicon surfaces, *J. Chem. Phys.*, 2016, **144**, 014701.
- 63 S. Gim, K. J. Cho, H.-K. Lim and H. Kim, Structure, Dynamics, and Wettability of Water at Metal Interfaces, *Sci. Rep.*, 2019, **9**, 14805.
- 64 C. G. Jothi Prakash and R. Prasanth, Approaches to design a surface with tunable wettability: a review on surface properties, *J. Mater. Sci.*, 2021, **56**, 108–135.
- 65 R. C. Tolman, The Effect of Droplet Size on Surface Tension, *J. Chem. Phys.*, 1949, **17**, 333–337.
- 66 A. Amirfazli and A. W. Neumann, Status of the three-phase line tension: a review, *Adv. Colloid Interface Sci.*, 2004, **110**, 121–141.
- 67 W. Klauser, F. T. von Kleist-Retzow, S. Fatikow, *et al.*, Line Tension and Drop Size Dependence of Contact Angle at the Nanoscale, *Nanomaterials*, 2022, **12**, 369.
- 68 J. Zhang, P. Wang, M. K. Borg, J. M. Reese and D. Wen, A critical assessment of the line tension determined by the modified Young's equation, *Phys. Fluids*, 2018, **30**, 082003.
- 69 L. Boruvka and A. W. Neumann, Generalization of the classical theory of capillarity, *J. Chem. Phys.*, 1977, **66**, 5464–5476.
- 70 C. Yang, F. He and P. Hao, The apparent contact angle of water droplet on the micro-structured hydrophobic surface, *Sci. China: Chem.*, 2010, **53**, 912–916.
- 71 C. W. Extrand, Contact Angles and Hysteresis on Surfaces with Chemically Heterogeneous Islands, *Langmuir*, 2003, **19**, 3793–3796.
- 72 D. Öner and T. J. McCarthy, Ultrahydrophobic Surfaces., Effects of Topography Length Scales on Wettability, *Langmuir*, 2000, **16**, 7777–7782.
- 73 G. McHale, Cassie and Wenzel: Were They Really So Wrong?, *Langmuir*, 2007, **23**, 8200–8205.
- 74 L. Gao and T. J. McCarthy, How Wenzel and Cassie Were Wrong, *Langmuir*, 2007, **23**, 3762–3765.
- 75 D. Bonn, J. Eggers, J. Indekeu, J. Meunier and E. Rolley, Wetting and spreading, *Rev. Mod. Phys.*, 2009, **81**, 739–805.
- 76 R. G. Cox, The dynamics of the spreading of liquids on a solid surface. Part 1. Viscous flow, *J. Fluid Mech.*, 1986, **168**, 169–194.
- 77 K. S. Ha, T. Wang, L. Zhang and J. Yuyan, Hydrodynamic analysis of the advancing dynamic contact angle in micro-tube, *J. Mech. Sci. Technol.*, 2018, **32**, 5305–5314.
- 78 T. D. Blake and J. M. Haynes, Kinetics of liquidliquid displacement, *J. Colloid Interface Sci.*, 1969, **30**, 421–423.
- 79 R. Sedev, The molecular-kinetic approach to wetting dynamics: Achievements and limitations, *Adv. Colloid Interface Sci.*, 2015, **222**, 661–669.
- 80 S. R. Carlson, *et al.*, Modeling Water Interactions with Graphene and Graphite via Force Fields Consistent with Experimental Contact Angles, *J. Phys. Chem. Lett.*, 2024, **15**, 6325–6333.
- 81 L. Hakim, I. Kurniawan, E. Indahyanti and I. Pradana, Molecular Dynamics Simulation of Wetting Behavior: Contact Angle Dependency on Water Potential Models, *ICS Phys. Chem.*, 2021, **1**, 10.
- 82 F. Domínguez-Flores, T. Kiljunen, A. Groß, S. Sakong and M. M. Melander, Metal–water interface formation:



- Thermodynamics from ab initio molecular dynamics simulations, *J. Chem. Phys.*, 2024, **161**, 044705.
- 83 F. Leroy, S. Liu and J. Zhang, Parametrizing Nonbonded Interactions from Wetting Experiments via the Work of Adhesion: Example of Water on Graphene Surfaces, *J. Phys. Chem. C*, 2015, **119**, 28470–28481.
- 84 F. Taherian, V. Marcon, N. F. van der Vegt and F. Leroy, What Is the Contact Angle of Water on Graphene?, *Langmuir*, 2013, **29**, 1457–1465.
- 85 B. Ramos-Alvarado, S. Kumar and G. P. Peterson, Solid-Liquid Thermal Transport and Its Relationship with Wettability and the Interfacial Liquid Structure, *J. Phys. Chem. Lett.*, 2016, **7**, 3497–3501.
- 86 L. Zhao and J. Cheng, Characterizing the bifurcating configuration of hydrogen bonding network in interfacial liquid water and its adhesion on solid surfaces, *RSC Adv.*, 2019, **9**, 16423–16430.
- 87 C. U. Gonzalez-Valle and B. Ramos-Alvarado, Molecular Dynamics Simulations of Wettability, Thermal Transport, and Interfacial Liquid Structuring at the Nanoscale in Polar Solid-Liquid Interfaces, *ACS Appl. Nano Mater.*, 2021, **4**, 3821–3832.
- 88 T. Huhtamäki, X. Tian, J. T. Korhonen and R. H. A. Ras, Surface-wetting characterization using contact-angle measurements, *Nat. Protoc.*, 2018, **13**, 1521–1538.
- 89 J. M. Schuster, C. E. Schvezov and M. R. Rosenberger, Influence of Experimental Variables on the Measure of Contact Angle in Metals Using the Sessile Drop Method, *Procedia Mater. Sci.*, 2015, **8**, 742–751.
- 90 J. Drelich, Guidelines to measurements of reproducible contact angles using a sessile-drop technique, *Surf. Innovations*, 2013, **1**, 248–254.
- 91 M. Santini, M. Guilizzoni and S. Fest-Santini, X-ray computed microtomography for drop shape analysis and contact angle measurement, *J. Colloid Interface Sci.*, 2013, **409**, 204–210.
- 92 J. Park, *et al.*, Direct and accurate measurement of size dependent wetting behaviors for sessile water droplets, *Sci. Rep.*, 2015, **5**, 18150.
- 93 E. Pierce, F. J. Carmona and A. Amirfazli, Understanding of sliding and contact angle results in tilted plate experiments, *Colloids Surf., A*, 2008, **323**, 73–82.
- 94 G. T. Smedley and D. E. Coles, A refractive tilting-plate technique for measurement of dynamic contact angles, *J. Colloid Interface Sci.*, 2005, **286**, 310–318.
- 95 C. G. L. Furnidge, Studies at phase interfaces. I. The sliding of liquid drops on solid surfaces and a theory for spray retention, *J. Colloid Sci.*, 1962, **17**, 309–324.
- 96 T. D. Blake, The physics of moving wetting lines, *J. Colloid Interface Sci.*, 2006, **299**, 1–13.
- 97 C. D. Volpe and S. Siboni, The Wilhelmy method: a critical and practical review, *Surf. Innovations*, 2018, **6**, 120–132.
- 98 A. M. Karim and H. P. Kavehpour, Effect of viscous force on dynamic contact angle measurement using Wilhelmy plate method, *Colloids Surf., A*, 2018, **548**, 54–60.
- 99 A. Bateni, S. S. Susnar, A. Amirfazli and A. W. Neumann, A high-accuracy polynomial fitting approach to determine contact angles, *Colloids Surf., A*, 2003, **219**, 215–231.
- 100 H. Wang, S. V. Garimella and J. Y. Murthy, Characteristics of an evaporating thin film in a microchannel, *Int. J. Heat Mass Transfer*, 2007, **50**, 3933–3942.
- 101 V. D. Sobolev, V. M. Starov and M. G. Velarde, *On the Accuracy of Measuring Small Contact Angles by the Sessile Drop Method*, 2003, vol. 65.
- 102 C. Dorrer and J. Rühle, Some thoughts on superhydrophobic wetting, *Soft Matter*, 2009, **5**, 51–61.
- 103 D. Daniel, *et al.*, Mapping micrometer-scale wetting properties of superhydrophobic surfaces, *Proc. Natl. Acad. Sci. U. S. A.*, 2019, **116**, 25008–25012.
- 104 R. Wang, L. Cong and M. Kido, Evaluation of the wettability of metal surfaces by micro-pure water by means of atomic force microscopy, *Appl. Surf. Sci.*, 2002, **191**, 74–84.
- 105 A. Checco, H. Schollmeyer, J. Daillant, P. Guenoun and R. Boukherroub, Nanoscale Wettability of Self-Assembled Monolayers Investigated by Noncontact Atomic Force Microscopy, *Langmuir*, 2006, **22**, 116–126.
- 106 A. V. Nguyen, J. Nalaskowski and J. D. Miller, The dynamic nature of contact angles as measured by atomic force microscopy, *J. Colloid Interface Sci.*, 2003, **262**, 303–306.
- 107 J. Yu, H. Wang and X. Liu, Direct measurement of macro contact angles through atomic force microscopy, *Int. J. Heat Mass Transfer*, 2013, **57**, 299–303.
- 108 Y. Deng, L. Xu, H. Lu, H. Wang and Y. Shi, Direct measurement of the contact angle of water droplet on quartz in a reservoir rock with atomic force microscopy, *Chem. Eng. Sci.*, 2018, **177**, 445–454.
- 109 X. Huo, *et al.*, Mechanism and Quantitative Characterization of Wettability on Shale Surfaces: An Experimental Study Based on Atomic Force Microscopy (AFM), *Energies*, 2023, **16**, 7527.
- 110 J. Castillo and G. L. Galarza-Acosta, Superhydrophobic silica nanoparticles produced from rice husks, wettability at the macro- and nanoscale, *Appl. Phys. A*, 2024, **130**, 102.
- 111 M. Wanli, K. Kobayashi and S. Murata, Wettability modification of muscovite surfaces using silica nanoparticles synthesized from rice husk, *Surf. Interfaces*, 2025, **70**, 106823.
- 112 C. Luo, H. Zheng, L. Wang, H. Fang, J. Hu, C. Fan, Y. Chao and J. Wang, Direct three-dimensional imaging of the buried interfaces between water and superhydrophobic surfaces, *Angew. Chem.*, 2010, **122**(48), 9331–9334.
- 113 A. Hongru, L. Xiangqin, S. Shuyan, Z. Ying and L. Tianqing, Measurement of Wenzel roughness factor by laser scanning confocal microscopy, *RSC Adv.*, 2017, **7**, 7052–7059.
- 114 B. Haimov, S. Pechook, O. Ternyak and B. Pokroy, Shape of Water-Air Interface beneath a Drop on a Superhydrophobic Surface Revealed: Constant Curvature That Approaches Zero, *J. Phys. Chem. C*, 2013, **117**, 6658–6663.



- 115 P. Papadopoulos, L. Mammen, X. Deng, D. Vollmer and H.-J. Butt, How superhydrophobicity breaks down, *Proc. Natl. Acad. Sci. U. S. A.*, 2013, **110**, 3254–3258.
- 116 E. Bormashenko, *et al.*, Environmental Scanning Electron Microscopy Study of the Fine Structure of the Triple Line and Cassie–Wenzel Wetting Transition for Sessile Drops Deposited on Rough Polymer Substrates, *Langmuir*, 2007, **23**, 4378–4382.
- 117 Y. C. Jung and B. Bhushan, Wetting behaviour during evaporation and condensation of water microdroplets on superhydrophobic patterned surfaces, *J. Microsc.*, 2008, **229**, 127–140.
- 118 A. T. Paxson and K. K. Varanasi, Self-similarity of contact line depinning from textured surfaces, *Nat. Commun.*, 2013, **4**, 1492.
- 119 L. M. Jenkins and A. M. Donald, Contact Angle Measurements on Fibers in the Environmental Scanning Electron Microscope, *Langmuir*, 1999, **15**, 7829–7835.
- 120 D. Aronov, G. Rosenman and Z. Barkay, Wettability study of modified silicon dioxide surface using environmental scanning electron microscopy, *J. Appl. Phys.*, 2007, **101**, 084901.
- 121 S. L. Schellbach, S. N. Monteiro and J. W. Drelich, A novel method for contact angle measurements on natural fibers, *Mater. Lett.*, 2016, **164**, 599–604.
- 122 M. Brugnara, C. D. Volpe, S. Siboni and D. Zeni, Contact angle analysis on polymethylmethacrylate and commercial wax by using an environmental scanning electron microscope, *Scanning*, 2006, **28**, 267–273.
- 123 K. Marbou, A. A. Ghaferi and M. Jouiad, *In situ* characterization of wettability alteration in HOPG, *SOP Trans. Nanotechnol.*, 2015, **2374**, 1–10.
- 124 Z. Barkay, Wettability study using transmitted electrons in environmental scanning electron microscope, *Appl. Phys. Lett.*, 2010, **96**, 183109.
- 125 P. Körber, Investigation on Building Materials with the SEM in the ESEM Mode to Demonstrate Their Capillarity Using the Contact Angle Method, in *Electron Microscopy*, ed. M. Mhadhbi, IntechOpen, 2022, DOI: [10.5772/intechopen.104292](https://doi.org/10.5772/intechopen.104292).
- 126 K. Al-Naimi, *et al.*, Micro-scale wettability of carbonate rocks via high-resolution ESEM imaging, *Results Phys.*, 2023, **52**, 106871.
- 127 C. S. Fadley, X-ray photoelectron spectroscopy: Progress and perspectives, *J. Electron Spectrosc. Relat. Phenom.*, 2010, **178–179**, 2–32.
- 128 A. A. Behroozmand, K. Keating and E. Auken, A Review of the Principles and Applications of the NMR Technique for Near-Surface Characterization, *Surv. Geophys.*, 2015, **36**, 27–85.
- 129 C. Berthomieu and R. Hienerwadel, Fourier transform infrared (FTIR) spectroscopy, *Photosynth. Res.*, 2009, **101**, 157–170.
- 130 S. P. Mulvaney and C. D. Keating, Raman Spectroscopy, *Anal. Chem.*, 2000, **72**, 145–158.
- 131 F. A. Stevie and C. L. Donley, Introduction to X-ray photoelectron spectroscopy, *J. Vac. Sci. Technol., A*, 2020, **38**, 063204.
- 132 H. S. N. Jayawardena, S. H. Liyanage, K. Rathnayake, U. Patel and M. Yan, Analytical Methods for Characterization of Nanomaterial Surfaces, *Anal. Chem.*, 2021, **93**, 1889–1911.
- 133 G. Zhou, C. Xu, W. Cheng, Q. Zhang and W. Nie, Effects of Oxygen Element and Oxygen-Containing Functional Groups on Surface Wettability of Coal Dust with Various Metamorphic Degrees Based on XPS Experiment, *J. Anal. Methods Chem.*, 2015, **2015**, 1–8.
- 134 C. Xu, G. Zhou and H. Qiu, Analysis of the microscopic mechanism of coal wettability evolution in different metamorphic states based on NMR and XPS experiments, *RSC Adv.*, 2017, **7**, 47954–47965.
- 135 S. K. Woche, *et al.*, Soil wettability can be explained by the chemical composition of particle interfaces - An XPS study, *Sci. Rep.*, 2017, **7**, 42877.
- 136 G. J. Pronk, *et al.*, Interaction of minerals, organic matter, and microorganisms during biogeochemical interface formation as shown by a series of artificial soil experiments, *Biol. Fertil. Soils*, 2017, **53**, 9–22.
- 137 B. Schampera, *et al.*, Surface structure of organoclays as examined by X-ray photoelectron spectroscopy and molecular dynamics simulations, *Clay Miner.*, 2015, **50**, 353–367.
- 138 B. Jiang, *et al.*, Investigation on the effect of functional groups on the wettability of coal dust: Experiments and theoretical validation, *Fuel*, 2023, **351**, 128987.
- 139 J. Yang, J. Chen and J. Song, Studies of the surface wettability and hydrothermal stability of methyl-modified silica films by FT-IR and Raman spectra, *Vib. Spectrosc.*, 2009, **50**, 178–184.
- 140 K. Vijayarangamuthu, *et al.* Temporospatial Control of Graphene Wettability, *Adv. Mater.*, 2016, **28**, 661–667.
- 141 P. K. Chow, *et al.* Wetting of Mono and Few-Layered WS<sub>2</sub> and MoS<sub>2</sub> Films Supported on Si/SiO<sub>2</sub> Substrates, *ACS Nano*, 2015, **9**, 3023–3031.
- 142 A. Kozbial, F. Zhou, Z. Li, H. Liu and L. Li, Are Graphitic Surfaces Hydrophobic?, *Acc. Chem. Res.*, 2016, **49**, 2765–2773.
- 143 A. Pertsin and M. Grunze, Water–Graphite Interaction and Behavior of Water Near the Graphite Surface, *J. Phys. Chem. B*, 2004, **108**, 1357–1364.
- 144 M. Rubeš, P. Nachtigall, J. Vondrášek and O. Bludský, Structure and Stability of the Water–Graphite Complexes, *J. Phys. Chem. C*, 2009, **113**, 8412–8419.
- 145 Y. Qiu, L. Lupi and V. Molinero, Is Water at the Graphite Interface Vapor-like or Ice-like?, *J. Phys. Chem. B*, 2018, **122**, 3626–3634.
- 146 G. Hong, *et al.*, On the Mechanism of Hydrophilicity of Graphene, *Nano Lett.*, 2016, **16**, 4447–4453.
- 147 A. Ashraf, *et al.*, Correction to Doping-Induced Tunable Wettability and Adhesion of Graphene, *Nano Lett.*, 2016, **16**(7), 4708–4712.



- 148 A. P. Terzyk, *et al.*, Water Nanodroplet on a Hydrocarbon “Carpet”—The Mechanism of Water Contact Angle Stabilization by Airborne Contaminations on Graphene, Au, and PTFE Surfaces, *Langmuir*, 2019, **35**, 420–427.
- 149 T. Smith, The hydrophilic nature of a clean gold surface, *J. Colloid Interface Sci.*, 1980, **75**, 51–55.
- 150 M. J. P. Nijmeijer, C. Bruin, A. F. Bakker and J. M. J. van Leeuwen, Wetting and drying of an inert wall by a fluid in a molecular-dynamics simulation, *Phys. Rev. A*, 1990, **42**, 6052–6059.
- 151 M. J. de Ruijter, T. D. Blake and J. De Coninck, Dynamic Wetting Studied by Molecular Modeling Simulations of Droplet Spreading, *Langmuir*, 1999, **15**, 7836–7847.
- 152 T. Koishi, K. Yasuoka, S. Fujikawa, T. Ebisuzaki and X. C. Zeng, Coexistence and transition between Cassie and Wenzel state on pillared hydrophobic surface, *Proc. Natl. Acad. Sci. U. S. A.*, 2009, **106**, 8435–8440.
- 153 D. Surblys, Y. Yamaguchi, K. Kuroda, T. Nakajima and H. Fujimura, Analysis on wetting and local dynamic properties of single water droplet on a polarized solid surface: A molecular dynamics study, *J. Chem. Phys.*, 2011, **135**, 014703.
- 154 N. Tretyakov, M. Müller, D. Todorova and U. Thiele, Parameter passing between molecular dynamics and continuum models for droplets on solid substrates: The static case, *J. Chem. Phys.*, 2013, **138**, 064905.
- 155 S. Chen, J. Wang, T. Ma and D. Chen, Molecular dynamics simulations of wetting behavior of water droplets on polytetrafluorethylene surfaces, *J. Chem. Phys.*, 2014, **140**, 114704.
- 156 J. Q. Broughton and G. H. Gilmer, Molecular dynamics investigation of the crystal–fluid interface. VI. Excess surface free energies of crystal–liquid systems, *J. Chem. Phys.*, 1986, **84**, 5759–5768.
- 157 R. L. Davidchack and B. B. Laird, Direct calculation of the crystal–melt interfacial free energies for continuous potentials: Application to the Lennard-Jones system, *J. Chem. Phys.*, 2003, **118**, 7651–7657.
- 158 F. Leroy, D. J. V. A. dos Santos and F. Müller-Plathe, Interfacial Excess Free Energies of Solid–Liquid Interfaces by Molecular Dynamics Simulation and Thermodynamic Integration, *Macromol. Rapid Commun.*, 2009, **30**, 864–870.
- 159 F. Leroy and F. Müller-Plathe, Solid-liquid surface free energy of Lennard-Jones liquid on smooth and rough surfaces computed by molecular dynamics using the phantom-wall method, *J. Chem. Phys.*, 2010, **133**, 044110.
- 160 F. Leroy and F. Müller-Plathe, Dry-Surface Simulation Method for the Determination of the Work of Adhesion of Solid–Liquid Interfaces, *Langmuir*, 2015, **31**, 8335–8345.
- 161 H. Jiang and A. J. Patel, Recent advances in estimating contact angles using molecular simulations and enhanced sampling methods, *Curr. Opin. Chem. Eng.*, 2019, **23**, 130–137.
- 162 B. H. Tan, H. An and C.-D. Ohl, Body Forces Drive the Apparent Line Tension of Sessile Droplets, *Phys. Rev. Lett.*, 2023, **130**, 064003.
- 163 D. Surblys, F. Müller-Plathe and T. Ohara, Computing the Work of Solid–Liquid Adhesion in Systems with Damped Coulomb Interactions via Molecular Dynamics: Approaches and Insights, *J. Phys. Chem. A*, 2022, **126**, 5506–5516.
- 164 S. Burian, *et al.*, Size-Dependent Wetting Contact Angles at the Nanoscale Defined by Equimolar Surfaces and Surfaces of Tension, *Sci. Rep.*, 2024, **14**, 31340.
- 165 G. Jiménez-Serratos, P. B. Warren, S. Singleton, D. J. Bray and R. L. Anderson, Modeling Contact Angles with Chemically Specific Dissipative Particle Dynamics, *Langmuir*, 2025, **41**, 3877–3887.
- 166 N. Sedighi, S. Murad and S. K. Aggarwal, Molecular dynamics simulations of nanodroplet spreading on solid surfaces, effect of droplet size, *Fluid Dyn. Res.*, 2010, **42**, 035501.
- 167 C. Yang, U. Tartaglino and B. N. J. Persson, Nanodroplets on rough hydrophilic and hydrophobic surfaces, *Eur. Phys. J. E*, 2008, **25**, 139–152.
- 168 S. Becker, H. M. Urbassek, M. Horsch and H. Hasse, Contact Angle of Sessile Drops in Lennard-Jones Systems, *Langmuir*, 2014, **30**, 13606–13614.
- 169 J. Di, Z. Yang and Y. Duan, Molecular dynamics simulation of nanosized water droplet spreading on chemically heterogeneous surfaces, *AIP Adv.*, 2019, **9**, 125105.
- 170 J. Liu, C. Wang, P. Guo, G. Shi and H. Fang, Linear relationship between water wetting behavior and microscopic interactions of super-hydrophilic surfaces, *J. Chem. Phys.*, 2013, **139**, 234703.
- 171 P. Johansson, A. Carlson and B. Hess, Water–substrate physico-chemistry in wetting dynamics, *J. Fluid Mech.*, 2015, **781**, 695–711.
- 172 G. Scocchi, D. Sergi, C. D’Angelo and A. Ortona, Wetting and contact-line effects for spherical and cylindrical droplets on graphene layers: A comparative molecular-dynamics investigation, *Phys. Rev. E: Stat., Nonlinear, Soft Matter Phys.*, 2011, **84**, 061602.
- 173 M. Kanduč, Going beyond the standard line tension: Size-dependent contact angles of water nanodroplets, *J. Chem. Phys.*, 2017, **147**, 174701.
- 174 J. H. Weijs, A. Marchand, B. Andreotti, D. Lohse and J. H. Snoeijer, Origin of line tension for a Lennard-Jones nanodroplet, *Phys. Fluids*, 2011, **23**, 022001.
- 175 M. Kanduč, L. Eixeres, S. Liese and R. R. Netz, Generalized line tension of water nanodroplets, *Phys. Rev. E*, 2018, **98**, 032804.
- 176 B. V. Toshev, D. Platikanov and A. Scheludko, Line tension in three-phase equilibrium systems, *Langmuir*, 1988, **4**, 489–499.
- 177 V. Raspal, *et al.*, Nanoporous Surface Wetting Behavior: The Line Tension Influence, *Langmuir*, 2012, **28**, 11064–11071.
- 178 M. Iwamatsu, Size-dependent contact angle and the wetting and drying transition of a droplet adsorbed onto a spherical substrate: Line-tension effect, *Phys. Rev. E*, 2016, **94**, 042803.



- 179 J.-C. Fernandez-Toledano, T. D. Blake, P. Lambert and J. De Coninck, On, the cohesion of fluids and their adhesion to solids: Young's equation at the atomic scale, *Adv. Colloid Interface Sci.*, 2017, **245**, 102–107.
- 180 Y. Escalona, N. Espinoza, M. Barria-Urenda, C. Oostenbrink and J. A. Garate, On the effects of induced polarizability at the water–graphene interface via classical charge-on-spring models, *Phys. Chem. Chem. Phys.*, 2022, **24**, 7748–7758.
- 181 A. Govind Rajan, V. Sresht and A. A. Pádua, Dominance of Dispersion Interactions and Entropy over Electrostatics in Determining the Wettability and Friction of Two-Dimensional MoS2 Surfaces, *ACS Nano*, 2016, **10**, 9145–9155.
- 182 D. Surblys, F. Leroy, Y. Yamaguchi and F. Müller-Plathe, Molecular dynamics analysis of the influence of Coulomb and van der Waals interactions on the work of adhesion at the solid-liquid interface, *J. Chem. Phys.*, 2018, **148**, 134707.
- 183 V. Kumar and J. Errington, Wetting Behavior of Water near Nonpolar Surfaces, *J. Phys. Chem. C*, 2013, **117**, 23017–23026.
- 184 F. Leroy, Revisiting the droplet simulation approach to derive force-field parameters for water on molybdenum disulfide from wetting angle measurements, *J. Chem. Phys.*, 2016, **145**, 164705.
- 185 H. J. C. Berendsen, J. R. Grigera and T. P. Straatsma, The missing term in effective pair potentials, *J. Phys. Chem.*, 1987, **91**, 6269–6271.
- 186 W. L. Jorgensen, J. Chandrasekhar, J. D. Madura, R. W. Impey and M. L. Klein, Comparison of simple potential functions for simulating liquid water, *J. Chem. Phys.*, 1983, **79**, 926–935.
- 187 F. M. Fowkes and W. D. Harkins, The State of Monolayers Adsorbed at the Interface Solid–Aqueous Solution, *J. Am. Chem. Soc.*, 1940, **62**, 3377–3386.
- 188 J. Li and F. Wang, Water graphene contact surface investigated by pairwise potentials from force-matching PAW-PBE with dispersion correction, *J. Chem. Phys.*, 2017, **146**, 054702.
- 189 T. Ondarçuhu, *et al.*, Wettability of partially suspended graphene, *Sci. Rep.*, 2016, **6**, 24237.
- 190 D. Li, *et al.*, Effects of low-temperature plasma treatment on wettability of glass surface: Molecular dynamic simulation and experimental study, *Appl. Surf. Sci.*, 2020, **503**, 144257.
- 191 F. S. Emami, *et al.*, Force Field and a Surface Model Database for Silica to Simulate Interfacial Properties in Atomic Resolution, *Chem. Mater.*, 2014, **26**, 2647–2658.
- 192 S. M. Foiles, M. I. Baskes and M. S. Daw, Embedded-atom-method functions for the fcc metals Cu, Ag, Au, Ni, Pd, Pt, and their alloys, *Phys. Rev. B: Condens. Matter Mater. Phys.*, 1986, **33**, 7983–7991.
- 193 S. K. Sethi, S. Kadian and G. Manik, A Review of Recent Progress in Molecular Dynamics and Coarse-Grain Simulations Assisted Understanding of Wettability, *Arch. Comput. Methods Eng.*, 2022, **29**, 3059–3085.
- 194 I. Morcos, Surface Tension of Stress-Annealed Pyrolytic Graphite, *J. Chem. Phys.*, 1972, **57**, 1801–1802.
- 195 B. Luan and R. Zhou, Wettability and friction of water on a MoS2 nanosheet, *Appl. Phys. Lett.*, 2016, **108**, 131601.
- 196 M. A. M. Munshi, *et al.*, A review of heat transport in solvated gold nanoparticles: Molecular dynamics modeling and experimental perspectives, *Nanoscale*, 2025, **17**, 20803–20830.
- 197 H. Heinz, T.-J. Lin, R. Kishore Mishra and F. S. Emami, Thermodynamically Consistent Force Fields for the Assembly of Inorganic, Organic, and Biological Nanostructures: The INTERFACE Force Field, *Langmuir*, 2013, **29**, 1754–1765.
- 198 A. Jaramillo-Botero, S. Naserifar and W. A. I. Goddard, General Multiobjective Force Field Optimization Framework, with Application to Reactive Force Fields for Silicon Carbide, *J. Chem. Theory Comput.*, 2014, **10**, 1426–1439.
- 199 L. Dumortier, C. Chizallet, B. Creton, T. de Bruin and T. Verstraelen, Managing Expectations and Imbalanced Training Data in Reactive Force Field Development: An Application to Water Adsorption on Alumina, *J. Chem. Theory Comput.*, 2024, **20**, 3779–3797.
- 200 P. S. Nerenberg and T. Head-Gordon, New developments in force fields for biomolecular simulations, *Curr. Opin. Struct. Biol.*, 2018, **49**, 129–138.
- 201 J. Behler, Four Generations of High-Dimensional Neural Network Potentials, *Chem. Rev.*, 2021, **121**, 10037–10072.
- 202 P. Hou, Y. Tian and X. Meng, Improving Molecular-Dynamics Simulations for Solid–Liquid Interfaces with Machine-Learning Interatomic Potentials, *Chem. – Eur. J.*, 2024, **30**, e202401373.
- 203 L. Zhang, J. Han, H. Wang, R. Car and E. Weinan, Deep Potential Molecular Dynamics: A Scalable Model with the Accuracy of Quantum Mechanics, *Phys. Rev. Lett.*, 2018, **120**, 143001.
- 204 B. Focassio, L. P. M. Freitas and G. R. Schleder, Performance Assessment of Universal Machine Learning Interatomic Potentials: Challenges and Directions for Materials' Surfaces, *ACS Appl. Mater. Interfaces*, 2025, **17**, 13111–13121.
- 205 T. W. Ko, J. A. Finkler, S. Goedecker and J. Behler, A fourth-generation high-dimensional neural network potential with accurate electrostatics including non-local charge transfer, *Nat. Commun.*, 2021, **12**, 398.
- 206 Y. K. Shin, C. M. Ashraf and A. C. T. van Duin, Development and Applications of the ReaxFF Reactive Force Field for Biological Systems, in *Computational Materials, Chemistry, and Biochemistry: From Bold Initiatives to the Last Mile*, ed. S. Shankar, R. Muller, T. Dunning and G. H. Chen, Springer International Publishing, Cham, 2021, pp. 157–182, DOI: [10.1007/978-3-030-18778-1\\_9](https://doi.org/10.1007/978-3-030-18778-1_9).



- 207 W. Zhang and A. C. T. van Duin, Second-Generation ReaxFF Water Force Field: Improvements in the Description of Water Density and OH-Anion Diffusion, *J. Phys. Chem. B*, 2017, **121**, 6021–6032.
- 208 H. Manzano, R. J. M. Pellenq, F.-J. Ulm, M. J. Buehler and A. C. T. van Duin, Hydration of Calcium Oxide Surface Predicted by Reactive Force Field Molecular Dynamics, *Langmuir*, 2012, **28**, 4187–4197.
- 209 J. C. Fogarty, H. M. Aktulga, A. Y. Grama, A. C. T. van Duin and S. A. Pandit, A reactive molecular dynamics simulation of the silica-water interface, *J. Chem. Phys.*, 2010, **132**, 174704.
- 210 B. Ramos-Alvarado, S. Kumar and G. P. Peterson, Wettability of graphitic-carbon and silicon surfaces: MD modeling and theoretical analysis, *J. Chem. Phys.*, 2015, **143**, 044703.
- 211 M. Samanian and M. H. Ghatee, Wettability Scope of MoS<sub>2</sub>–Ionic Liquid Interfaces and Their Modification toward Novel Superhydrophobic Boundaries, *Langmuir*, 2022, **38**, 4555–4566.
- 212 C. U. Gonzalez-Valle, S. Kumar and B. Ramos-Alvarado, Investigation on the Wetting Behavior of 3C-SiC Surfaces: Theory and Modeling, *J. Phys. Chem. C*, 2018, **122**, 7179–7186.
- 213 V. Kumar and J. R. Errington, Wetting Behavior of Water near Nonpolar Surfaces, *J. Phys. Chem. C*, 2013, **117**, 23017–23026.
- 214 S. Chattopadhyay, *et al.*, How Water Meets a Very Hydrophobic Surface, *Phys. Rev. Lett.*, 2010, **105**, 037803.
- 215 C. U. Gonzalez-Valle, S. Kumar and B. Ramos-Alvarado, Thermal Transport across SiC-Water Interfaces, *ACS Appl. Mater. Interfaces*, 2018, **10**, 29179–29186.
- 216 C. U. Gonzalez-Valle and B. Ramos-Alvarado, Spectral mapping of thermal transport across SiC-water interfaces, *Int. J. Heat Mass Transfer*, 2019, **131**, 645–653.
- 217 M. Mezger, *et al.*, On the Origin of the Hydrophobic Water Gap: An X-ray Reflectivity and MD Simulation Study, *J. Am. Chem. Soc.*, 2010, **132**, 6735–6741.
- 218 C. Weber and H. Stanjek, Energetic and entropic contributions to the work of adhesion in two-component, three-phase solid–liquid–vapour systems, *Colloids Surf., A*, 2014, **441**, 331–339.
- 219 K. Motomura, H. Iyota, M. Aratono, M. Yamanaka and R. Matuura, Thermodynamic consideration of the pressure dependence of interfacial tension, *J. Colloid Interface Sci.*, 1983, **93**, 264–269.
- 220 S. Zeppieri, J. Rodríguez and A. L. López De Ramos, Interfacial Tension of Alkane + Water Systems, *J. Chem. Eng. Data*, 2001, **46**, 1086–1088.
- 221 M. Orselly, *et al.*, Molecular interactions at the metal–liquid interfaces, *J. Chem. Phys.*, 2022, **156**, 234705.
- 222 W. Kohn, A. D. Becke and R. G. Parr, Density functional theory of electronic structure, *J. Phys. Chem.*, 1996, **100**, 12974–12980.
- 223 R. Jinnouchi and A. B. Anderson, Electronic structure calculations of liquid-solid interfaces: Combination of density functional theory and modified Poisson-Boltzmann theory, *Phys. Rev. B: Condens. Matter Mater. Phys.*, 2008, **77**, 245417.
- 224 W. A. Curtin, Density-functional theory of the solid-liquid interface, *Phys. Rev. Lett.*, 1987, **59**, 1228–1231.
- 225 K. Burke, Perspective on density functional theory, *J. Chem. Phys.*, 2012, **136**, 150901.
- 226 J. P. Perdew, K. Burke and M. Ernzerhof, Generalized Gradient Approximation Made Simple, *Phys. Rev. Lett.*, 1996, **77**, 3865–3868.
- 227 A. D. Becke, Density-functional exchange-energy approximation with correct asymptotic behavior, *Phys. Rev. A*, 1988, **38**, 3098–3100.
- 228 C. Lee, W. Yang and R. G. Parr, Development of the Colle-Salvetti correlation-energy formula into a functional of the electron density, *Phys. Rev. B: Condens. Matter Mater. Phys.*, 1988, **37**, 785–789.
- 229 B. Hammer, L. B. Hansen and J. K. Nørskov, Improved adsorption energetics within density-functional theory using revised Perdew-Burke-Ernzerhof functionals, *Phys. Rev. B: Condens. Matter Mater. Phys.*, 1999, **59**, 7413–7421.
- 230 J. Hafner, *Ab initio* simulations of materials using VASP: Density-functional theory and beyond, *J. Comput. Chem.*, 2008, **29**, 2044–2078.
- 231 F. Flores, J. Ortega and H. Vázquez, Modelling energy level alignment at organic interfaces and density functional theory, *Phys. Chem. Chem. Phys.*, 2009, **11**, 8658–8675.
- 232 M. V. Fernández-Serra and E. Artacho, Network equilibration and first-principles liquid water, *J. Chem. Phys.*, 2004, **121**, 11136–11144.
- 233 M. J. Gillan, D. Alfè and A. Michaelides, Perspective: How good is DFT for water?, *J. Chem. Phys.*, 2016, **144**, 130901.
- 234 J. Klimeš and A. Michaelides, Perspective: Advances and challenges in treating van der Waals dispersion forces in density functional theory, *J. Chem. Phys.*, 2012, **137**, 120901.
- 235 P. J. Hasnip, *et al.*, Density functional theory in the solid state, *Philos. Trans. R. Soc., A*, 2014, **372**, 20130270.
- 236 S. Grimme, J. Antony, S. Ehrlich and H. Krieg, A consistent and accurate *ab initio* parametrization of density functional dispersion correction (DFT-D) for the 94 elements H–Pu, *J. Chem. Phys.*, 2010, **132**, 154104.
- 237 S. Grimme, A. Hansen, J. G. Brandenburg and C. Bannwarth, Dispersion-Corrected Mean-Field Electronic Structure Methods, *Chem. Rev.*, 2016, **116**, 5105–5154.
- 238 A. Tkatchenko, Current Understanding of van der Waals Effects in Realistic Materials, *Adv. Funct. Mater.*, 2015, **25**, 2054–2061.
- 239 T. Bučko, S. Lebègue, T. Gould and J. G. Ángyán, Many-body dispersion corrections for periodic systems: an efficient reciprocal space implementation, *J. Phys.: Condens. Matter*, 2016, **28**, 045201.
- 240 A. J. Misquitta, J. Spencer, A. J. Stone and A. Alavi, Dispersion interactions between semiconducting wires,



- Phys. Rev. B: Condens. Matter Mater. Phys.*, 2010, **82**, 075312.
- 241 A. Groß and S. Sakong, Ab Initio Simulations of Water/Metal Interfaces, *Chem. Rev.*, 2022, **122**, 10746–10776.
- 242 J. Sun, A. Ruzsinszky and J. P. Perdew, Strongly Constrained and Appropriately Normed Semilocal Density Functional, *Phys. Rev. Lett.*, 2015, **115**, 036402.
- 243 M. Chen, *et al.*, Ab initio theory and modeling of water, *Proc. Natl. Acad. Sci. U. S. A.*, 2017, **114**, 10846–10851.
- 244 C. Li, X. Zheng, A. J. Cohen, P. Mori-Sánchez and W. Yang, Local Scaling Correction for Reducing Delocalization Error in Density Functional Approximations, *Phys. Rev. Lett.*, 2015, **114**, 053001.
- 245 S. Dasgupta, E. Lambros, J. P. Perdew and F. Paesani, Elevating density functional theory to chemical accuracy for water simulations through a density-corrected many-body formalism, *Nat. Commun.*, 2021, **12**, 6359.
- 246 E. B. Isaacs and C. Wolverton, Performance of the strongly constrained and appropriately normed density functional for solid-state materials, *Phys. Rev. Mater.*, 2018, **2**, 063801.
- 247 Y. Fu and D. J. Singh, Applicability of the Strongly Constrained and Appropriately Normed Density Functional to Transition-Metal Magnetism, *Phys. Rev. Lett.*, 2018, **121**, 207201.
- 248 M. Ekholm, *et al.*, Assessing the SCAN functional for itinerant electron ferromagnets, *Phys. Rev. B*, 2018, **98**, 094413.
- 249 P. Kovács, F. Tran, P. Blaha and G. K. H. Madsen, Comparative study of the PBE and SCAN functionals: The particular case of alkali metals, *J. Chem. Phys.*, 2019, **150**, 164119.
- 250 R. Rousseau, V.-A. Glezakou and A. Selloni, Theoretical insights into the surface physics and chemistry of redox-active oxides, *Nat. Rev. Mater.*, 2020, **5**, 460–475.
- 251 T. T. Trinh, X. Rozanska, F. Delbecq and P. Sautet, The initial step of silicate versus aluminosilicate formation in zeolite synthesis: a reaction mechanism in water with a tetrapropylammonium template, *Phys. Chem. Chem. Phys.*, 2012, **14**, 3369–3380.
- 252 R. E. Buló, C. Michel, P. Fleurat-Lessard and P. Sautet, Multiscale Modeling of Chemistry in Water: Are We There Yet?, *J. Chem. Theory Comput.*, 2013, **9**, 5567–5577.
- 253 A. Groß, *et al.*, Water Structures at Metal Electrodes Studied by Ab Initio Molecular Dynamics Simulations, *J. Electrochem. Soc.*, 2014, **161**, E3015–E3020.
- 254 J. Le, Q. Fan, L. Perez-Martinez, A. Cuesta and J. Cheng, Theoretical insight into the vibrational spectra of metal-water interfaces from density functional theory based molecular dynamics, *Phys. Chem. Chem. Phys.*, 2018, **20**, 11554–11558.
- 255 S. Sakong and A. Groß, Water structures on a Pt(111) electrode from ab initio molecular dynamic simulations for a variety of electrochemical conditions, *Phys. Chem. Chem. Phys.*, 2020, **22**, 10431–10437.
- 256 P. Clabaut, R. Staub, J. Galiana, E. Antonetti and S. N. Steinmann, Water adlayers on noble metal surfaces: Insights from energy decomposition analysis, *J. Chem. Phys.*, 2020, **153**, 054703.
- 257 S. K. Iyemperumal and N. A. Deskins, Evaluating Solvent Effects at the Aqueous/Pt(111) Interface, *ChemPhysChem*, 2017, **18**, 2171–2190.
- 258 R. Car and M. Parrinello, Unified Approach for Molecular Dynamics and Density-Functional Theory, *Phys. Rev. Lett.*, 1985, **55**, 2471–2474.
- 259 S. Izvekov, A. Mazzolo, K. VanOpdorp and G. A. Voth, Ab initio molecular dynamics simulation of the Cu(110)-water interface, *J. Chem. Phys.*, 2001, **114**, 3248–3257.
- 260 S. Meng, E. G. Wang and S. Gao, Water adsorption on metal surfaces: A general picture from density functional theory studies, *Phys. Rev. B: Condens. Matter Mater. Phys.*, 2004, **69**, 195404.
- 261 J. Hafner, Ab-initio simulations of materials using VASP: Density-functional theory and beyond, *J. Comput. Chem.*, 2008, **29**, 2044–2078.
- 262 I.-F. W. Kuo, C. J. Mundy, M. J. McGrath and J. I. Siepmann, Time-Dependent Properties of Liquid Water: A Comparison of Car-Parrinello and Born-Oppenheimer Molecular Dynamics Simulations, *J. Chem. Theory Comput.*, 2006, **2**, 1274–1281.
- 263 G. Kresse, Ab initio molecular dynamics for liquid metals, *J. Non-Cryst. Solids*, 1995, **192–193**, 222–229.
- 264 G. Kresse and J. Furthmüller, Efficient iterative schemes for ab initio total-energy calculations using a plane-wave basis set, *Phys. Rev. B: Condens. Matter Mater. Phys.*, 1996, **54**, 11169–11186.
- 265 T. D. Kühne, *et al.*, CP2K: An electronic structure and molecular dynamics software package - Quickstep: Efficient and accurate electronic structure calculations, *J. Chem. Phys.*, 2020, **152**, 194103.
- 266 P. Giannozzi, *et al.*, Advanced capabilities for materials modelling with Quantum ESPRESSO, *J. Phys.: Condens. Matter*, 2017, **29**, 465901.
- 267 S. Meng, L. F. Xu, E. G. Wang and S. Gao, Vibrational Recognition of Hydrogen-Bonded Water Networks on a Metal Surface, *Phys. Rev. Lett.*, 2002, **89**, 176104.
- 268 S. Meng, E. G. Wang and S. Gao, Water adsorption on metal surfaces: A general picture from density functional theory studies, *Phys. Rev. B: Condens. Matter Mater. Phys.*, 2004, **69**, 195404.
- 269 H. Ibach, Vibration spectroscopy of water on stepped gold surfaces, *Surf. Sci.*, 2010, **604**, 377–385.
- 270 X. Lin and A. Groß, First-principles study of the water structure on flat and stepped gold surfaces, *Surf. Sci.*, 2012, **606**, 886–891.
- 271 H. Noguchi, T. Okada and K. Uosaki, Molecular structure at electrode/electrolyte solution interfaces related to electrocatalysis, *Faraday Discuss.*, 2008, **140**, 125–137.
- 272 W. Schmickler and E. Santos, Metal and semiconductor electrodes, in *Interfacial Electrochemistry*, ed. W. Schmickler and E. Santos, Springer, Berlin, Heidelberg, 2010, pp. 9–18, DOI: [10.1007/978-3-642-04937-8\\_2](https://doi.org/10.1007/978-3-642-04937-8_2).



- 273 C.-Y. Li, *et al.*, In situ probing electrified interfacial water structures at atomically flat surfaces, *Nat. Mater.*, 2019, **18**, 697–701.
- 274 S. Schnur and A. Groß, Properties of metal–water interfaces studied from first principles, *New J. Phys.*, 2009, **11**, 125003.
- 275 J. Hughes, E. J. Krebs and D. Roundy, A classical density-functional theory for describing water interfaces, *J. Chem. Phys.*, 2013, **138**, 024509.
- 276 C. Zhang, *et al.*, Modeling Liquid Water by Climbing up Jacob's Ladder in Density Functional Theory Facilitated by Using Deep Neural Network Potentials, *J. Phys. Chem. B*, 2021, **125**, 11444–11456.
- 277 S. Ringe, N. G. Hörmann, H. Oberhofer and K. Reuter, Implicit Solvation Methods for Catalysis at Electrified Interfaces, *Chem. Rev.*, 2021, **122**(12), 10777–10820.
- 278 J.-L. Fattebert and F. Gygi, Density functional theory for efficient ab initio molecular dynamics simulations in solution, *J. Comput. Chem.*, 2002, **23**, 662–666.
- 279 S. A. Petrosyan, A. A. Rigos and T. A. Arias, Joint density-functional theory: ab initio study of Cr<sub>2</sub>O<sub>3</sub> surface chemistry in solution, *J. Phys. Chem. B*, 2005, **109**, 15436–15444.
- 280 O. Andreussi, I. Dabo and N. Marzari, Revised self-consistent continuum solvation in electronic-structure calculations, *J. Chem. Phys.*, 2012, **136**, 064102.
- 281 N. G. Hörmann, *et al.*, Absolute band alignment at semiconductor-water interfaces using explicit and implicit descriptions for liquid water, *npj Comput. Mater.*, 2019, **5**, 100.
- 282 K. Xu, *et al.*, Pulse Dynamics of Electric Double Layer Formation on All-Solid-State Graphene Field-Effect Transistors, *ACS Appl. Mater. Interfaces*, 2018, **10**, 43166–43176.
- 283 H. H. Heenen, J. A. Gauthier, H. H. Kristoffersen, T. Ludwig and K. Chan, Solvation at metal/water interfaces: An ab initio molecular dynamics benchmark of common computational approaches, *J. Chem. Phys.*, 2020, **152**, 144703.
- 284 A. Klamt, COSMO-RS for aqueous solvation and interfaces, *Fluid Phase Equilib.*, 2016, **407**, 152–158.
- 285 A. Kondor, G. Járvas, J. Kontos and A. Dallos, Temperature dependent surface tension estimation using COSMO-RS sigma moments, *Chem. Eng. Res. Des.*, 2014, **92**, 2867–2872.
- 286 V. Goussard, *et al.*, Predicting the Surface Tension of Liquids: Comparison of Four Modeling Approaches and Application to Cosmetic Oils, *J. Chem. Inf. Model.*, 2017, **57**, 2986–2995.
- 287 M. P. Andersson, N. M. Hassan and N. M. Alsaifi, Prediction of Surface Tension Using COSMO-RS, *Ind. Eng. Chem. Res.*, 2024, **63**, 22452–22460.
- 288 M. P. Andersson, *et al.*, First-Principles Prediction of Surface Wetting, *Langmuir*, 2020, **36**, 12451–12459.
- 289 M. M. Pereira, *et al.*, Contact angles and wettability of ionic liquids on polar and non-polar surfaces, *Phys. Chem. Chem. Phys.*, 2015, **17**, 31653–31661.
- 290 D. Sebastiani and L. Delle Site, Adsorption, of Water Molecules on Flat and Stepped Nickel Surfaces from First Principles, *J. Chem. Theory Comput.*, 2005, **1**, 78–82.
- 291 J. L. C. Fajín, M. N. D. S. Cordeiro and J. R. B. Gomes, Density Functional Theory Study of the Water Dissociation on Platinum Surfaces: General Trends, *J. Phys. Chem. A*, 2014, **118**, 5832–5840.
- 292 W. T. Cahyanto, *et al.*, A First-Principles Study of the Adsorption of H<sub>2</sub>O on Ru- and Mo-Alloyed Pt(111) Surfaces, *J. Electron. Mater.*, 2020, **49**, 2642–2650.
- 293 Y. Gohda, S. Schnur and A. Groß, Influence of water on elementary reaction steps in electrocatalysis, *Faraday Discuss.*, 2008, **140**, 233–244.
- 294 Z. Xu, J. Rossmeisler and J. R. Kitchin, A Linear Response DFT+U Study of Trends in the Oxygen Evolution Activity of Transition Metal Rutile Dioxides, *J. Phys. Chem. C*, 2015, **119**, 4827–4833.
- 295 G. Materzanini, G. F. Tantardini, P. J. D. Lindan and P. Saalfrank, Water adsorption at metal surfaces: A first-principles study of the  $p(\sqrt{3}\times\sqrt{3})R\ 30^\circ$  H<sub>2</sub>O bilayer on Ru (0001), *Phys. Rev. B: Condens. Matter Mater. Phys.*, 2005, **71**, 155414.
- 296 C. H. Kung, P. K. Sow, B. Zahiri and W. Mérida, Assessment and Interpretation of Surface Wettability Based on Sessile Droplet Contact Angle Measurement: Challenges and Opportunities, *Adv. Mater. Interfaces*, 2019, **6**, 1900839.
- 297 X. Huo, *et al.*, Mechanism and Quantitative Characterization of Wettability on Shale Surfaces: An Experimental Study Based on Atomic Force Microscopy (AFM), *Energies*, 2023, **16**, 7527.
- 298 H. Y. Erbil, The debate on the dependence of apparent contact angles on drop contact area or three-phase contact line: A review, *Surf. Sci. Rep.*, 2014, **69**, 325–365.
- 299 J. M. Schuster, C. E. Schvezov and M. R. Rosenberger, Influence of Experimental Variables on the Measure of Contact Angle in Metals Using the Sessile Drop Method, *Procedia Mater. Sci.*, 2015, **8**, 742–751.
- 300 J. Park, U. Pasaogullari and L. Bonville, Wettability measurements of irregular shapes with Wilhelmy plate method, *Appl. Surf. Sci.*, 2018, **427**, 273–280.
- 301 M. Brugnara, C. D. Volpe, S. Siboni and D. Zeni, Contact angle analysis on polymethylmethacrylate and commercial wax by using an environmental scanning electron microscope, *Scanning*, 2006, **28**, 267–273.
- 302 T. Smith, The hydrophilic nature of a clean gold surface, *J. Colloid Interface Sci.*, 1980, **75**, 51–55.
- 303 S. Gim, H.-K. Lim and H. Kim, Multiscale Simulation Method for Quantitative Prediction of Surface Wettability at the Atomistic Level, *J. Phys. Chem. Lett.*, 2018, **9**, 1750–1758.
- 304 V. L. Deringer, M. A. Caro and G. Csányi, Machine Learning Interatomic Potentials as Emerging Tools for Materials Science, *Adv. Mater.*, 2019, **31**, 1902765.
- 305 . Direct and accurate measurement of size dependent wetting behaviors for sessile water droplets | Scientific Reports, <https://www.nature.com/articles/srep18150>.



- 306 Z. Li, *et al.*, Effect of airborne contaminants on the wettability of supported graphene and graphite, *Nat. Mater.*, 2013, **12**, 925–931.
- 307 A. Poynor, *et al.*, How Water Meets a Hydrophobic Surface, *Phys. Rev. Lett.*, 2006, **97**, 266101.
- 308 C. Sendner, D. Horinek, L. Bocquet and R. R. Netz, Interfacial Water at Hydrophobic and Hydrophilic Surfaces: Slip, Viscosity, and Diffusion, *Langmuir*, 2009, **25**, 10768–10781.
- 309 A. Anandakrishnan, B. Ramos-Alvarado, S. K. Kannam and S. P. Sathian, Effects of interfacial molecular mobility on thermal boundary conductance at solid–liquid interface, *J. Chem. Phys.*, 2023, **158**, 094710.
- 310 P.-G. De Gennes, F. Brochard-Wyart and D. Quéré, *Capillarity and Wetting Phenomena*, Springer, New York, NY, 2004, DOI: [10.1007/978-0-387-21656-0](https://doi.org/10.1007/978-0-387-21656-0).
- 311 P. Fenter and S. S. Lee, Hydration layer structure at solid–water interfaces, *MRS Bull.*, 2014, **39**, 1056–1061.
- 312 J. Behler, First Principles Neural Network Potentials for Reactive Simulations of Large Molecular and Condensed Systems, *Angew. Chem., Int. Ed.*, 2017, **56**, 12828–12840.
- 313 V. L. Deringer, *et al.*, Gaussian Process Regression for Materials and Molecules, *Chem. Rev.*, 2021, **121**, 10073–10141.

